

ABSTRACT

Title of Document: ARTIFICIAL KAGOME SPIN ICE
Yi Qi, Doctor of Philosophy, 2008
Directed By: John Cumings, Assistant Professor, Department
of Materials Science and Engineering

Geometrical frustration is known to significantly modify the properties of many materials. Pyrochlore spin ice and hexagonal water ice are canonical systems that show the effects of frustration in both heat capacity and dynamical response. In both instances, microscopic ordering principles on the lattice lead to a macroscopic degeneracy of configurations. This degeneracy in spin ice may also be modified or lifted by lattice imperfections, external pressure, or magnetic field. Unfortunately, these effects are difficult to model or predict, because existing experimental techniques cannot directly observe the local ordering, near lattice defects or otherwise. To address this long outstanding problem, recent interest has focused on fabricating systems that allow the effects of frustration to be physically modeled and the resulting local configurations to be directly observed.

In this dissertation, I present an artificial approach to kagome lattice. The kagome lattice is a two-dimensional structure composed of corner-sharing triangles and is an essential component of the pyrochlore spin ice structure. Our artificial

kagome spin ice, constructed by magnetic nano-bar elements, mimics spin ice in 2D. The realized system rigorously obeys the ice rule (2-in 1-out or 1-in 2-out configuration at a vertex of three elements), thus providing a sought-after model system appropriate for further studies.

To study the ground state of the artificial kagome system and to validate the artificial approach for spin ice study, we demagnetize the samples using rotating field and observe spin configurations using Lorentz TEM. The ice rule, short-range ordering and absence of long-range disorder, as well as the relatively low remnant magnetization are found in the system, which are signatures of spin ice materials in their ground states. To model our system and relate it to other spin study, we introduce magnetic charge model and Shannon entropy concept. The calculated charge correlation (charge ordering coefficient) and Shannon entropy suggest that the degeneracy of our lattice is lifted from a completely disordered kagome spin ice system, and close to a “true” ground state that is usually found as the kagome plateau in pyrochlore spin ice when applying a field in $\langle 111 \rangle$ direction.

We also study the effects of external perturbations. When applying a magnetic field, chain-like spin flipping is found in the system, which can be explained by the magnetic charge model. When distorting the lattice by introducing an artificial strain, we observe partial ordering or symmetry breaking in the system, which is similar to the pressure effects in real spin ice.

In the Appendix, I also introduce another study I have done, i.e. multiferroic thin film measurements. The focus of that chapter is the dielectric measurement for BaTiO₃ (BTO) -CoFe₂O₄ (CFO) thin film material using a microwave microscope.

The measurement has a quantitative spatial resolution of approximately 5 μm , and it provides a method for film quality check and the basis for a proposed ME coupling measurement.

ARTIFICIAL KAGOME SPIN ICE

By

Yi Qi

Dissertation submitted to the Faculty of the Graduate School of the
University of Maryland, College Park, in partial fulfillment
of the requirements for the degree of
Doctor of Philosophy
2008

Advisory Committee:
Assistant Professor Jon cumings, Chair/Advisor
Professor Steve Anlage, Dean's Representative
Professor Robert Briber
Professor Lourdes Salamanca-Riba
Professor Manfred Wuttig

© Copyright by
Qi, Yi
2008

Preface

Three years ago, I once had a time hesitating whether if I should continue my graduate study and career as a researcher. Then I met Prof. John Cumings, who at that time just joined the Department of Materials Science and Engineering at Maryland and was building his new lab. I remember he told me, “Once you find a goal, just do it. Too much thinking does not help anything.” I felt lucky that I joined his group later and had the opportunity to work on this exciting project – Artificial spin ice. This dissertation represents the published and unpublished experiments completed for this project. It also contains the results on multiferroics I had done with Prof. Steve Anlage in Physics department.

Both Artificial spin ice and multiferroic materials are fabricated through nano-engineering, either by self-assembly or nano-patterning. The artificial spin ice can be seen as model system of geometrical frustrated materials spin ice or water ice by mimicking their local interactions, thus it can help us understand the physics of spin ice and water ice and study the frustration in general. It also has potential application as high density data storage and so on. Multiferroics (magneto-electric materials) have magnetic ordering and electric ordering simultaneously in the system, and it has application potential in novel device, such as sensor, tunable MRAM, based on their coupling effect.

The results in this dissertation represent collaboration efforts from Cumings group with other groups, departments and universities.

Dedication

To Mom and Dad, my wife Lily, and my daughter.

Acknowledgements

First I would like to thank my loved wife, Lily. When we married three years ago, she decided to quit her job as an editor in Beijing and accompany me here. Her great love has delighted my life and supported my graduate study. She is talented woman with her own dream, and I believe she can get there with her efforts and persistence.

I must acknowledge my advisor, Professor John Cumings, for making this dissertation possible. His broad knowledge in science, great passion for research, and creative ideas always impress me a lot. He has always been supportive to my research by encouraging every step forward I have made. He never hesitates to get down finding the problem when I had trouble in experiments. He is also a good friend, willing to provide any help in my life. I also want to thank Heather, John's wife, for all the advice she's given to my wife and me regarding our baby, and for the food she's provided at their sweet home.

I also want to thank my previous advisor, Professor Steve Analge, for supporting and guiding me when I first came to Maryland. He's always willing to help in my research and study. I am grateful that he spent a lot of time working with me in detail, teaching me to do research. I remember he gave me a lot of encouragement when I gave first several presentations, and helped to build my confidence to speak in public.

I would like to thank Professor Manfred Wuttig, for his generous advice. His knowledge in magnetic materials, insight in general science and his humor sense have inspired me. His door has been always open for me. I want to thank Professor

Lourdes Salamanca-Riba for teaching the TEM course, which I later found so helpful in my real research. I am also grateful to Professor Robert Briber for his encouragement and discussions on my project. He is willing to come to graduate students and find what we need. I thank all the members for taking time to read this dissertation for doing me the honor of serving on my committee.

I also want to thank other professors in the department who helped me in my research. Professor Alexander L. Roytburd has been a great teacher (especially in Thermodynamics course) and personal friend. I am grateful that he treats his students as talents. I also thank Professor Ichiro Takeuchi for his advice both in my research projects, and my career. They gave me a lot of help and I am very grateful.

I want to thank particularly our collaborators at Johns Hopkins University, Professor Oleg Tchernyshyov, and his student Paula Mellado. They have traveled several times here to discuss this project. Their understanding in magnetic and frustrated system, as well as their great enthusiasm in research gave me a lot of help and support. I also want to thank Professor M. S. Fuhrer, Professor T. Einstein and Bill Cullen in Physics department for giving advice on this study.

I am indebted to my fellow graduate students / post-doc in the Cumings group at Maryland. Todd Brintlinger has taught me every step of the SEM operation, the deposition and so on. He also spent a lot of time editing my thesis and papers. I thank him deeply. I also want to thank Kamal Baloch for taking time editing my thesis and helping in experiments. He is a very warm guy. I want to thank Colin Heikes for helping with part machining, Jeremy Cheng for helping with spin counting. I also want to thank Paris Alexander and Stephen Daunheimer for their

encouragement and discussion. All the group members are always willing to help and they make the group active, effective and attractive.

I thank all my friends at Maryland for their support. Jason Hattrick-Simpers, S.-H. Lim, Yijun Wang, Hua Xu, Shixong Zhang, Haimei Zheng, Chris Long, Shenqiang Ren, Atif Imtiaz, Mircea Dragos, Sameer Hemmady, A. V. Ustinov all have given a lot of help in my research and life.

I also want to thank Tim Zhang particularly for designing the power control and making TEM accessible. I thank Tom Loughran for teaching me to use the e-beam evaporator, and other staff in the Fab-lab for their help.

I need to acknowledge all the staff members in the department. I thank Kathleen Hart for her academic support, Olivia for ordering and receiving, Annette Mateus for conferences and general business help, Kay Morris for benefits support and many others.

Lastly, my family and friends in China were always there for me, and I want to acknowledge them here.

Table of Contents

Preface.....	ii
Dedication.....	iii
Acknowledgements.....	iv
Table of Contents.....	vii
List of Tables.....	viii
List of Figures.....	ix
Chapter 1 : Introduction.....	1
Chapter 2 : Frustration and Spin Ice.....	4
2.1 Frustration and geometrical frustration.....	4
2.2 Ice and ice rule.....	8
2.3 Spin ice.....	9
2.4 Meta materials.....	15
Chapter 3 : Artificial Kagome Spin Ice.....	19
3.1 Artificial spin ice.....	19
3.2 Kagome spin ice.....	24
3.3 sample fabrication.....	30
3.4 Spin direction detecting- Lorentz TEM.....	33
3.5 Demagnetization protocols.....	35
Chapter 4 : Ground State Study.....	37
4.1 Direct observation of ice rule.....	37
4.2 Fourier transform of Lorentz TEM images.....	40
4.3 Correlations.....	44
4.4 charge correlation.....	49
4.5 Ground state entropy.....	54
Chapter 5 : Magnetization Reversal and Symmetry-breaking.....	59
5.1 magnetization reversal.....	59
5.2 distortion tuned frustration.....	62
5.3 lithography stigmatism and crystal anisotropy.....	70
Chapter 6 Summary and future works.....	76
Appendix A: Lorentz TEM and Contrast Transfer Function.....	80
Appendix B: Lithography Procedure.....	86
Appendix C: Multi-ferroic materials.....	88
C.1 Multiferroic andMagnetoelectric materials.....	88
C.2 Microwave microscope.....	92
C.3 Dielectric properties of BTO-CFO thin film.....	96
C.4 Magneto-electro coupling imaging.....	100
Bibliography.....	109

List of Tables

Table I OOMMF simulated exchange energy and dipolar energy value for different moment configuration of square vertex.....	23
Table II OOMMF simulated exchange energy and dipolar energy value for different moment configuration of triangular vertex.	29
Table III Correlation coefficients of artificial kagome spin ice calculated from a demagnetized sample.	47

List of Figures

Figure 2.1	Illustration of geometrical frustration	4
Figure 2.2	Different types of 2D lattices with triangular symmetry	6
Figure 2.3	Different types of 3D lattices with triangular symmetry	7
Figure 2.4	(Left) Local proton arrangement in water ice and ice rule; (Right) The spin configuration in the spin ice structure.....	9
Figure 2.5	Specific heat measurement and entropy calculation for $\text{Dy}_2\text{Ti}_2\text{O}_7$ spin ice	12
Figure 2.6	(Left) Experimental neutron scattering pattern of $\text{Ho}_2\text{Ti}_2\text{O}_7$ in the (hkl) plane of reciprocal space at $T = 50$ mK. (Right) Magnetic field dependence of the scattering from $\text{Ho}_2\text{Ti}_2\text{O}_7$ at a sample temperature of 0.35 K	14
Figure 2.7	Examples of meta-materials with artificial structures	17
Figure 2.8	Ni-Fe magnetic film with perforated holes shows hard magnet properties.	17
Figure 3.1	Atomic Force Microscope (AFM) and Magnetic Force Microscope (MFM) images of frustrated square lattice.....	20
Figure 3.2	Illustration of frustration on the square lattice.....	20
Figure 3.3	OOMMF simulations of the square vertex with different moment configurations.....	22
Figure 3.4	Possible true minimum energy state of artificial square spin ice. The arrows of alternate squares have the same configuration.....	24
Figure 3.5	Layer structures of pyrochlore lattice	25
Figure 3.6	Sketch of kagome spin ice and its ice rule.....	26
Figure 3.7	OOMMF simulations of the kagome vertex with different moment configurations.....	28
Figure 3.8	Illustration of fabrication process	31
Figure 3.9	TEM images of our fabricated kagome lattice with connected islands (left) and isolated islands (right).	32
Figure 3.10	TEM picture of our fabricated lattice with a larger field of view	32
Figure 3.11	Contrast transfer function simulation and Fresnel image of magnetic bar elements.....	34
Figure 3.12	Lorentz TEM images of the kagome lattice with connected elements (Left) or isolated islands (right)	34
Figure 3.13	Illustration of the demagnetization setup.....	36
Figure 3.14	The field protocol used in demagnetization process.	36
Figure 4.1	Spin vertex distribution in demagnetized kagome lattice.....	39
Figure 4.2	Fourier transforms of Lorentz images of the artificial kagome spin ice (six-fold average).....	41
Figure 4.3	FFT simulations from a computer generated fake spin ice lattice. The insets of each picture denote one ordered (FM or AFM) sub-lattice corresponding to that FFT image.	43
Figure 4.4	Illustration of different types of spin pairs.....	45
Figure 4.5	Illustration of two dipole interaction in x-y coordinates.....	48

Figure 4.6	Kagome plateau in pyrochlore spin ice and its magnetic charge distribution	50
Figure 4.7	Mapping from dipoles to dumb bells	51
Figure 4.8	Magnetic charge maps	54
Figure 4.9	Shannon entropy for a binary system.	55
Figure 4.10	Shannon entropy based on different alphabets	57
Figure 5.1	Magnetization process when field is along a zigzag chain.....	60
Figure 5.2	Magnetization process when field is along a spin and has 60° angle with the other two spin sub-lattice	61
Figure 5.3	Sketch of the proposed kagome spin ice with strain-like distortion	64
Figure 5.4	Vertex type distribution with lattice distortion.....	64
Figure 5.5	OOMMF simulation of a three-spin vertex with various distortions	66
Figure 5.6	Energy change of triangular vertex with ‘strain’ distortion	67
Figure 5.7	Correlation symbols definition for three sub-lattices.....	68
Figure 5.8	Correlations vs. strain-like distortion measurements.....	69
Figure 5.9	Remnant magnetization of kagome lattice before and after demagnetization	72
Figure 5.10	Vertex distribution before and after demagnetization.....	73
Figure 5.11	A kagome spin ice sample with various widths.	74
Figure 5.12	Vertex distribution after demagnetization for sample in Fig 5.10.	75
Figure A.1	Lorentz TEM image of a permalloy thin film shows domain structures	80
Figure A.2	The deflection of electrons on passing through a uniform ferromagnetic foil that contains one domain wall.	81
Figure A.3	Schematic representation of the intensity distribution in a fresnel image of a ferromagnetic foil containing two 180 domain walls.	84
Figure A.4	Contrast transfer function simulation and Fresnel image of magnetic nano bar elements.	85
Figure C.1	The BTO-CFO thin film nano-composite structure characterization	90
Figure C.2	The BTO-CFO thin film nano-composite magnetic and electric properties	91
Figure C.3	Schematic illustration of a microwave microscope.	92
Figure C.4	Characterization curves of microwave microscope for dielectric measurements	95
Figure C.5	Illustration of thin film sample and the microwave probe.	96
Figure C.6	Dielectric scanning and resolution characterization	97
Figure C.7	Dielectric image of BTO-CFO thin film.	98
Figure C.8	Schematic diagram of Microwave Microscope for ME measurement.	101
Figure C.9	Illustration of microscope tip, sample geometry (left) and electric field with a bias voltage (right).	102

Figure C.10 Illustration of Thin film sample morphology (bottom) and
BTO/CFO lattice (top)..... 103
Figure C.11 Illustration of the dielectric constant change with ac electric
field and the generation of 2f signal for a BTO/SRO thin film. 106

Chapter 1 : Introduction

In materials science, the capability of nano-engineering allows us to fabricate new materials or structures that do not exist in nature. Those materials or structure either lift limits and expand freedoms of properties (e.g. Super-rigid materials or materials that combine magnetic and electric properties), or show completely different properties than conventional materials (e.g. Left hand materials). Moreover, model materials can be fabricated through nano-engineering that mimic certain behaviors/ interactions, thus help us understand the physics of existing materials. Regarding materials fabrication, it can be either a spontaneous process that organize molecular units into ordered structures by thermodynamics (self-assembly), or a manipulated process that manufacture and tailor the structure to desired geometry (nano-patterning).

In this dissertation, I introduce two types of materials in this scheme. One, also the majority of this thesis, is artificial spin ice, which is fabricated to mimic the frustrated behavior of spin ice and water ice. The structure is patterned with $\text{Ni}_{0.80}\text{Fe}_{0.20}$ (permalloy) nano-bars that act as individual spins, and its honeycomb structure demonstrates interactions similar to those of kagome spin ice. The advantage of the artificial approach to kagome spin ice is that the local spin configuration can be probed. Ground state properties such as correlation and entropy can be calculated statistically. This structure can also be tuned easily, allowing us to study certain effects in real spin ice.

In Chapter 2, I will introduce the general concept of frustration and the frustration in ice and spin ice. Chapter 3 explains how we design the artificial kagome spin ice, and how the spins are probed.

Chapter 4 discusses the ground state properties of artificial kagome spin ice and compares them with other spin ice experiments/models. The ice rule, the important restriction that governs the configuration of ice and spin ice, is observed. Correlations between near neighbors are calculated and compared with a nearest neighbor spin ice model, and dipolar effects are found to play a role in the spin configurations. We also introduced magnetic charge model and Shannon entropy concept to our artificial kagome spin ice. These concepts help to explain certain behaviors of the system and correlate them to other spin ice study.

Chapter 5 discusses the behaviors when we introduce disturbance into our system. Two disturbances are studied: magnetic field and stress (strain). We find chain-like flipping in the field induced magnetization process. Strain-like distortion in the pattern by lithography generates symmetry breaking or partial ordering, a phenomenon found in pyrochlore spin ice materials. Other factors that influence the magnetic symmetry of the system are also discussed.

Another kind of materials via nano-engineering is multiferroic or magneto-electric (ME) materials that is fabricated by self-assembly. There are ferroelectric phase and ferromagnetic phase simultaneously in this system and those two phases are coupled with each other through strain mediation. Because of the additional degree of freedom, there is current interest in using the materials for applications such

as memory that permits data to be written electrically and read magnetically [1], magnetic field sensors [2] and so on.

I introduce such a material BaTiO₃ (BTO) -CoFe₂O₄ (CFO) in thin film geometry with pillar like CFO phase and BTO matrix in Appendix C[3]. The focus of the chapter is the dielectric measurement for this material using a microwave microscope. It provides a method for film quality check and the basis for a proposed ME coupling measurement.

Chapter 2 : Frustration and Spin Ice

In this chapter, we introduced the general concept of geometrical frustration and model materials for that study – spin ice.

2.1 Frustration and geometrical frustration

Frustration is defined as the competition between the interactions in a system such that not all of them can be minimized simultaneously, due to local constraints. The concept was used to explain spin glasses' special behavior, such as time dependence of magnetization, by Phil Anderson [4]. Frustration is thought to be ubiquitous and has been a topic of constant interest over half century [5-7].

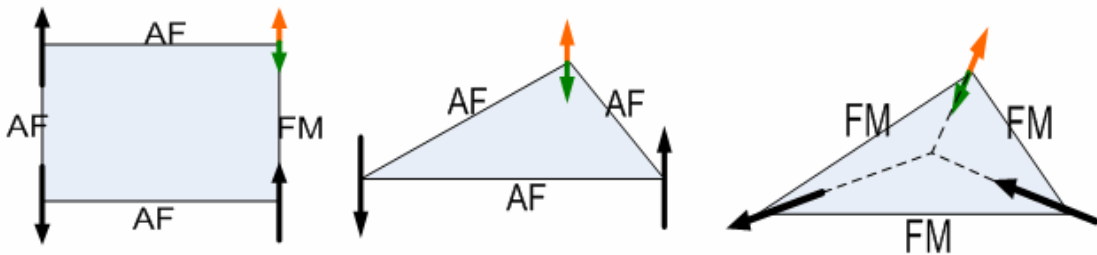


Figure 2.1 Illustration of geometrical frustration. Frustration of Ising spins on a square geometry due to introduction of a ferromagnetic interaction (Left); Geometrical frustration on a triangular geometry (center); and geometrical frustration with Ferromagnetic (FM) interactions (right). See Ref [8] .

For example, frustration was used to explain super-cooled liquid and glass transitions [[9]]. Another example is the argument that frustrated interactions are important to explain the way a one-dimensional protein folds into a living three-dimensional structure with a specific biological role [6].

Coming back to spin glasses, the origin of the behavior can either be a disordered structure (such as that of a conventional vitreous glass) or a disordered magnetic doping in an otherwise regular structure [4, 10, 11]. These both give us the first type of frustration, disorder-induced frustration, as illustrated in Fig 2.1 (left) by drawing a square geometry of Ising spins. If these spins are all coupled with anti-ferromagnetic (AFM) interactions, then energy of each bond can be individually minimized. However, if one of the bonds is made ferromagnetic (FM), then one spin is frustrated, unable to satisfy the constraints imposed by its neighbors [8].

The other type of frustration is geometrical frustration. In such systems, frustration arises without disorder, solely from the incompatibility of local interactions with global symmetry imposed by the crystal structure. It's also called frustration without disorder (or organized frustration). Geometrical frustration can be explained with spins in a triangular geometry, shown in Fig 2.1(center). Here each interaction is AF, but there is still a frustrated spin. The essential difference with the previous example is that an impurity was not necessary to produce frustration. Another geometrically frustrated example with FM interactions is illustrated in Fig 2.1 (right), where spin Ising direction is in plane connecting center to the corners.

The triangle symmetry can then be repeated to construct different lattices in 2D (Fig 2.2) and 3D (Fig 2.3). The frustration in these lattices is associated with a frozen-in disorder or ground state entropy. For example, the triangle lattice was found to have a ground state entropy of $0.323R$ (R is molar gas constant) as compared to the full spin entropy of $R\ln 2 = 0.693R$ (Residual entropy of Bethe lattice of triangles was calculated to be $R/3\ln 9/2 = 0.501R$). Note that the kagome lattice can be seen as

a Bethe lattice that develops into closed loop, or corner sharing triangular lattice. A corresponding 3-D structure for kagome is corner sharing tetrahedral, called pyrochlore structure, as shown in Fig 2.3.

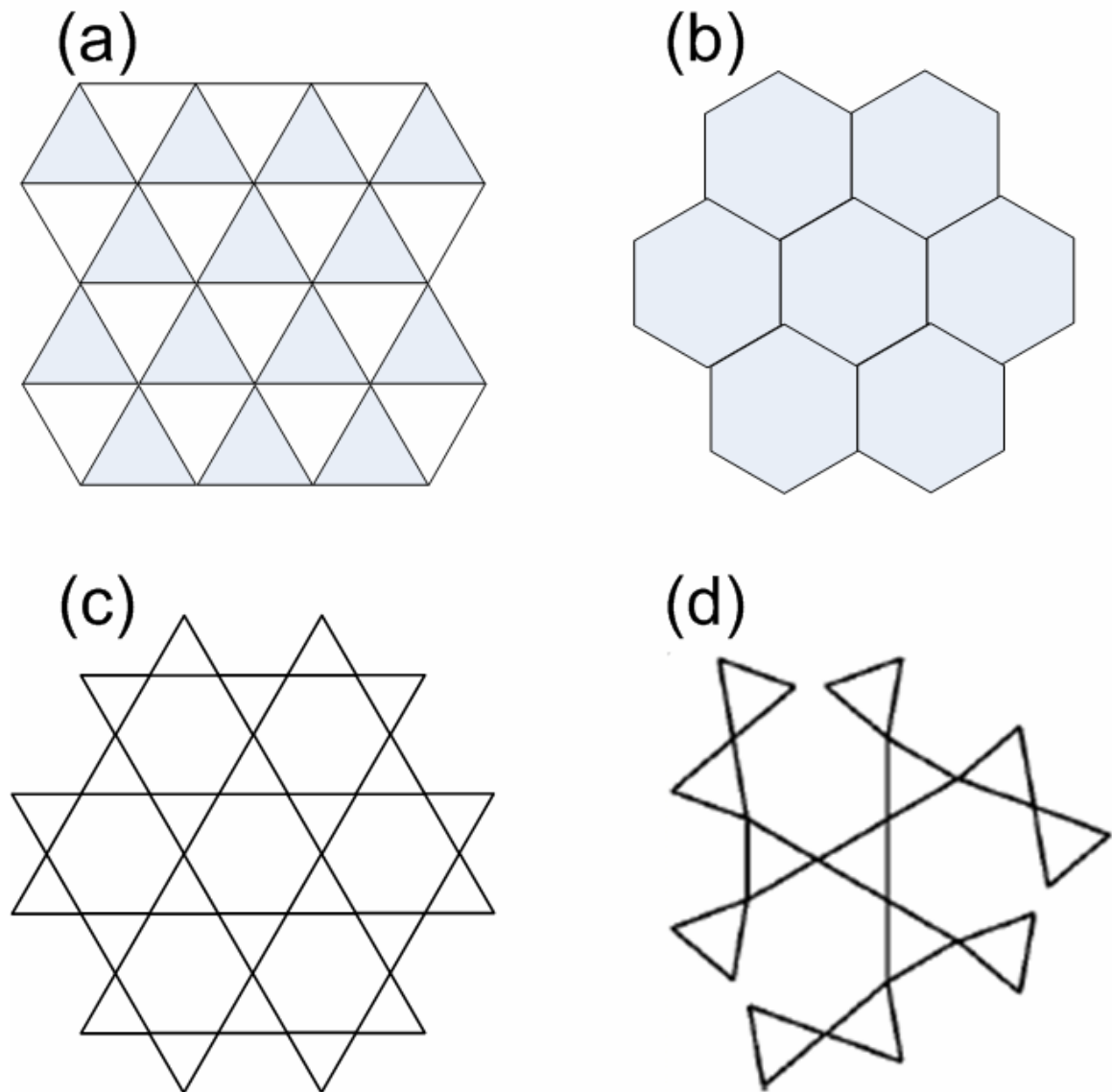


Figure 2.2 Different types of 2D lattices with triangular symmetry. (a) triangle lattice (b) hexagon honeycomb lattice (c) Kagome lattice (d) Bethe lattice (Reproduced from [8] and [12]). Kagome lattice is basically a closely connected Bethe lattice thus with more constraint.

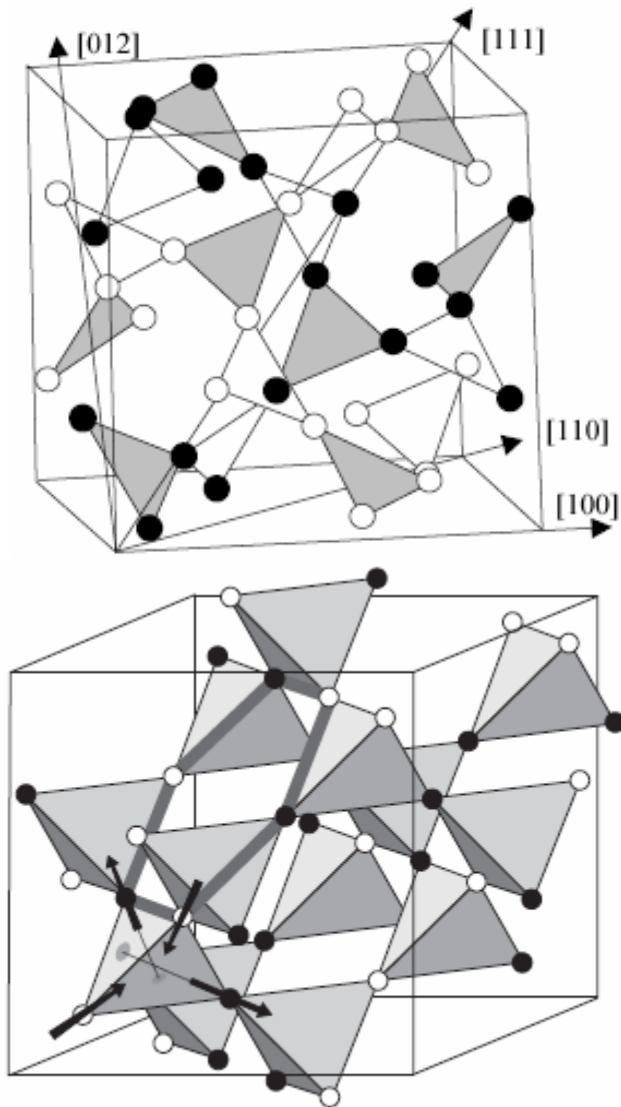


Figure 2.3 Different types of 3D lattices with triangular symmetry. (a) Garnet Lattice (b) pyrochlore lattice (Reproduced from [13] and [7]). Pyrochlore lattice is basically a closely connected Garnet lattice thus with more constraint.

2.2 Ice and ice rule

Historically, the first frustrated system identified was crystalline ice, which has a residual frozen-in disorder down to extremely low temperatures, a property known as residual or zero point entropy [14, 15]. This phenomenon was explained by Pauling[16], as illustrated in Fig 2.4a. Ice consists of oxygen atoms with four neighboring Hydrogen atoms (protons). These protons fall onto the lines connecting neighboring oxygen atoms. However, they are not at the center of these lines, rather, there are two minimum energy positions. Protons need to be either at a near position or a far position relative to oxygen. Not all of the oxygen-hydrogen interaction can be minimized when oxygen atoms form an ordered structure at low temperature. In other words, they are frustrated.

What Pauling noted was that there was a special type of proton disorder that obeyed the so-called “ice rules”, two protons are near to each oxygen (forming the traditional H₂O) and two are further away from each oxygen (being the hydrogen atoms of neighboring water molecules) [16]. This can be stated successfully as “two-in, two-out”. For four hydrogen atoms around one oxygen atom, there are 6 types of energetically equivalent arrangements complying with the ice rule out of the total 16 ways to distribute the hydrogen.

Pauling showed that the ice rule does not lead to order in the proton arrangement but rather, the ice ground state is “macroscopically degenerate” or energetically equivalent proton arrangements. Using the ice rule above, the number of available states is $2^{2N}(6/16)^N$ for a water crystal with N oxygen atoms, which leads

to a measurable zero point entropy $S_0 = R \ln 3/2$ related to the degeneracy, where R is the molar gas constant.

$$S_0 = R \ln(3/2) = 3.4 \text{ J/mole K} = 0.81 \text{ cal/mole K.}$$

Pauling's estimate of S_0 agrees well with experimental value of 0.82 cal/mole.K obtained by direct calorimetical measurements([14, 15]).

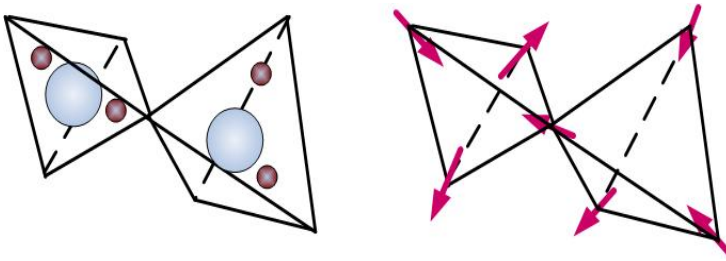


Figure 2.4 (Left) Local proton arrangement in water ice and ice rule; (Right) The spin configuration in the spin ice structure. The spin configuration obeys the ice-rule: 2-in, 2-out for each tetrahedron. Reproduced from [7].

There is an energetic barrier of the order of $\sim 1\text{eV}$ that prevents the hydrogen disorder from establishing long range order. However, it can relax into a lower entropy state through an extremely slow tunneling process below ice's freezing temperature,. From this point of view, the third law of thermodynamics is not violated [17]; it simply takes an exponentially long time for the ordered state to "anneal".

2.3 Spin ice

Although the disordered ice rule in water ice was eventually confirmed by neutron scattering [18], there has been a limited experimental study of frustration and organization of disordered state in general. This leaves the door open for research in

magnetic systems because magnetic materials are easy to study by a battery of experimental techniques, and there is a large variety of diverse magnetic materials that can be chosen to approximate simple theoretical “toy models” of collective behavior[7]. Towards this end, Harris *et al.* first proposed the name “spin ice” as a concept of frustrated spin alignment [19]. Spin ice materials normally adopt the cubic Pyrochlore structure with form of $A_2B_2O_7$. Here A is usually rare earth magnetic ion (Ho^{3+} , Dy^{3+}) occupying the four corner positions of corner sharing tetrahedra, shown in Fig 2.3b on the lower left downward tetrahedron (arrows), with Ising anisotropy directed along the $\langle 111 \rangle$ -type directions, connecting a spin with the center of its tetrahedron, pointing into or out from the center. The spins here are equivalent to the proton displacement vectors. B is non-magnetic ion (Ti^{4+} , Sn^{4+}).

Each A ion has a particularly large magnetic moment of approximately $10 \mu_B$ that persists to the lowest temperatures. Each tetrahedron of A ions has an oxide ion at its center, so two of these oxide ions lie close to each A along the $\langle 111 \rangle$ crystallographic axis. The anisotropic crystallographic environment changes the quantum ground state of A such that its magnetic moment vector has its maximum possible magnitude and lies parallel to the local $\langle 111 \rangle$ axis. The first excited state is several hundreds of Kelvin above the ground state. At temperatures of the order of ten Kelvin or below, the excited states are not accessed thermally. The A moments therefore behave as almost pure two-state spins that approximate classical Ising spins pointing in or out of the tetrahedron.

The spin ice structure is frustrated because the neighboring interaction among spins favors an in–out arrangement, but not all pairs of neighbors can be satisfied

simultaneously. The 2-in, 2-out configuration in any one tetrahedron arises from the combined effect of magnetic coupling and anisotropy described above, because for each tetrahedra, the best low energy compromise leads to the 2-in 2-out configuration. This local organizing principle is exactly analogous to the property of protons of water ice [20].

Frustration in spin ice leads to exotic disordered states even at low temperatures like water ice, however spin ice materials lend themselves more ready to experiments than water ice, revealing much about the basic physics of disorder [17, 21, 22]. Currently, the spin ice model has been approximately realized by many real materials, most notably the rare earth pyrochlores $\text{Ho}_2\text{Ti}_2\text{O}_7$, $\text{Dy}_2\text{Ti}_2\text{O}_7$, and $\text{Ho}_2\text{Sn}_2\text{O}_7$. Experimental methods that can be used to study spin ice include susceptibility, specific heat measurements, neutron scattering, muon spin relaxation (μSR) among others [8], as described below.

Specific heat measurement

In spin ice, ground state spin configurations and correlations relate to spin ice rule, ground state entropy and degeneracy. Entropy and degeneracy associated with spin ice rule have been directly measured by specific heat experiments [17], and are consistent with prediction of a spin ice model which suppose there is an ice-rule obeying spin ice state in $\text{Dy}_2\text{Ti}_2\text{O}_7$. This is shown in Fig 2.5.

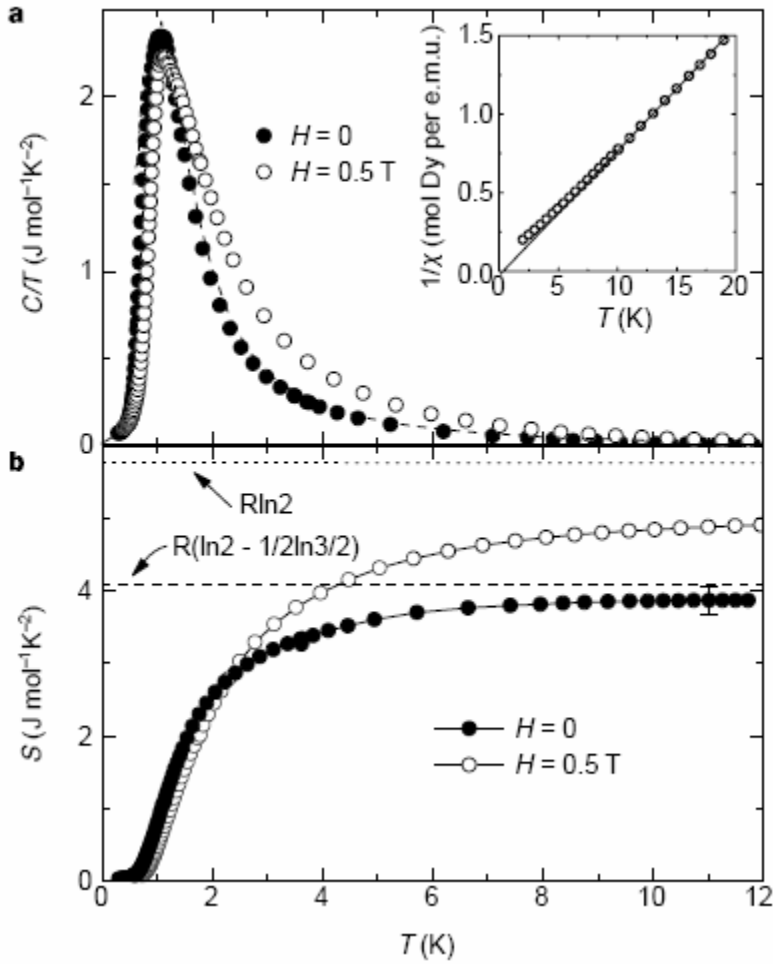


Figure 2.5 Specific heat measurement and entropy calculation for $\text{Dy}_2\text{Ti}_2\text{O}_7$ spin ice. Reproduced from [17].

The approach of Ramirez *et al.* was to integrate the magnetic specific heat between the frozen regime ($T_1=300\text{mK}$) and the paramagnetic regime ($T_2=10\text{K}$) where the expected entropy should be $R\ln 2$ for a two state system. The magnetic entropy change, ΔS , was determined by integrating $C(T)/T$ between these two temperatures:

$$\Delta S_{1,2} = \int_{T_1}^{T_2} \frac{C(T)}{T} dT$$

Fig 2.5a shows $C(T)/T$ changes with temperature. The broad maximum occurs at a temperature $T \sim 1.2\text{K}$, which is of the order of the energy scale of the magnetic interactions in that material. The specific heat has the appearance of a Schottky anomaly, indicating two energy levels. At the low temperature side of the Schottky peak, $C(T)$ falls rapidly towards zero, indicating an almost complete freezing of the magnetic moment.

Fig 3.5b shows that the magnetic entropy recovered is approximately 3.9 J/mol K , which is considerably smaller than the value $R \ln 2 = 5.76\text{ J/mol K}$. The difference, 1.86 J/mol K is quite close to Pauling's estimate for the entropy associated with the extensive degeneracy of ice $R/2 \ln 3/2 = 1.68\text{ J/mol K}$ [16].

Neutron scattering

Neutrons interact with internal magnetic fields in the sample. The strength of the magnetic scattering signal is often very similar to that of the nuclear scattering signal in many materials, which allows the simultaneous exploration of both nuclear and magnetic structure.

Fig 2.6 left panel shows the elastic neutron scattering pattern of $\text{Ho}_2\text{Ti}_2\text{O}_7$ at $T \sim 50\text{mK}$ and it is compared with the predictions of the near neighbor and dipolar spin ice models [23]. The simulation for near neighbor spin ice successfully reproduces the main features of the experimental pattern but there is visible difference about the intensities. The dipolar model successfully accounts for the differences between experimental pattern and the near neighbor model, specifically the relative intensities

of the regions around $(0\ 0\ 3)$ and $(3/2\ 3/2\ 3/2)$, and the diagonal broad features.

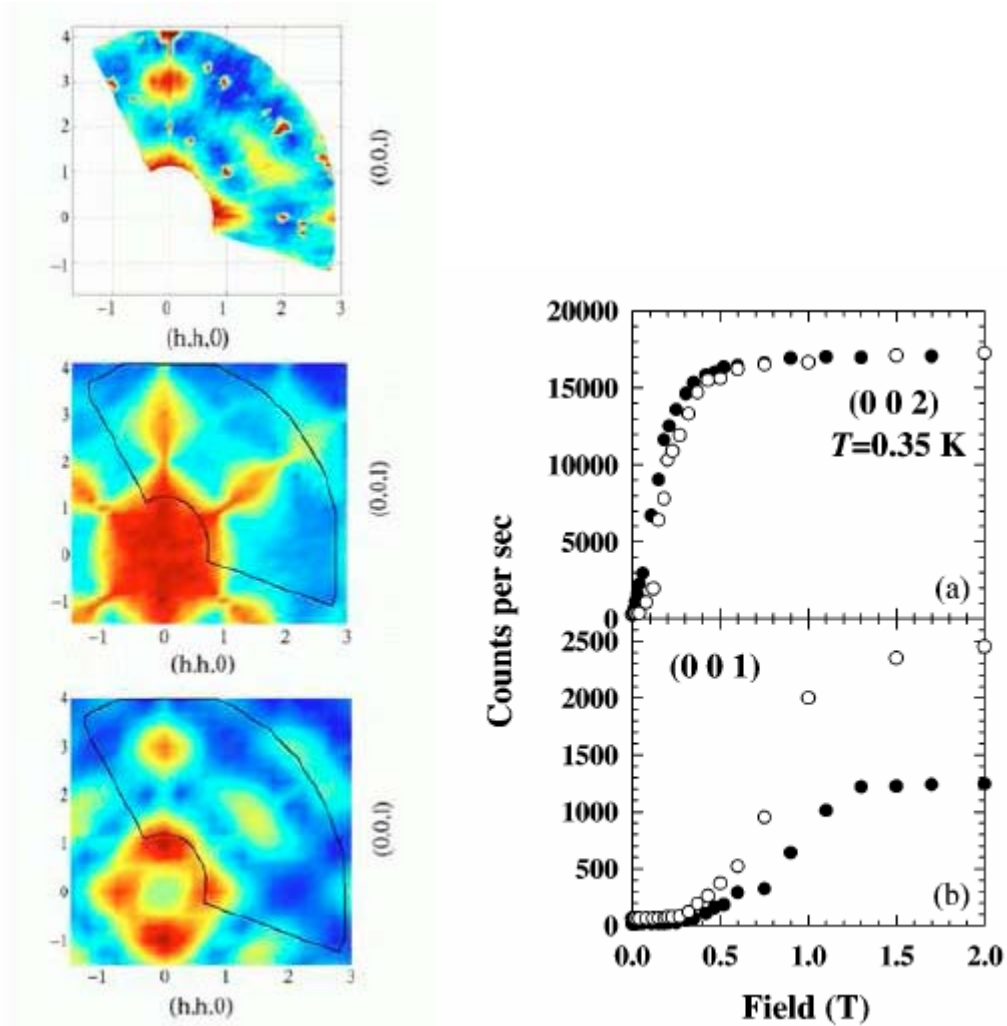


Figure 2.6 (Left) Experimental neutron scattering pattern of $\text{Ho}_2\text{Ti}_2\text{O}_7$ in the (hhl) plane of reciprocal space at $T = 50$ mK [23] (A) compared with simulated neutron scattering for the nearest neighbor spin ice model at $T = 0.15$ J (B), and simulation from the dipolar spin ice model at $T = 0.6$ K (C); (Right) Magnetic field dependence of the scattering from $\text{Ho}_2\text{Ti}_2\text{O}_7$ at a sample temperature of 0.35 K, at (a) the $[002]$ position, and (b) the $[001]$ position. The measurements shown by the full circles were made after cooling from high temperatures in zero-field, while the open circles show the behavior after an initial field of 0.5 T was applied and then removed before beginning the measurements. This reveals the field-dependent behavior of the frozen-in magnetic order [19].

Correlations and magnetic field effect have been measured by magnetization and neutron scattering [19, 24]. Harris found that magnetic scattering in zero-field shows no significant change in the intensities of any Bragg peaks while cooling the crystal from 300K to 0.35K concluding that there is no phase transition to a magnetically-ordered state in zero-field. Instead, strong magnetic diffuse scattering was detected at 0.35 and 1.8K. The ridge of scattering sharpens upon cooling to 0.35K, showing that the ferromagnetic order is on a scale of one to two nearest neighbor distances at 1.8K, and increase to between three and four distances at 0.35K. The field-dependent neutron scattering measurements also suggest that, upon applying magnetic field, ground-state degeneracy is broken and a long range magnetic order is formed. An ordered structure is predicted from the experimental data.

As we have seen above, although experiments on spin ice materials have exhibited rich results about frustration and ice rule related properties, there are many limitations about this study. For example, the specific heat measurement requires extremely low temperature; the local spin configuration and complicated order-to-disorder transition may not be inferred from bulk experiments.

2.4 Meta materials

One of the most fascinating aspects of geometrically frustrated magnets is how the spins locally accommodate the frustration of the spin-spin interactions. On the other hand, probing the spins locally and studying how they accommodate the

frustration is still a challenging topic in experiments for real materials. To overcome these problems, we introduced "meta-materials" concept in this study.

Originally meta-material is a concept in which a material gains its properties from its structure rather than directly from its composition. This term is particularly used when the material has properties not found in naturally-formed materials. For example, all known transparent materials possess positive values of ϵ and μ , thus have positive refractive index. However, some engineered meta-materials can have $\epsilon < 0$ and $\mu < 0$. Such materials are referred as "left-handed". This idea was verified by experiments working in the microwave frequency range 2001[25, 26]. A more recent meta-material example is shown in Ref [27, 28], where they used colloidal spheres to fabricate three-dimensional periodical artificial structure that do not allow the propagation of photons in all directions with a wavelength in the visible region (see Fig 2.7).

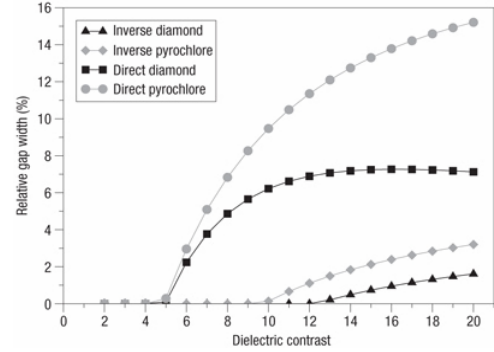
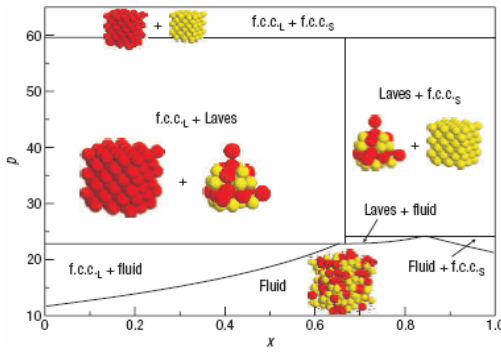
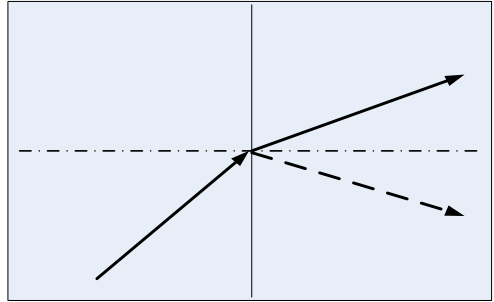
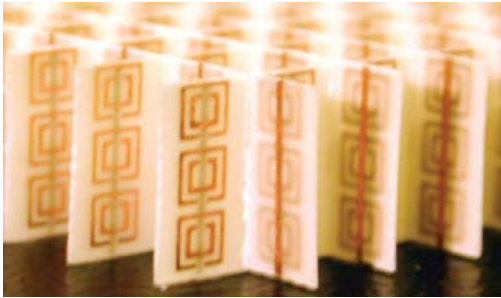


Figure 2.7 Examples of meta-materials with artificial structures. (Top) Artificial structure that gives negative refractive index [25]; (Bottom) three-dimensional periodical artificial structure that do not allow the propagation of photons in all directions with a wavelength in the visible region[27].

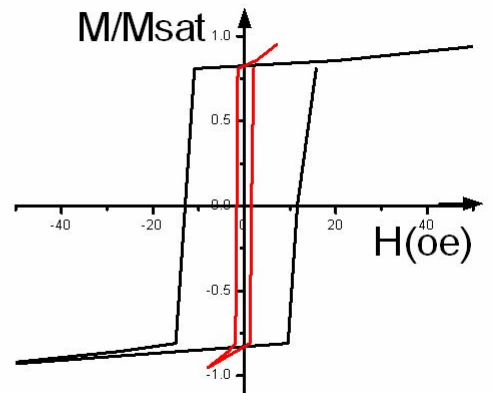
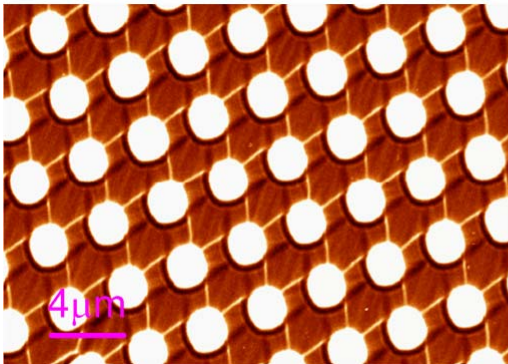


Figure 2.8 Ni-Fe magnetic film with perforated holes shows hard magnet properties.

Although meta-materials are of particular importance in optics and photonics, this concept can be expanded to magnetic materials. Previous studies done by our group on a perforated permalloy film have shown that the coercive field is considerably larger than for a uniform film, an obvious super-hard magnet, due to the domain wall pinning by the holes (Fig 2.8)[29].

In this thesis, we refer "meta-material" or artificial system as a system specially designed in attempt to mimic the behavior of ice, but it is created out of completely different substances. Like other meta-materials, the desirable properties of the system come from the designed geometry as well as the materials.

Chapter 3 : Artificial Kagome Spin Ice

Spin ice study generates significant interest because the frustration and ice rule restriction together import the materials with many interesting properties. However, conventional materials exhibit several limitations, including limited choices of experimental materials and absence of an effective probe for individual spin. In this chapter, we discuss an artificial approach for this study - using nanotechnology to fabricate structures that mimic the geometry and interaction in real spin ice. We present the designed model lattice, fabrication methods and probing techniques.

3.1 Artificial spin ice

Conventional geometrically frustrated materials like spin ice materials have significant limitations, including 1. Limited choices and modification. 2. Critical experimental conditions like very low temperature and high magnetic field. 3. Absence of an effective probe for investigating local spin configurations or defects.

A more recent option is to use the tools of nanotechnology to custom tailor a system that is analogous to real materials. Wang *et al.* studied a two-dimensional square lattice of single-domain nanoscale ferromagnetic islands [30]. The permalloy islands were sufficiently small (80nm x 220nm and 25nm thick) that the atomic spins were ferromagnetically aligned in a single domain along the long axis, but large enough so that the moment configuration was stable at 300K. Using a Magnetic Force Microscope (MFM), individual spins were probed, which is experimentally difficult in real materials (Fig 3.1).

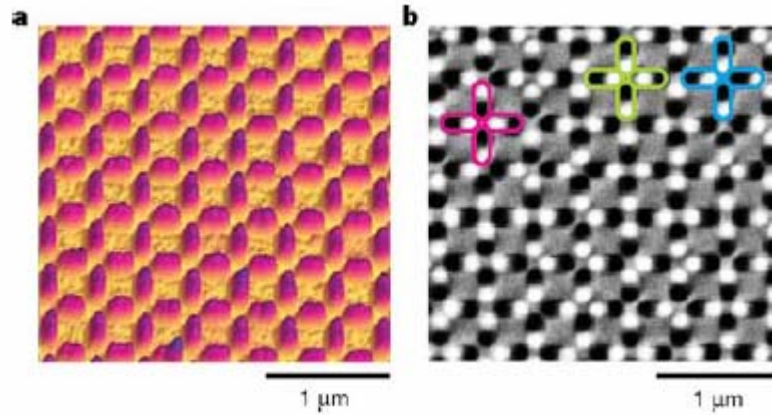


Figure 3.1 Atomic Force Microscope (AFM) and Magnetic Force Microscope (MFM) images of frustrated square lattice[30]. (a) AFM image shows an array of permalloy nano-islands. The magnetic islands are about 220nm long, 80nm wide and 25nm thick. (b) MFM images taken from the same array shows each island has black and white contrast, indicating the magnetization directions. The colored outlines indicate examples of different type of vertices.

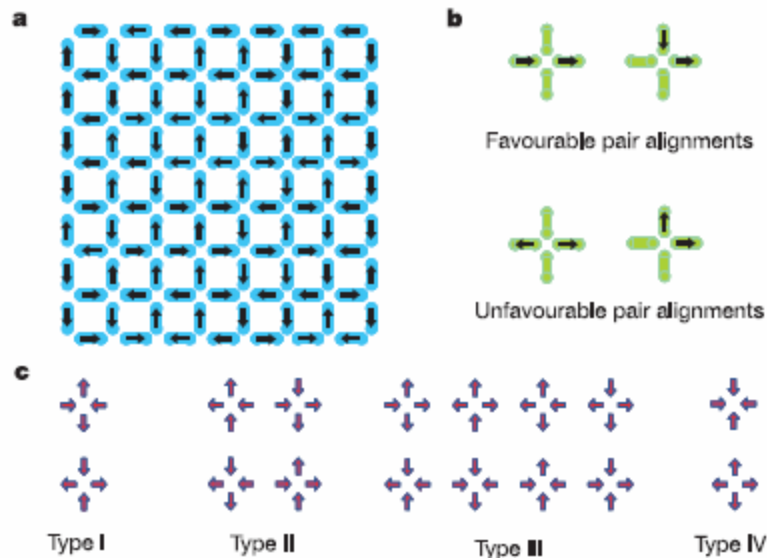


Figure 3.2 Illustration of frustration on the square lattice. (a) each island in the lattice is a single-domain ferromagnet with its moment pointing along the long axis. (b) vertices of the lattice with pairs of moments are indicated. (c) 16 possible moment configurations on a vertex of four islands, separated into four topological types. Reproduced from [30].

A square geometry like this is frustrated because each vertex of four islands has 16 possible moment configurations, among which type I and II have lower energy

because two moments point into the vertex center and two moments point out. Type III and IV configurations are unfavorable because the three-in one-out or four-in configurations have relatively higher energy. The square lattice can be seen as an experimental realization of the spin ice square model [31].

This artificial square lattice is attractive because it provides an approach to probe individual spins and use this model system to study disordered systems. Unfortunately, the system of Wang *et al.* does not completely show the effects of spin ice frustration[20, 32]. This system should instead prefer an anti-ferromagnetic ordered state because the 6 interactions at each vertex are not equivalent to one another. Moreover, a significant fraction of interactions are shown to disobey the essential (2-in, 2-out) ice rule[32]. These shortcomings leave a large scope for further study.

As we discussed above, one possible problem for the square lattice is that it should prefer an alternative, anti-ferromagnetic ordered state [33] because the 6 interactions at each vertex are not energetically equivalent. This is shown in our OOMMF simulation of a similar square vertex structure (Fig 3.3). When the elements are isolated islands like in Wang *et al.* paper, the two types of 2-in-2-out configuration have different energy in the demagnetization mode. The energy minimum state slightly prefers type I configuration. In a square lattice constructed with this type of vertices, an ordered pattern is possibly the true minimum energy state, where the arrows of alternate squares have the same configuration (AFM, Fig 3.4). When we connect the islands at the center of the vertex, the low energy state changes to type II, and the ordered lattice prefers a FM type configuration.

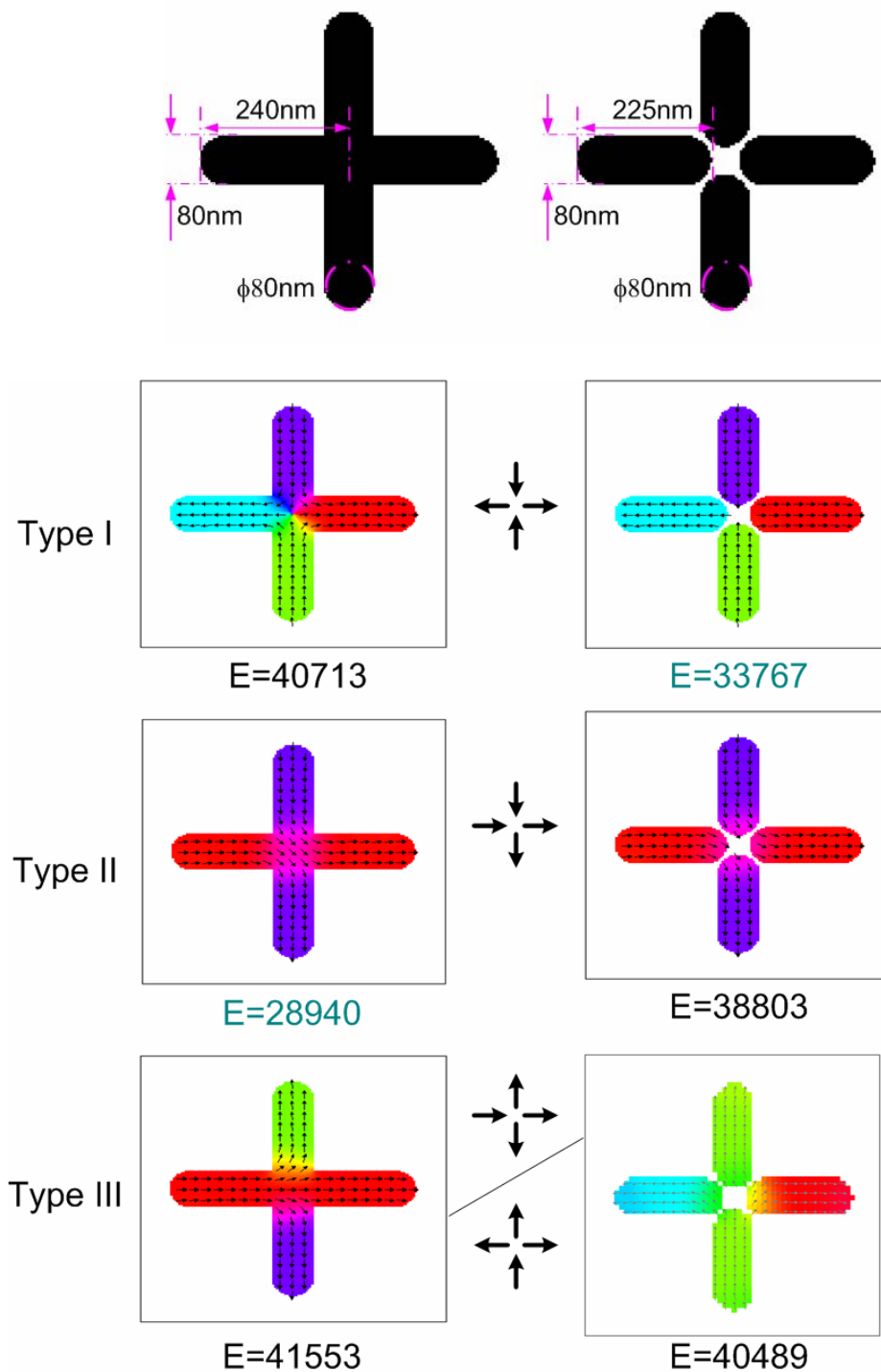


Figure 3.3 OOMMF simulations of the square vertex with different moment configurations. Left, simulation with square vertex of connected islands suggests that the low energy configuration is type II. Right, simulation with square vertex of isolated islands suggests type I has the lowest energy. Energy units: J/m^3 . Please see table I for detailed exchange energy and dipolar energy value for each simulation.

Table I OOMMF simulated exchange energy and dipolar energy value for different moment configuration of square vertex.

(a) Vertex with connected islands

Units: J/m^3	Type I	Type II	Type III
E_{exchange}	13093.6	2719.2	4416.1
E_{demag}	27620.1	26211.3	37137.2
E_{Total}	40713.7	28940.5	41553.3

(b) Vertex with isolated islands

Units: J/m^3	Type I	Type II	Type III
E_{exchange}	84.7	1443.0	2616.8
E_{demag}	33683.9	37360.4	36873.1
E_{Total}	33768.6	38803.4	40489.9

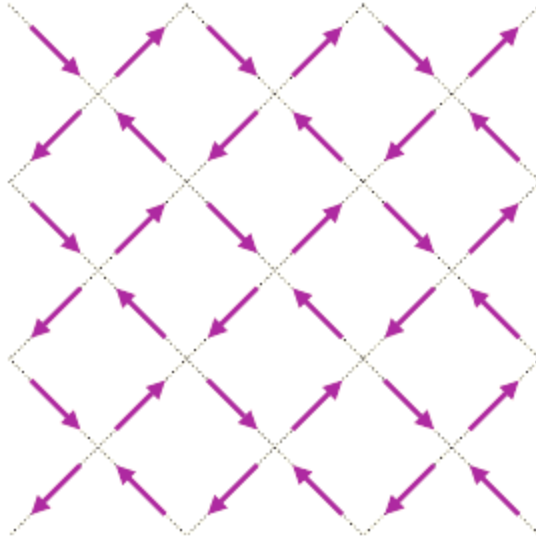


Figure 3.4 Possible true minimum energy state of artificial square spin ice. The arrows of alternate squares have the same configuration. Reproduced from [20].

The reason that many vertices do not obey the ice rule might be that there are not strong enough interactions between neighboring elements. As for the square lattice, the energy difference between type I 2-in 2-out configuration and 1-in 3-out configuration is only 19.9% - 40.6%. Connecting the elements in the square lattice could increase the energy difference in principle; however the six pair interaction in a connected square lattice vertex are not equivalent to each other, as predicted in OOMMF simulation (Fig 3.3), and connecting the elements would shift the preference from AFM to FM ordering.

3.2 Kagome spin ice

Following Tanaka et. al. [34], we bring two innovations to the artificial spin ice approach[35] and we show that by employing these two innovations, we realize an artificial spin ice system that rigorously obeys ice rule, thus providing a sought-after model system appropriate for further studies. Furthermore, correlations in our

artificial spin ice system suggest a strong role for dipolar effects, an essential component of spin ice models.

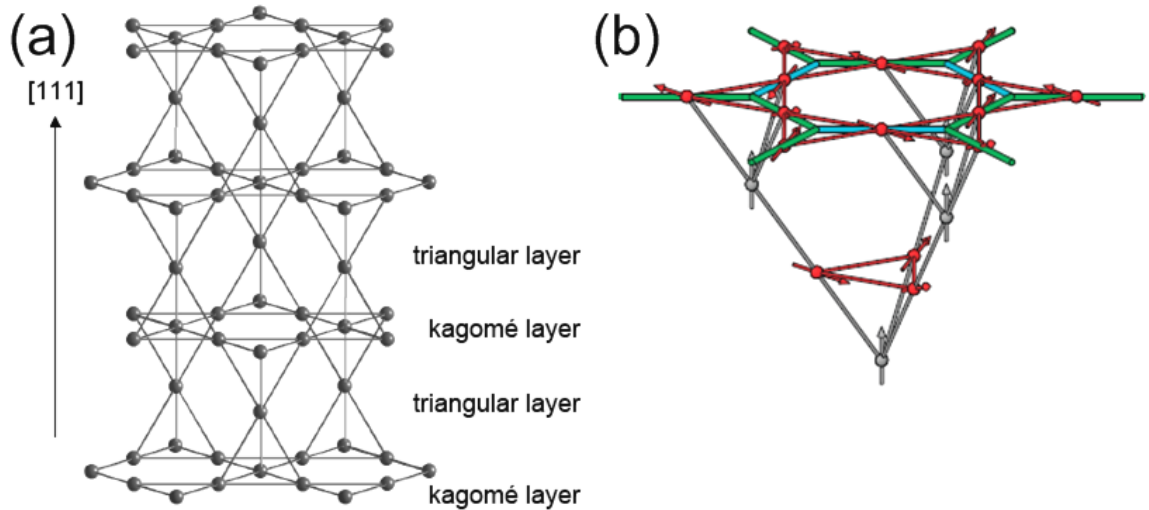


Figure 3.5 Layer structures of pyrochlore lattice. (left) Stacking layer feature of pyrochlore structure along [111] direction: having alternative Kagome/triangle layers. (Right) the kagome layer when applying a field along [111] direction. Reproduced from [36] and [37]. See also Ref. [7].

Our first innovation is the use of a kagome lattice instead of a square lattice. The kagome lattice is a two-dimensional structure composed of corner-sharing triangles and is an essential component of the pyrochlore spin ice structure (see Fig 3.5) [32, 34, 38, 39]. Compared to the 2-in 2-out configuration in the pyrochlore structure, here the ice rule changes to 2-in-1-out or 1-in 2-out for each vertex (see Fig 3.6a). Because there are six energetically-equivalent configurations out of a total of eight (see Fig 3.6c), the kagome lattice is more under-constrained than the square-ice lattice [40].

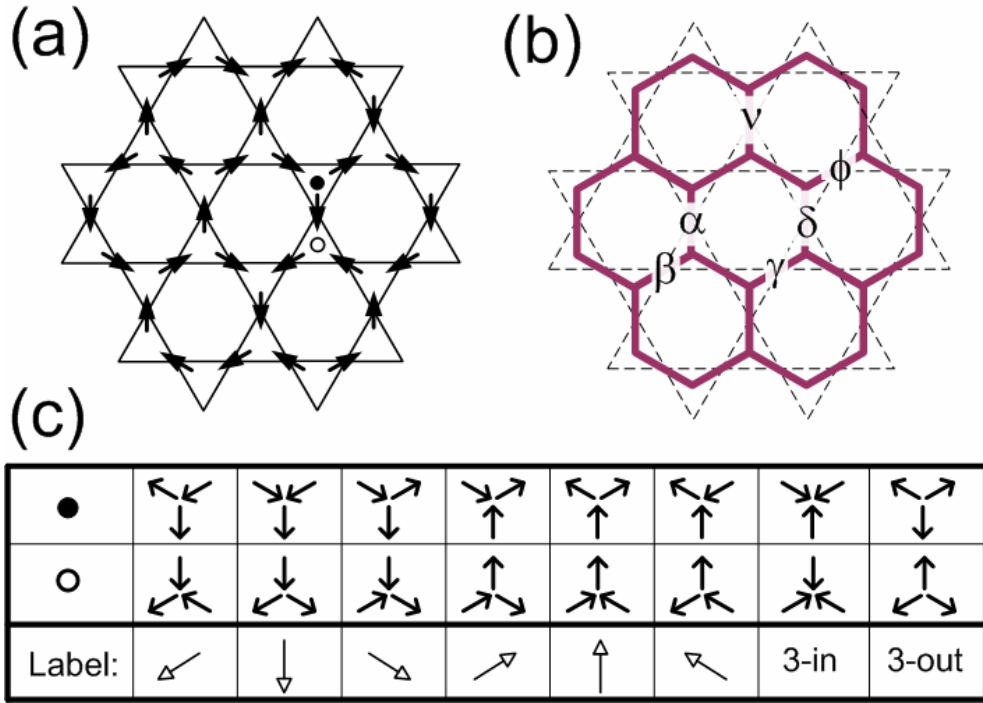


Figure 3.6 Sketch of kagome spin ice and its ice rule. (a) A sketch of the kagome spin ice lattice showing 30 spins. The two sub-lattices on which interaction vertices can occur are labeled by ● and ○. (b) Honeycomb structure formed by connecting the spins of the kagome lattice. Each bar element represents a spin magnetic moment oriented along the bar axis. The Greek symbols label spins for later use in correlation calculations. (c) The possible spin configurations at a single vertex. Spin configurations that obey the ice rule produce a net magnetic moment at each vertex, which we use to label the allowed spin configurations. The two configurations that produce no net magnetic moment (3-in and 3-out) are not energetically favorable.

The second innovation we introduce is to lengthen the magnetic islands until they become physically connected at the center of the kagome triangles, creating a honeycomb structure (Fig 3.6b) and thus increasing the strength of the spin interactions via ferromagnetic exchange[34]. The ‘spins’ are now no longer the moment of isolated islands, but rather they are the axial moments of connected magnetic nanowires. The lines of the honeycomb are 500nm long, 110nm wide and 23nm thick. At this scale, micromagnetic simulations[41] indicate that the connecting elements are magnetized along their axis and act as macroscopic single spins with energy differences among the different configurations that support the ice rule assumption[42]. OOMMF simulation shows that the energy difference between 2-in 1-out (1-in 2-out) and 3-in (3-out) is as big as 72.39% or 38.2% for connecting vertex and non-connecting vertex respectively. With strong analogies to real spin ice, these simulations show that 85% of this nearest neighbor energy difference comes from dipolar field, with the remaining 15% coming from exchange energy due to the domain walls at the vertices (See Fig 3.7 and Table II).

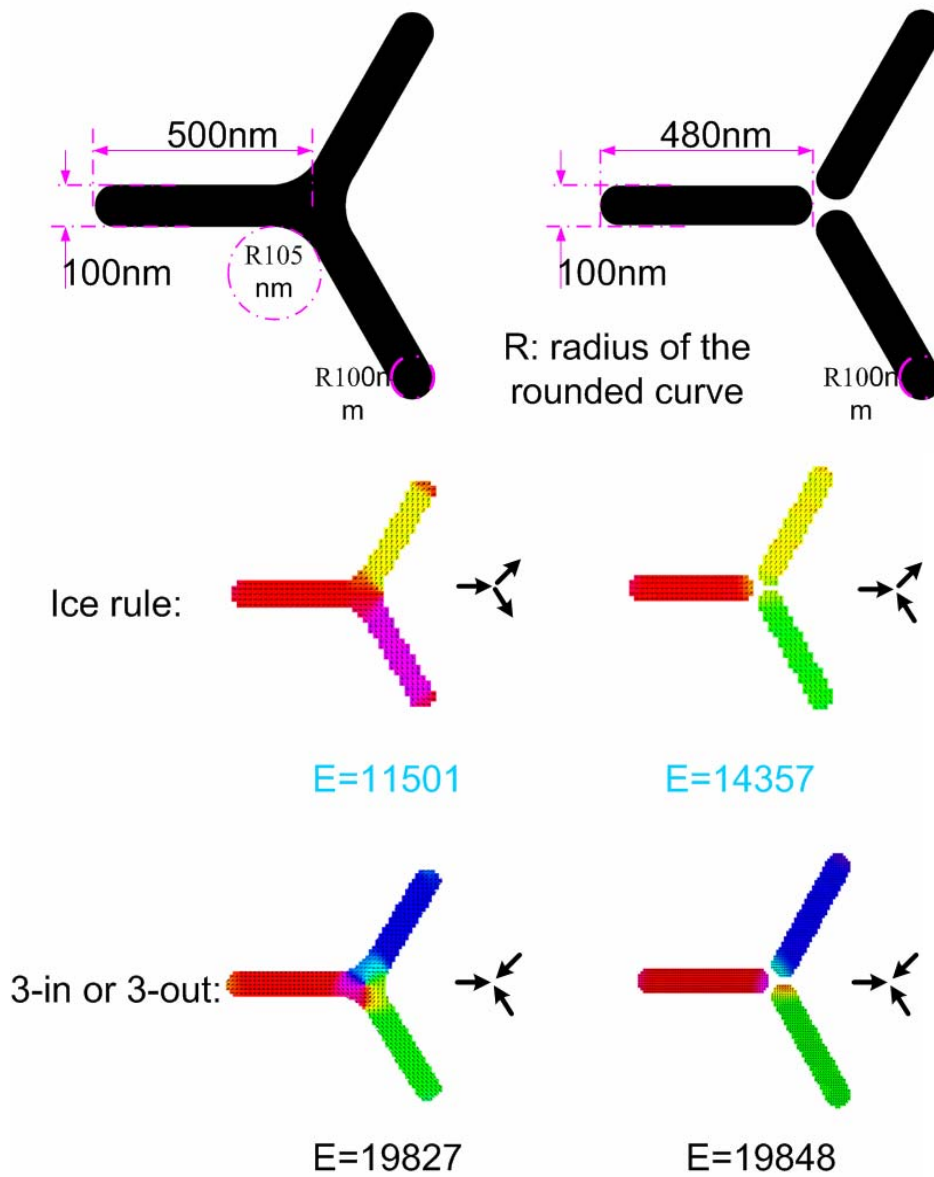


Figure 3.7 OOMMF simulations of the kagome vertex with different moment configurations. The energy values calculated suggest 1-in 2-out or 2-in 1-out ice rule configuration preference in these vertices. Energy units: J/m^3 .

Table II OOMMF simulated exchange energy and dipolar energy value for different moment configuration of triangular vertex.

(a) Vertex with connected islands

Units: J/m^3	1-in 2-out or 2-in 1-out	3-in or 3-out
E_{exchange}	610.8	3439.9
E_{demag}	10891.9	16388.6
E_{Total}	11502.7	19828.5

(b) Vertex with isolated islands

Units: J/m^3	1-in 2-out or 2-in 1-out	3-in or 3-out
E_{exchange}	260.7	889.3
E_{demag}	14097.3	18959.6
E_{Total}	14358.0	19848.9

3.3 sample fabrication

The sample fabrication process is a combination of electron beam lithography, thin film deposition, and lift-off. We employed a bi-layer resist lithography which could be found in general references[43-45] and illustrated in Fig 3.8. First, PMMA 495 and PMMA 950 bi-layer resists are applied in two steps on the commercially available SiN membrane substrate [46] prior to electron beam exposure. The SiN has a nice amorphous surface and is transparent to electron beam for Transmission Electron Microscope (TEM) observation. PMMA 495 and 950 PMMA are ultra-high resolution, high current positive resist used for nanolithography, and this bi-layer structure generates an undercut when exposed to e-beam and is easier for lift off. A solution of methyl isobutyl ketone (MIBK) and isopropanol (IPA), with relative volume ration of 1:3, is used to develop PMMA after exposure to the electron beam. Then we deposit 25 nm permalloy ($\text{Ni}_{0.80}\text{Fe}_{0.20}$) and 3 nm aluminum capping layer on the sample using electron beam evaporator with a deposition rate of 0.8 Å/s at ambient temperature. In the final step, we use PRX-127 to remove the PMMA bi-layer. This lift-off process leaves only permalloy islands (with Al capping layer) on the substrate. A detailed lithography recipe can be found in Appendix B at the end of this dissertation.

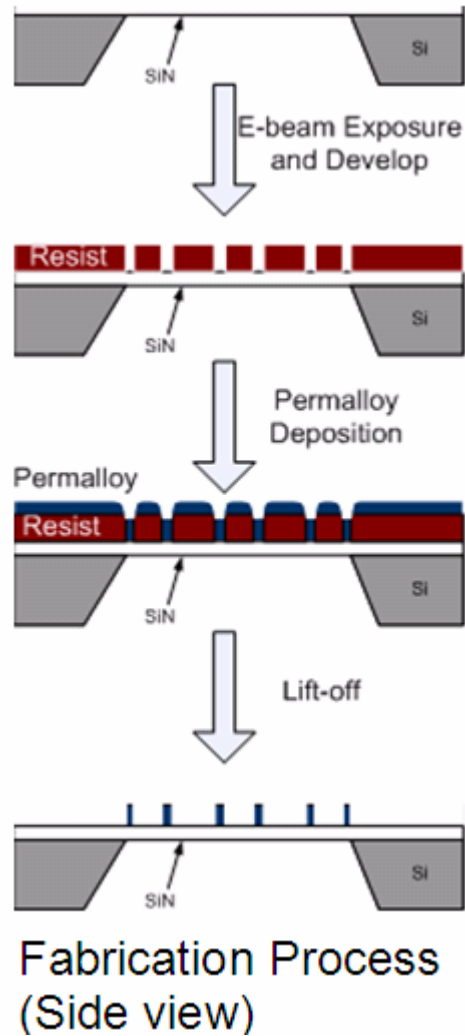


Figure 3.8 Illustration of fabrication process. From top: commercially available SiN membrane TEM grid; part of resist (wanted geometry) is removed after e-beam lithography and development; Permalloy film deposited on SiN membrane and remaining resist; remaining resist removed by lift-off.

Fig 3.9 and 4.10 display TEM images of connected and isolated kagome lattice arrays with lattice constant of 500nm. The total number of elements in our realization is 12,864, large enough for ensemble results comparable to Monte Carlo simulations[12].

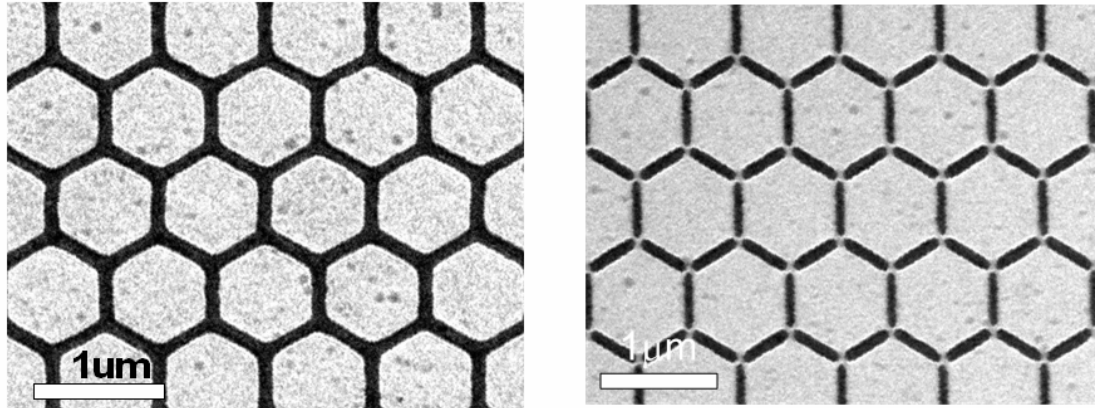


Figure 3.9 TEM images of our fabricated kagome lattice with connected islands (left) and isolated islands (right).

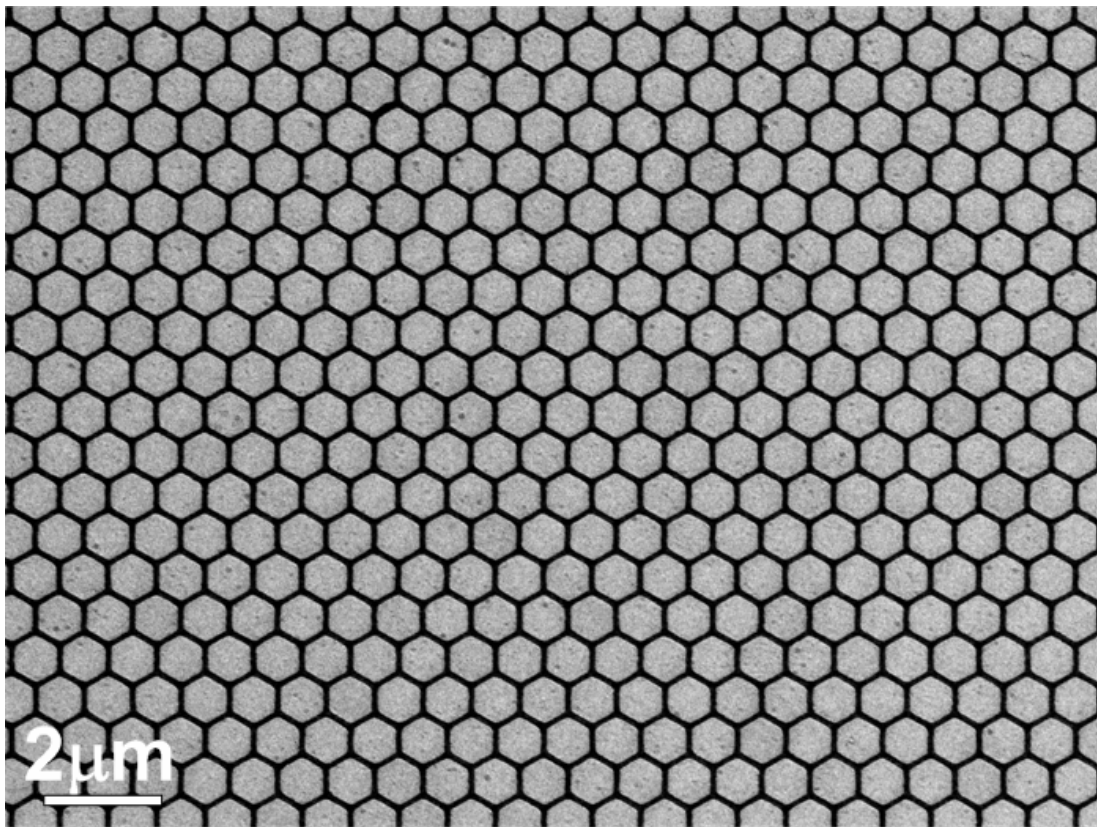


Figure 3.10 TEM picture of our fabricated lattice with a larger field of view.

3.4 Spin direction detecting- Lorentz TEM

To determine the directions of the single-domain elements, we employ a TEM operated in Lorentz imaging mode. The Lorentz transmission electron microscope was first used to image domains by simply defocusing the objective lens [47, 48]. The observed contrast can be understood qualitatively in terms of the Lorentz force acting on the moving electrons as they travel through the magnetic foil (See Appendix A.)

For single-domain needle-shaped elements used in our structure, we use a standard contrast transfer function [49] to simulate the contrast of. Fig 3.11 shows that Lorentz contrast simulation of a magnetic bar elements has over-focus Lorentz contrast featuring a dark edge and a bright edge depending on the magnetization direction. The TEM images verified the simulation. Simply, this can be explained by deflection of the e-beam by Lorentz force when it passes through a magnetic element. The detail description of contrast transfer function and a Matlab code we used to generate Lorentz contrast can be found in Appendix A at the end of this thesis.

Using a right-hand rule, we can uniquely specify the magnetization direction for each element, as shown by the colored arrows (Fig 3.12). We verify the magnetic origin of the contrast both by through-focus imaging and by in-situ field reversal.

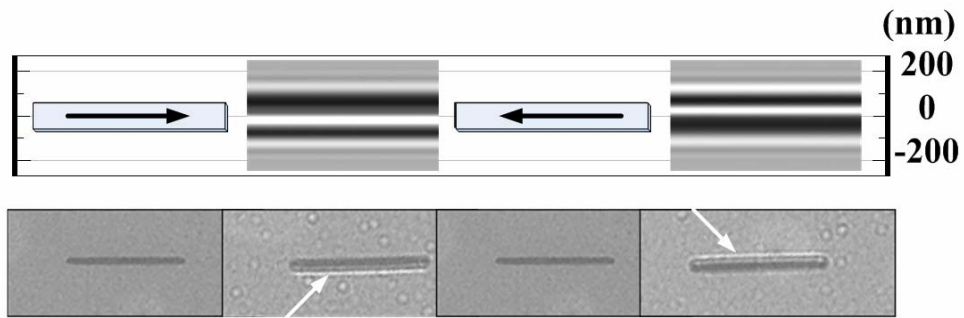


Figure 3.11 Contrast transfer function simulation and Fresnel image of magnetic bar elements. Both show bright fringes running along the long edges of each element; from these the magnetization orientation can be deduced.

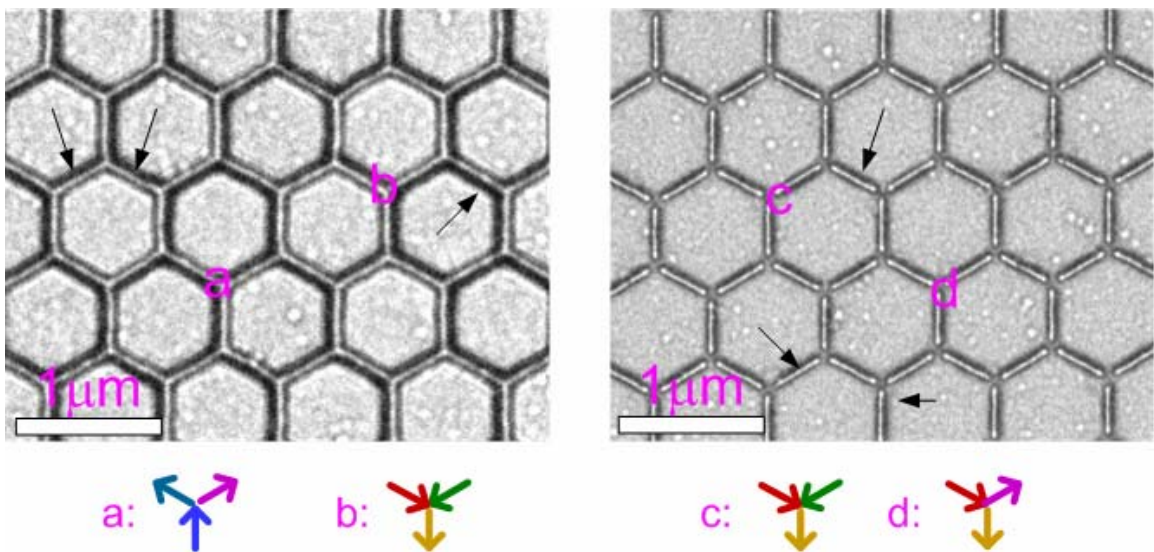


Figure 3.12 Lorentz TEM images of the kagome lattice with connected elements (Left) or isolated islands (right). The arrows in the images show dark fringes along the long edges of each element. We used right-hand rule to determine the spin directions for each elements, as shown by examples.

3.5 Demagnetization protocols

In thermodynamics, a disordered materials can be brought into a remarkable stable state through annealing, i.e., cooling down the materials rather slowly. For spin ice study, annealing was also used to drive spin ice materials into their ground state. During annealing process, thermal noise can help to escape high-energy local minima, and materials could reach a rather optimized state after long time. However, in our artificial spin ice the magnetization state and moment configurations are very stable at room temperature due to their relatively large interaction. The interaction energy between nearest neighbors is of the order of 10^{-19}J , or equivalent to 10^4Kelvin [30].

Here we used another procedure which is commonly used to demagnetize disordered magnets and is experimentally known to result in a very stable state: the application of an oscillating external field [50],[51, 52]. This procedure makes uses of another type of noise, a random external field, to help escape their local interaction. Study shows the ac demagnetization procedure can result in an optimized state for a magnetic disordered system[50].

Fig 3.13 shows the setup for the demagnetization procedure. We put the sample in rotating table which is located in an ac external field. The field steps down from above the coercive field for our nanoscale permalloy elements (1600Oe) to zero. Fig 3.14 shows the field change during the demagnetization procedure. We used a time period of $t=2.2\text{s}$, rotating speed = 90Hz, and the magnetic field step of 2Oe. One entire demagnetization run is 800 cycles and takes about 30 minutes.

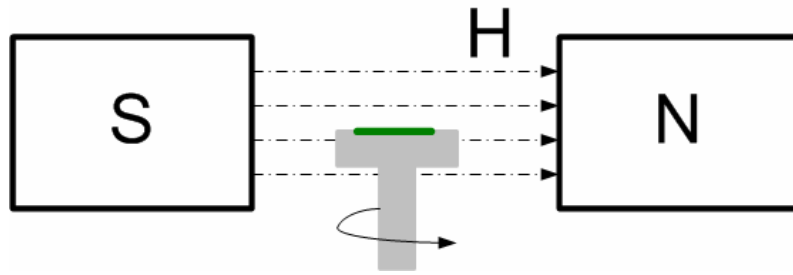


Figure 3.13 Illustration of the demagnetization setup. Kagome spin ice sample was placed on a rotating table which is in a magnetic field. The magnetic field is controlled by a power supply and is decreased with time.

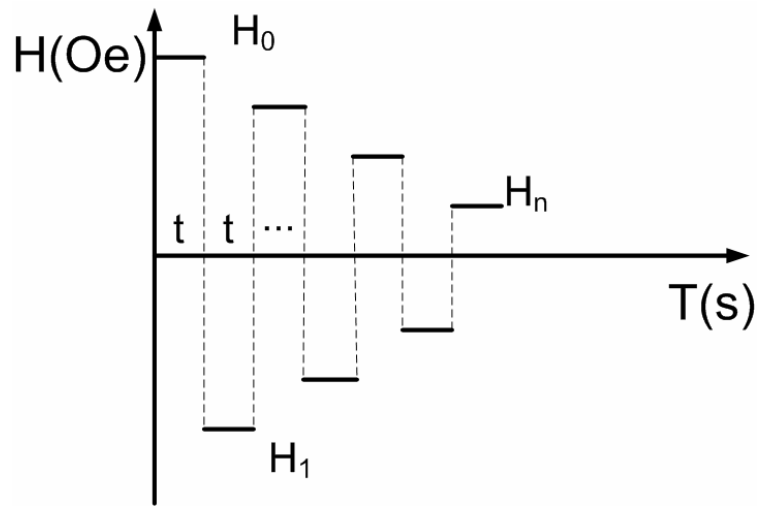


Figure 3.14 The field protocol used in demagnetization process.

Chapter 4 : Ground State Study

The artificial kagome lattice provides us a model system to study spin ice and frustration in general. It has the advantage that we can probe individual spins and study the ground state properties at room temperature. In this chapter, we discuss the ground state brought on by the demagnetization process. We confirm the ice rule in this system. Spin correlations were calculated and it is found that dipolar energy has enhancement effect to correlation. We also try to compare our system to real spin ice materials by charge correlation and entropy.

4.1 Direct observation of ice rule

In chapter 4, we introduced Lorentz TEM by which we deduce the in-plane magnetization direction for each spin element by their dark-edge bright-edge contrast. We also used an oscillating external field to drive the spin ice sample into an optimized near-ground state. Fig 4.1a shows part of a spin map of a demagnetized sample where we use arrows and colors to denote the spin directions. Consequently, neighboring elements with similar colors have a head-to-tail low-energy configuration, while those with dissimilar colors have a head-to-head or tail-to-tail high-energy configuration. A first glance reveals that the spins are quite disordered in long range, a signature of most frustrated systems.

For statistical studies of the spin distributions, we count the elements using a numerical method, labeling spins pointing to one of the two Ising directions as $s_i = 1$, and the opposite directions as $s_i = -1$. The net magnetization is then defined as

$m = \langle s_i \rangle$ for each of the three sub-lattices of spins. The demagnetization process typically achieves $|m|$ in the range of 0.03-0.14 for each sub-lattice. The distribution of vertex types is plotted in Fig 4.1b and varies among the six ice-rule vertex types from 9.8% to 24.8% [53]. We find that all vertices fall into the six low-energy configurations and there are no 3-in or 3-out high-energy states. Therefore, every vertex satisfies the ice rule.

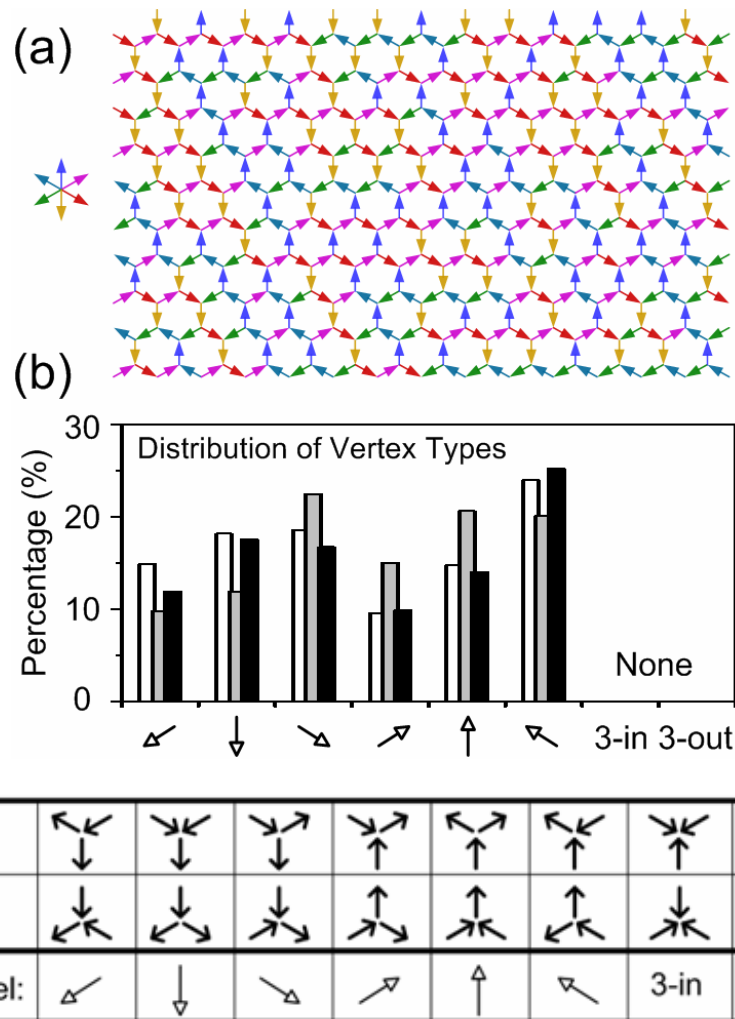


Figure 4.1 Spin vertex distribution in demagnetized kagome lattice. (a) A region of the spin map from a demagnetized kagome lattice sample. The spin directions are disordered in long-range, with a small net magnetization, yet locally there are some ordered chains and loops. (b) The vertex-type distributions; three demagnetization runs are shown with differently shaded bars. The bar labels are shown in the bottom table. The percentage of each type of vertex varies from run to run and ranges from 9.8%-24%.

4.2 Fourier transform of Lorentz TEM images

In pyrochlore spin ice studies, researchers use neutron diffraction to examine the disordered states and correlations [19, 23, 54]. Like x-ray and electron diffraction, neutron diffraction requires that the lattice period or obstacle size is smaller than the wavelength of the beam. This is obviously not true for our artificial kagome lattice and the electron wavelength. However, diffraction can be seen as the Fourier transform of the exiting wave from the studied lattice. Here we first acquire the real lattice images with Lorentz contrast, and then perform Fourier translation on computer. The resulting Fast Fourier Transform (FFT) images enable us to study the magnetic ordering of our system.

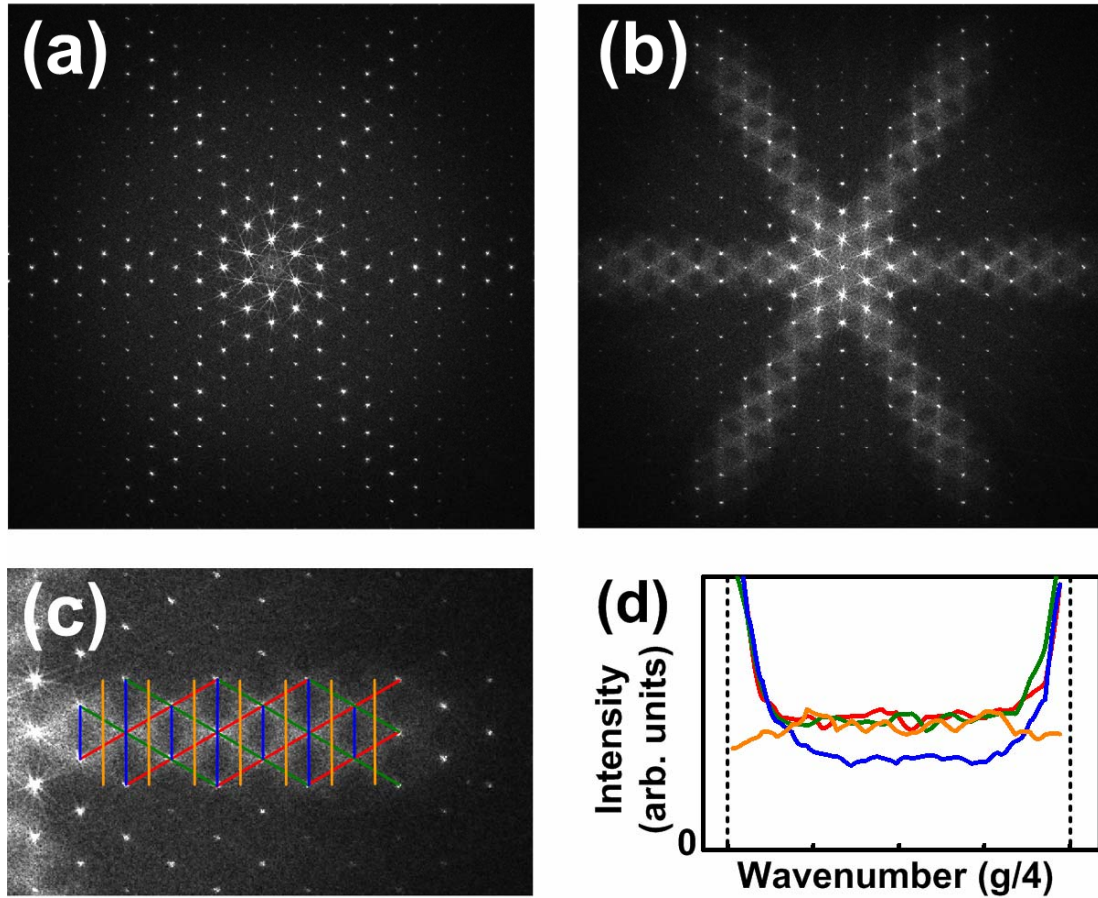


Figure 4.2 Fourier transforms of Lorentz images of the artificial kagome spin ice (six-fold average). (a) Fourier transform of a magnetic ordered state, (b) Fourier transform of a demagnetized state, (c) Zoom in picture of one arm of (b); (d) Line scans along the lines in (c).

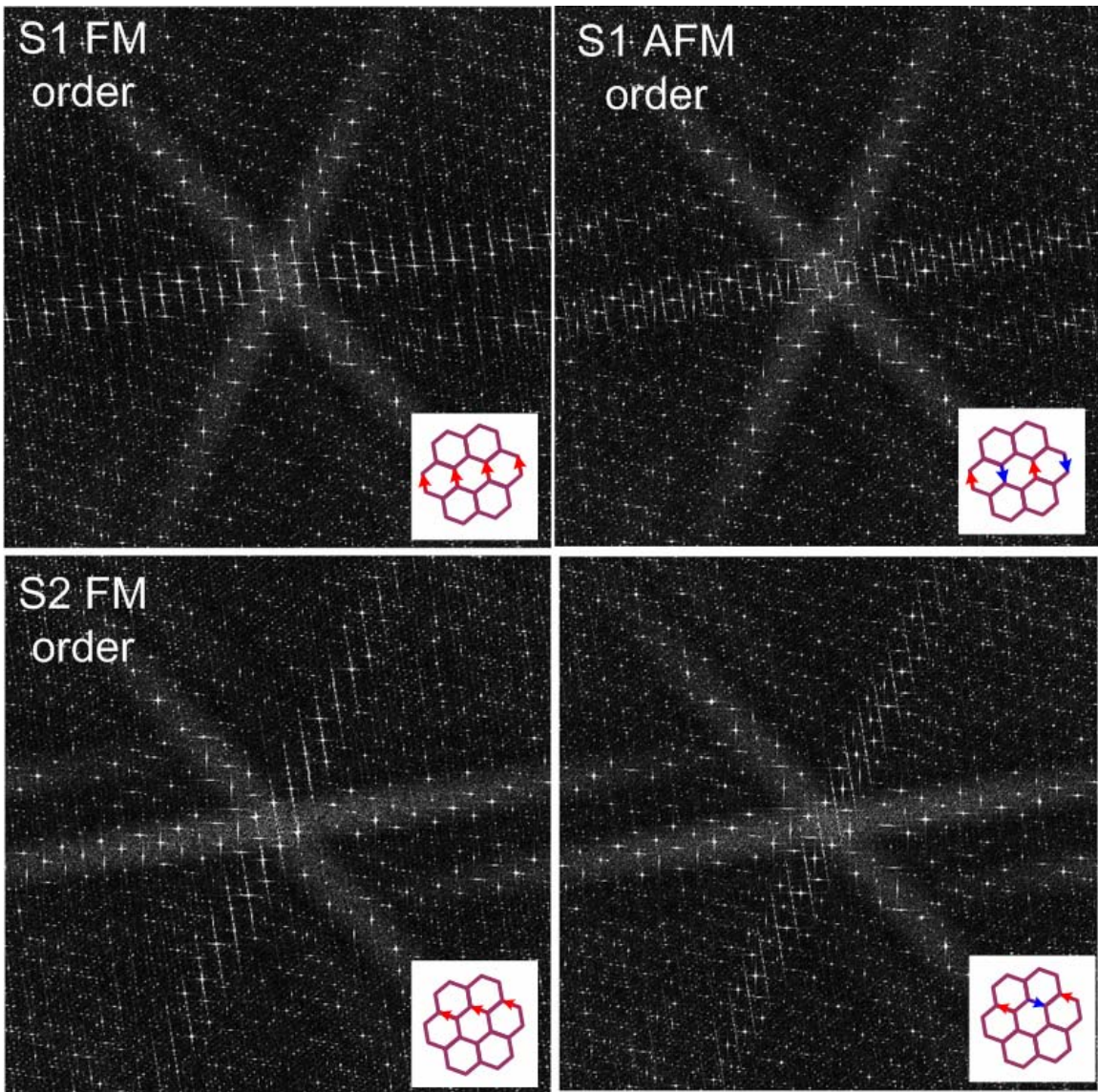
Fourier transform is taken on the Lorentz-mode image of the demagnetized sample and compared with that for a magnetic ordered sample. Fig 4.2a shows the Fast Fourier Transform (FFT) for the ordered sample (six-fold average), which features high contrast bright diffraction spots. However, the FFT shown in Fig 4.2b for the demagnetized sample is clearly different. In addition to the diffraction spots, there is a patterned streak shape of diffuse intensity between the spots. The six diffuse arms are related to different sub-lattices and suggest various degrees of disorder. Analysis on a zoom-in picture of one arm (Fig 4.2c and d) shows that there

are relatively strong intensities along the green and red lines which suggest ferromagnetic (FM) correlations between $\alpha\upsilon$ type spins or spins along a zigzag chain, The intensity along yellow lines suggest anti-ferromagnetic (AFM) correlations between $\alpha\delta$ type spins or spins perpendicular to their Ising direction (between the zigzag chains). Intensity along blue lines would suggest FM kind correlations between $\alpha\delta$ type spins. The observed low intensity indicates lack of this FM correlation.

To further verify the relation between spin correlations and the relative intensity in the Fourier transform, we also did simulations using a fake spin lattice. Fig 4.3 shows the results. In the simulation, we use 1 and -1 to indicate spins in the opposite directions. When we define a sub-lattice group of spins to be ordered, we leave the other spins to be random. A general conclusion from the simulation is that FM-type ordering generates periodic intensity lines passing *through* the diffraction spots, while AFM-type ordering shows periodical intensity lines *between* diffraction spots.

For example, in the FFT image for FM ordering in S1 sub-lattice (shown in Fig 4.3 insets), there are intensity lines passing through the diffraction spots in the arm which is perpendicular to S1, while AFM ordering in S1 generate similar periodic intensity lines but passing *between* diffraction spots. Following the same principle, if FM ordering happens along S2 (shown in insets), the periodic intensity lines still pass through the diffraction spots, while AFM ordering generates intensity lines passing *between* the diffraction spots. Note that when ordering happens in the S2 sub-lattice, the intensity now appears in another arm which is perpendicular to the

spin directions. However, the intensity lines are perpendicular to the ordering direction. So the angle between intensity lines and the arm that shows intensity is different.



40

Figure 4.3 FFT simulations from a computer generated fake spin ice lattice. The insets of each picture denote one ordered (FM or AFM) sub-lattice corresponding to that FFT image. The other two sub-lattices were left completely disordered by populating them with random spins.

4.3 Correlations

FFT analysis is qualitative, it usually requires detailed simulations, and it is limited in terms of detailed spin configurations. For that purpose, real space images and calculations based on them are far superior, demonstrating one of the strengths of the artificial meta-material approach. Fig 4.1a shows a spin map of part of the kagome lattice after the demagnetization process, where we utilize a color wheel to represent different spin directions. Spin disorder in long range and small net magnetization are visualized in this image, which is a signature found in most frustrated systems in their ground state[7]. Thus, we have an ideal system for calculating the intrinsic correlations defined by lattice geometry and magnetic interactions. Based on the fact that we observe many vertex types and the specific configuration varies from run to run, the correlation calculated would be expected to be close to its intrinsic value according to statistical theory.

Correlation between spin pairs is defined as $c_{ij} = 1$ when $\vec{s}_i \cdot \vec{s}_j$ is positive, otherwise $c_{ij} = -1$. There are also different types of correlations for a pair based on their relative position and how many elements are between them, as shown in Fig 4.4. The correlation coefficient is calculated as the average for each type of such neighboring pairs, e.g., $C_{\alpha\beta} = \langle c_{ij} \rangle_{(ij \in \alpha\beta)}$. A positive sign of $C_{\alpha\beta}$ indicates FM-type correlation, while negative sign indicates AFM-type correlation.

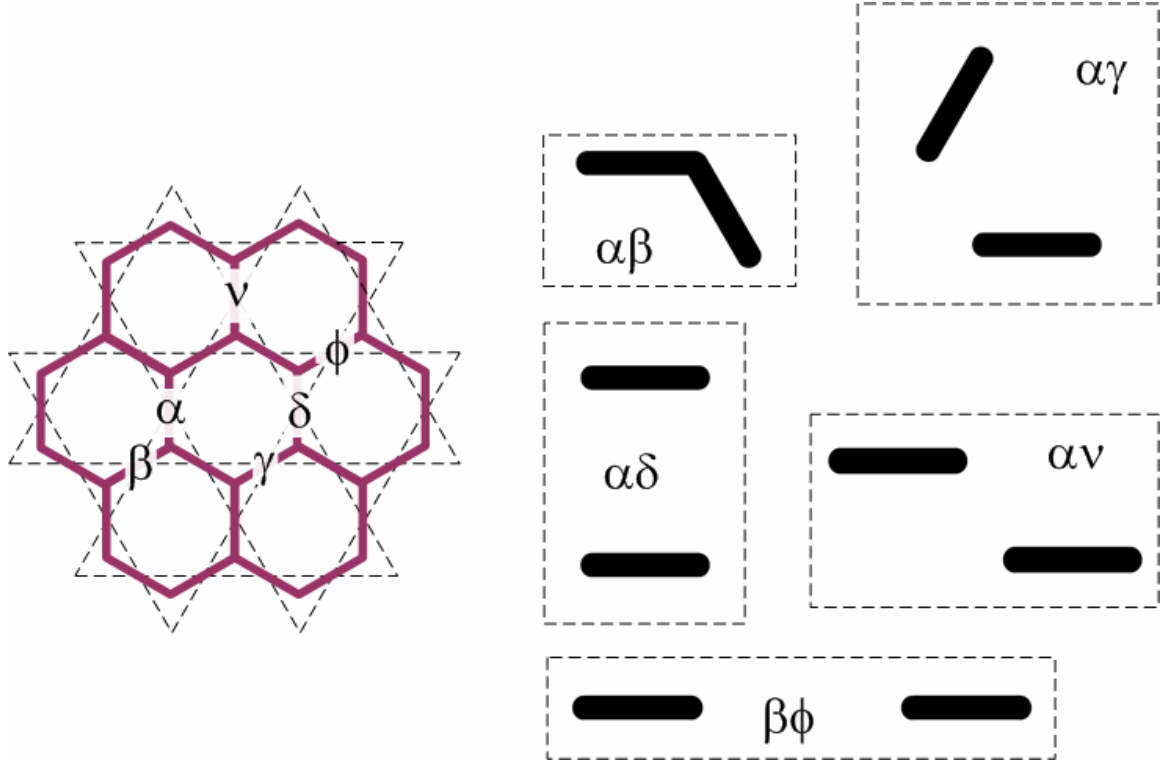


Figure 4.4 Illustration of different types of spin pairs.

The correlation coefficients are summarized in table III and are compared with Monte Carlo simulation results based on a kagome spin ice model using nearest-neighbor interactions [12]. We note substantial consistency between our results and the model simulation. Specifically, $C_{\alpha\beta} = 1/3$ indicates that all vertices obey the ice rule. The coefficient for second-nearest-neighbors within the same hexagon, $C_{\alpha\gamma} = -0.158$, indicates anti-ferromagnetic interactions, while second-nearest-neighbor coefficient in the neighboring hexagon is ferromagnetic with $C_{\alpha\nu} = 0.165$. Parallel elements within a hexagon have anti-ferromagnetic interactions with $C_{\alpha\delta} = -0.130$. The correlation value is also reflected in the spin map. For

example, the positive value $C_{\alpha\nu} = 0.165$ supports a slight ordering preference along the zigzag chain. While the negative value $C_{\alpha\gamma} = -0.158$ means two neighboring zigzag chains slightly prefer anti-parallel configuration.

Each of these pair-wise correlations agrees in sign and relative magnitude with published Monte Carlo simulations[12]. However, we note our measured higher-order correlations have reproducibly larger absolute values than predicted by Monte Carlo with only nearest-neighbor interactions. One difference between our model system and Wills' simulation is that their simulation uses a nearest-neighbor model only and did not include dipolar energy. To further investigate the dipolar effect in our system, we calculated the relative further-neighbor dipole energies using simple magnetostatics for each configuration.

Table III Correlation coefficients of artificial kagome spin ice calculated from a demagnetized sample. The results are shown as the mean and standard deviation correlation values taken from three demagnetization runs. ΔE_{dipole} gives the energy difference between aligned and anti-aligned spin pairs, relative to the nearest neighbor value.

	Data	Model	ΔE_{dipole}
$C_{\alpha\beta}$	0.333	0.333	1.0
$C_{\alpha\gamma}$	-0.158 ± 0.008	-0.118	-0.137
$C_{\alpha\nu}$	0.165 ± 0.013	0.101	0.089
$C_{\alpha\delta}$	-0.130 ± 0.015	-0.072	-0.070
$C_{\beta\phi}$	0.057 ± 0.007	0.007	0.082

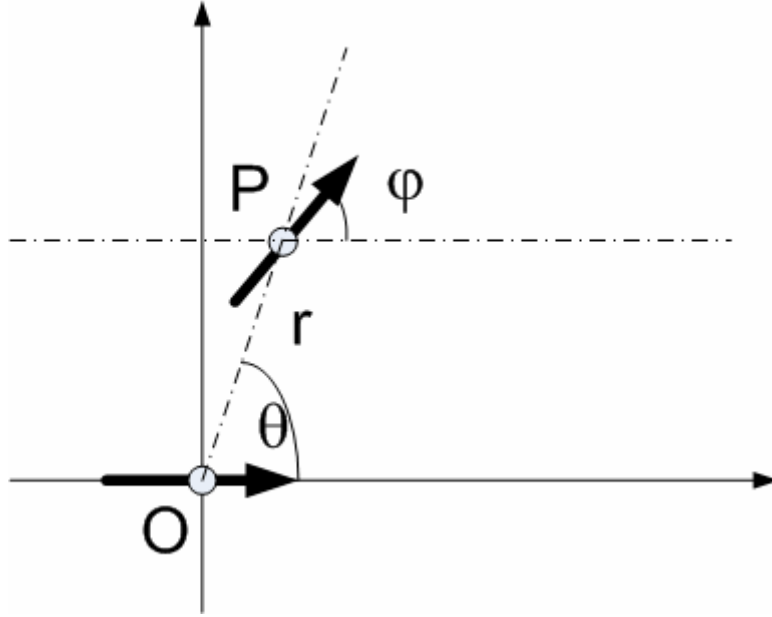


Figure 4.5 Illustration of two dipole interaction in x-y coordinates. Dipole P sits in a magnetic field generated by dipole O and has a magnetic potential energy determined by their relative positions.

In the following calculation, we assume each spin element is a point dipole.

The dipolar interaction energy in Table III is given by the concept of magnetic potential energy.

$$U = -\vec{m}_1 \cdot \mathbf{B},$$

where m_1 is the moment of dipole P, and B is the magnetic field at position P induced by another dipole O.

The field from a point dipole O is given by

$$\mathbf{B}(r) = \frac{\mu_0}{4\pi r^3} (3(\vec{m} \cdot \vec{r})\vec{r} - \vec{m})$$

So the magnetic field components along x and y axis are

$$B_x = \frac{\mu_0 m}{4\pi} \left[\frac{3 \cos^2 \theta - 1}{r^3} \right]$$

$$B_y = \frac{\mu_0 m}{4\pi} \left[\frac{3 \cos \theta \sin \theta}{r^3} \right]$$

Thus, the magnetic potential energy is given as:

$$U = B_x m_1 \cos \varphi + B_y m_1 \sin \varphi = \frac{\mu_0 m m_1}{4\pi} \left[\frac{3 \cos^2 \theta - 1}{r^3} \right] \cos \varphi + \frac{\mu_0 m m_1}{4\pi} \left[\frac{3 \cos \theta \sin \theta}{r^3} \right] \sin \varphi$$

Since all elements have the same length and width, m_1 and m have the same magnitude, and the magnetic potential energy between different types of spin pairs can be calculated as shown in the table. The sign of potential energy is inverted when one spin is in the opposite direction. Note that the sign from our definition of the potential energy (positive for FM type spin pairs and negative for AFM type spin pairs) is consistent with our correlation definition where we define $c > 0$ when $\vec{s}_i \cdot \vec{s}_j$ is positive.

The dipolar energy values we calculate agree in sign with the correlation values. This suggests that dipolar interactions are responsible for the deviations, as is the case for real spin ice [7]. These long-range interactions generally increase the ordering in spin ice, decreasing the degeneracy of the ground state manifold [55, 56].

4.4 charge correlation

In pyrochlore spin ices like $\text{Dy}_2\text{Ti}_2\text{O}_7$, applying magnetic fields to the sample partly or fully lifts the macroscopic degeneracy of the ground state depending on the field direction and magnitude [17, 21]. For a field parallel to the [111] direction, along which the pyrochlore lattice can be envisioned as alternating stacking of kagome and triangular layers (see Fig 3.5 and 4.6a), the field with intermediate strengths partly lifts the degeneracy and simultaneously induces decoupling of spins

between the layers. In these ground states, spins on the triangular layers are parallel to the field, and spins on the kagome layers retain macroscopic degeneracy preserving the “two-in and two-out” configuration at each tetrahedron (see Fig 4.6b and [34]). This state is called the Kagome plateau.

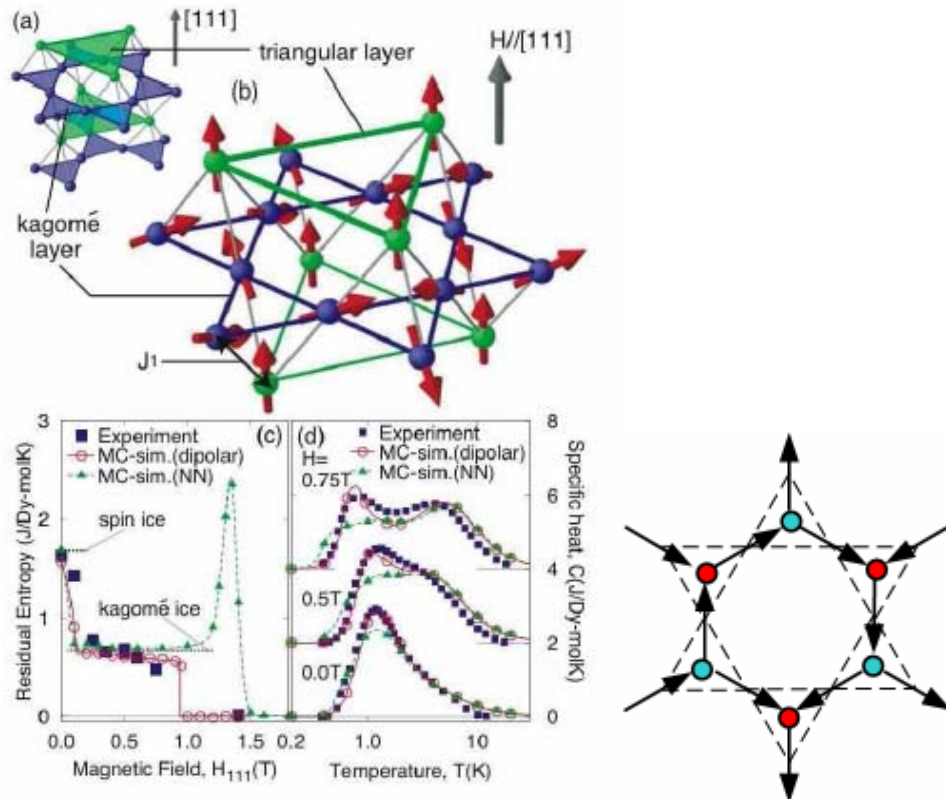


Figure 4.6 Kagome plateau in pyrochlore spin ice and its magnetic charge distribution. (a) The pyrochlore lattice is alternating stacking of kagome and triangular layers along the [111] direction. (b) A spin configuration of the kagome ice state is shown; the spin configuration of the kagome layer (blue) is illustrated in the right picture for a clearer view. (c) The observed [57] and calculated residual entropies [58] are plotted as a function of magnetic field. (d) Temperature dependence of observed [57] and calculated specific heat at $H = 0, 0.5, 0.75$ T. Reproduced from [34]. Right figure: Magnetic charge representation of the spin configurations in the kagome layer.

The kagome layer at this plateau presents very interesting spin configurations.

First, each triangle in the layer has 2-in 1-out or 1-in 2-out state which means they

obey ice rule. Second, if we use red color to denote 2-in-1-out triangles and blue color for 1-in 2-out triangles, every nearest neighboring triangle always has a different color. Although the spins in this state are still disordered, the second restriction reduce the entropy from 0.501[59] to 0.081 [57] compared to a free kagome spin ice. On the other hand, the former can be seen as a minimum-energy or true ground state for kagome spin ice with ice rule restriction. To investigate to what extent the demagnetization process put our sample in the true ground state, we introduce a concept called magnetic charge [60].

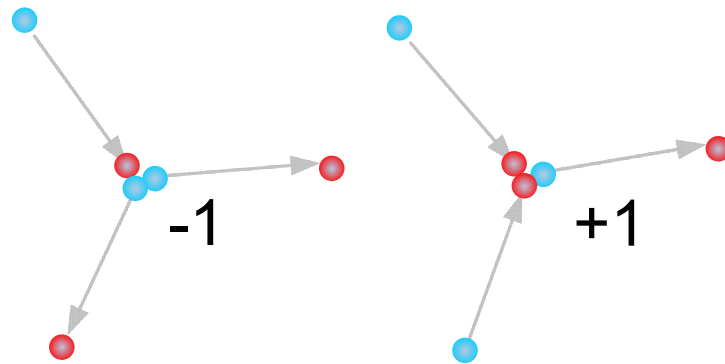


Figure 4.7 Mapping from dipoles to dumbbells. The dumbbell picture is obtained by replacing each spin (grey color arrows) by a pair of opposite magnetic charges (red and blue ball).

The Hamiltonian for spin ice contains a sum of nearest neighbor exchange and long range dipolar interaction. We replace the interaction energy of the magnetic dipoles with the interaction energy of dumbbells consisting of equal and opposite magnetic charges that live at the end of the bonds. The two ways of assigning charges on each bond reproduces the two orientations of the original dipole. It is

found that a charge value at $\pm\mu/a_d$, a configuration this way would reproduce the dipole moment of the spin.

The energy of a configuration of dipoles is computed as the pair wise interaction energy of magnetic charges, given by the magnetic Coulomb's law[60, 61]:

$$V_{\alpha\beta} = \begin{cases} \frac{\mu_0}{4\pi} \frac{Q_i Q_j}{r_{ij}} & |i \neq j \\ \frac{1}{2C} Q_i^2 & |i = j \end{cases}$$

where Q_i denotes the total magnetic charge at site α , and r_{ij} is the distance between two sites. $C \propto \frac{a}{u_0}$, a = distance between charges in a junction. The energy

vanishes with distance at least as fast as $1/r^5$ [60]. The total dipolar energy is:

$$H = \sum_i \frac{q_i^2}{2C} + \frac{\mu_0}{4\pi} \sum_{i,j} \frac{q_i q_j}{r_{ij}}.$$

For small a , first term is minimum for the total magnetic charge in a junction is smallest. So the ice rule translates into charges in junctions restricted to +1 and -1. We use red and blue circle to denote positive and negative magnetic net charge respectively. Because energy in the above equation vanishes with distance very fast, it's reasonable to only consider nearest neighboring sites to estimate. We found a charge ordering state with alternating red and blue circles is the minimum energy state or true ground state (Fig 4.8c), which is exactly the kagome layer spin configuration in pyrochlore spin ice at kagome plateau happens (Fig 4.6 right picture).

If we define charge correlation as,

$$C_{\alpha\beta} = \langle c_{\alpha\beta} \rangle = \langle Q_{\alpha} Q_{\beta} \rangle, \text{ where } Q_{\alpha}, Q_{\beta} = \pm 1$$

In the charge ordering state, the charge correlation between neighboring sites is $C_{NN} = -1$, because every nearest neighbor magnetic charge pair has opposite signs.

Our demagnetization process didn't put the sample in a fully ground state.

The correlation we calculated $C_{nn} = -0.3079$, or 1.96 out of 3 neighboring sites have opposite signs. The nearest-neighbor value is certainly more negative than expected from a spin-ice ensemble, which is $-1/9 = -0.111$ based on the Bethe-lattice approximation (using similar analytical method introduced by [62] and [12]). The significant deviation for our data from $-1/9$ towards -1 indicates that the system tends to have charge order. The reason that our demagnetization process fails to reach the true ground state may be that such a ground state requires complex spin flipping, such as loop or chain flipping, while the artificial kagome spin ice prefers zigzag chain flipping in our observation (see chapter 6).

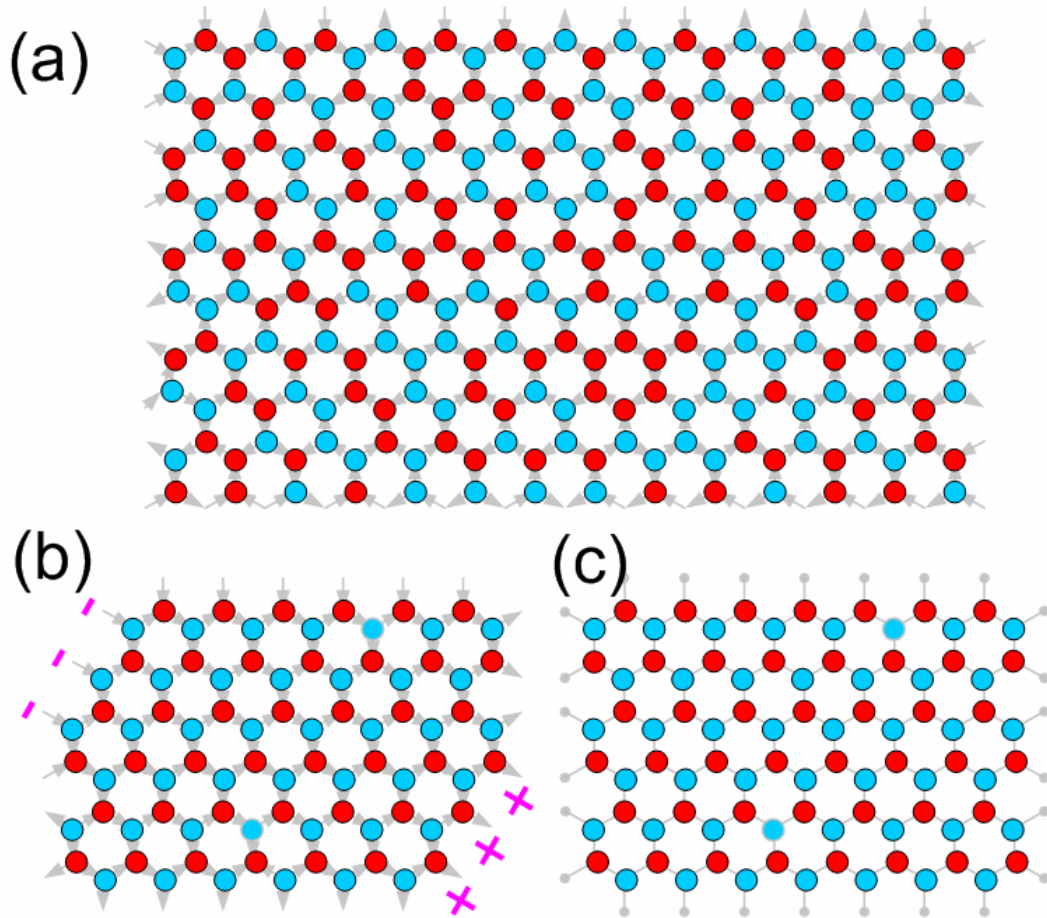


Figure 4.8 Magnetic charge maps. (a) Magnetic charge map for a demagnetized sample. (b) Charge map for a magnetic ordering state. $C_{NV} = -1$, but the magnetic ordering state has higher energy because there are significant net magnetic charges at the surface (denoted by plus and minus signs). (c) Magnetic charge ordering state with zero magnetization, which is thought to be the true ground state of kagome spin ice.

4.5 Ground state entropy

As we stated in chapter 2, the magnetic entropy change, ΔS , can be determined by measuring the specific heat and integrating $C(T)/T$ between two temperatures (Fig 2.5 and [17]):

$$\Delta S_{1,2} = \int_{T_1}^{T_2} \frac{C(T)}{T} dT.$$

We also learned that the equivalent temperature to change the magnetization status for artificial spin ice is about 10^4 K, which is above the melting temperature of permalloy. Thus we have to find an alternate method to calculate the entropy for artificial spin ice. For this, we utilize a statistic method: Shannon entropy.

Shannon entropy is a measure of the uncertainty associated with a probabilistic event or variable [63]. It has the form

$$H = -\sum_i^n p_i \log p_i .$$

For example, for a binary system, the possibilities of event 1 and 2 are p_1 and p_2 respectively, where $p_2 = 1 - p_1$. So Shannon entropy can be plotted to give Fig 4.9.

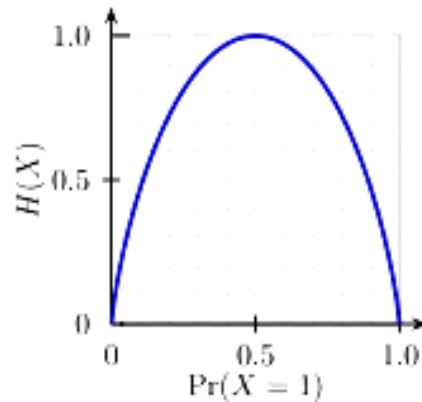


Figure 4.9 Shannon entropy for a binary system.

Shannon entropy is similar to the Gibbs entropy, defined as:

$$S = -k \sum_i^\infty p_i \ln p_i .$$

Jaynes [64] has discussed the relationship between Shannon and Gibbs entropy. He proposed that thermodynamics should be seen as an application of

Shannon's information theory, and the thermodynamic entropy can be interpreted as being an estimate of the amount of further Shannon information needed to define the detailed microscopic state of the system. The method Pauling used to estimate the entropy of spin ice [62] further suggests we can use a statistical method to calculate thermodynamic entropy.

Simply, an alphabet consisting several spins could have different types of configurations, the possibility of each type that appears on a demagnetized sample is denoted as p_i , where $\sum p_i = 1$. From this we can calculate the Shannon entropy, H . For example, if we choose a vertex, consisting three spins, as an alphabet, there are $n=6$ types of configuration, $i = 1 \dots 6$, as we have shown in Fig 4.1. The possibility of each type $p_i = 0.122, 0.158, 0.193, 0.115, 0.165, 0.231$ respectively (only ice rule configurations are allowed), and $H = -\sum_i^6 p_i \log p_i = 0.836$.

There are many different alphabets for choosing. For example, it could be one spin, thus $n=2$, two spins and $n=4$, three spins and $n=6$, five spins and $n=19 \dots$ (Fig 4.10)

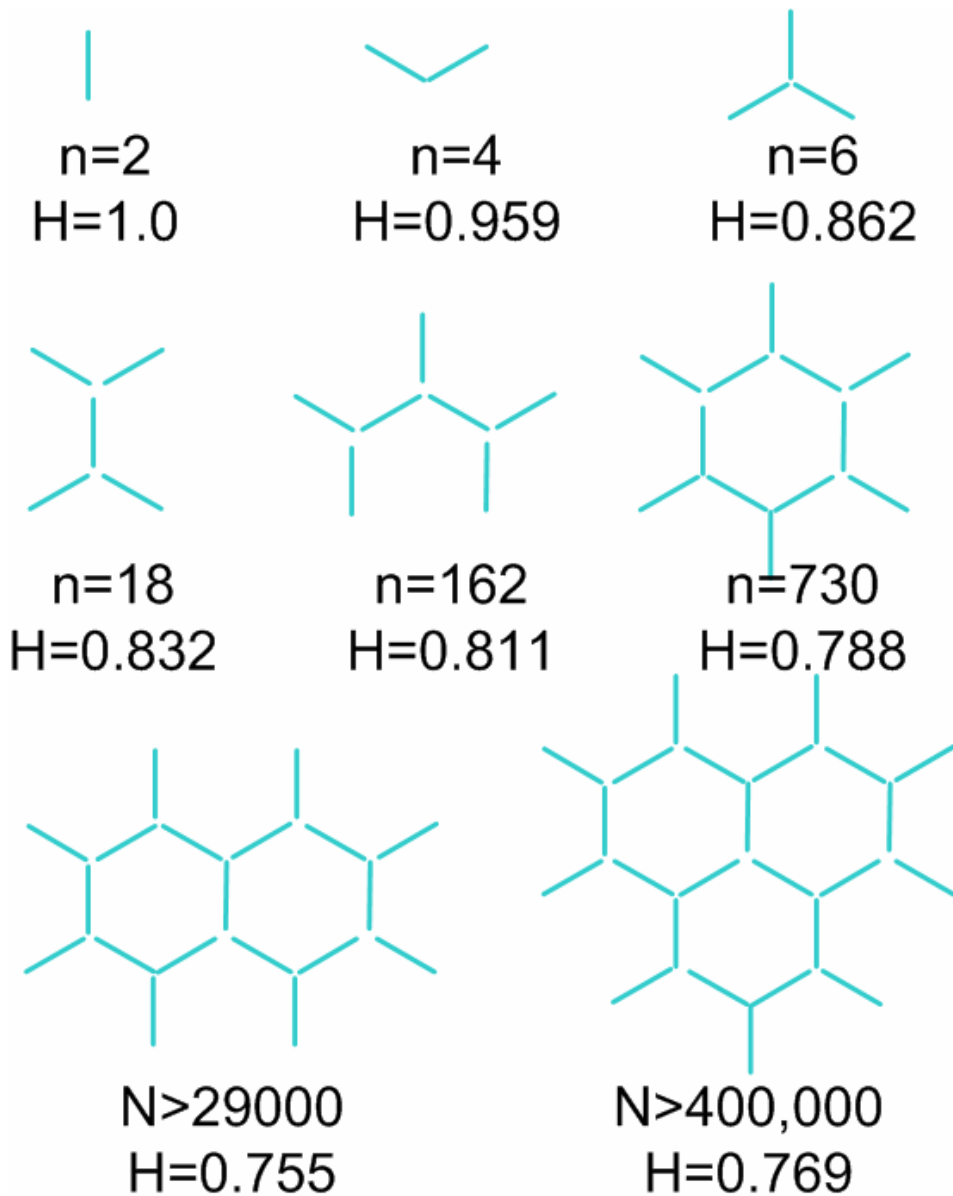


Figure 4.10 Shannon entropy based on different alphabets. Here, n is the number of allowed states, and H is calculated Shannon entropy. H is calculated on a kagome spin ice in its disordered state simulated by Monte Carlo method.

From Monte Carlo simulation, we find that when the chosen alphabet increases in size, the calculated Shannon entropy approaches 0.723 (using units of Shannon entropy, bits), as estimated by Kano *et al.*[59]. In principle, we can choose a very large alphabet and calculate a Shannon entropy based on the actual kagome spin ice sample. However, that requires a larger sample because the data set needs to approach ~ 1023 elements to make the Shannon entropy approach thermodynamics entropy [65].

Entropy for Kagome spin ice has been reported from 0.723 to 0.116 (using units of Shannon entropy, bits) depending on their constraints [59] [57]. As we have calculated above, $H = 0.836$ bits if we choose three spins as an alphabet. Although, this number is larger than even the 0.723 value given by Kano *et al.* [59](because the chosen alphabet is too small), it is smaller than the value 0.862 given by Monte Carlo simulation. This indicates the real entropy value is likely smaller than 0.723. Again, if the sample size is large enough and we choose a larger alphabet, we expect the calculated H to approach the real thermodynamic entropy. This work is ongoing in our group.

Chapter 5 : Magnetization Reversal and Symmetry-breaking

In addition to the ground state properties, it is desirable to study the disturbance of frustration due to external influences, such as magnetic field or pressure. In this chapter, we introduce some results on the kagome lattice during the magnetization reversal process. Although stress is difficult to introduce to our sample, we study the property change by introducing distortion, via strain, into the lattice.

5.1 magnetization reversal

Neutron scattering has shown that applying a magnetic field would lift the degeneracy of disordered spin ice and eventually lead to an ordered state[19]. Artificial spin ice enables us to study the magnetization process spin by spin. In our experiment, this is realized by applying a changing field in the TEM to the sample, while taking real-time video of the Lorentz images. The magnetization reversal process might also shine light on the demagnetization mechanism.

There are two special directions regarding the magnetic field relative to the kagome spin ice. One is along the zigzag chain, x_1 , and another along one spin, with a 60° angle to the other two spins, x_2 . When field is along x_1 direction (Fig 5.1), spin flipping was observed to be along the zigzag chains parallel to that direction, and it propagates over long distances. Spins in the third sub-lattice are found to remain unchanged, presumably because they are perpendicular to the field. Flipping that propagates along zigzag chain could be explained by the ice rule. If chain flipping stops in the middle of a chain, some vertices would probably violate the ice rule. In

principle, chain flipping could stop where a vertex does not violate the ice rule by switching only one spin. When field is along x_2 direction (Fig 5.2), all the spins would eventually flip. However, during this chain flipping is also preferred.

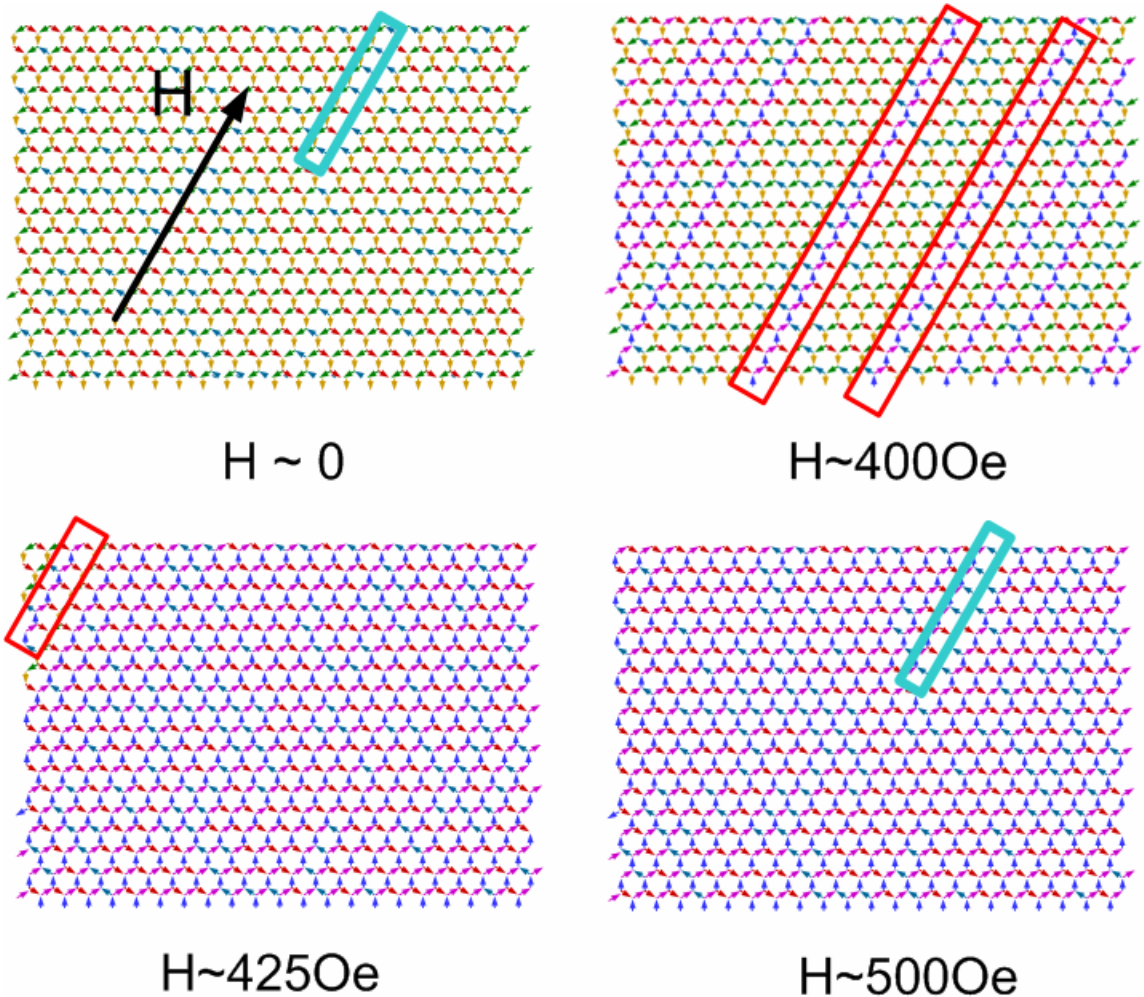


Figure 5.1 Magnetization process when field is along a zigzag chain. Arrow indicates the field direction after the sample is pre-magnetized in the opposite direction. Red color frames are examples of chain flipping. Blue color frames show spins that do not flip during the magnetization process.

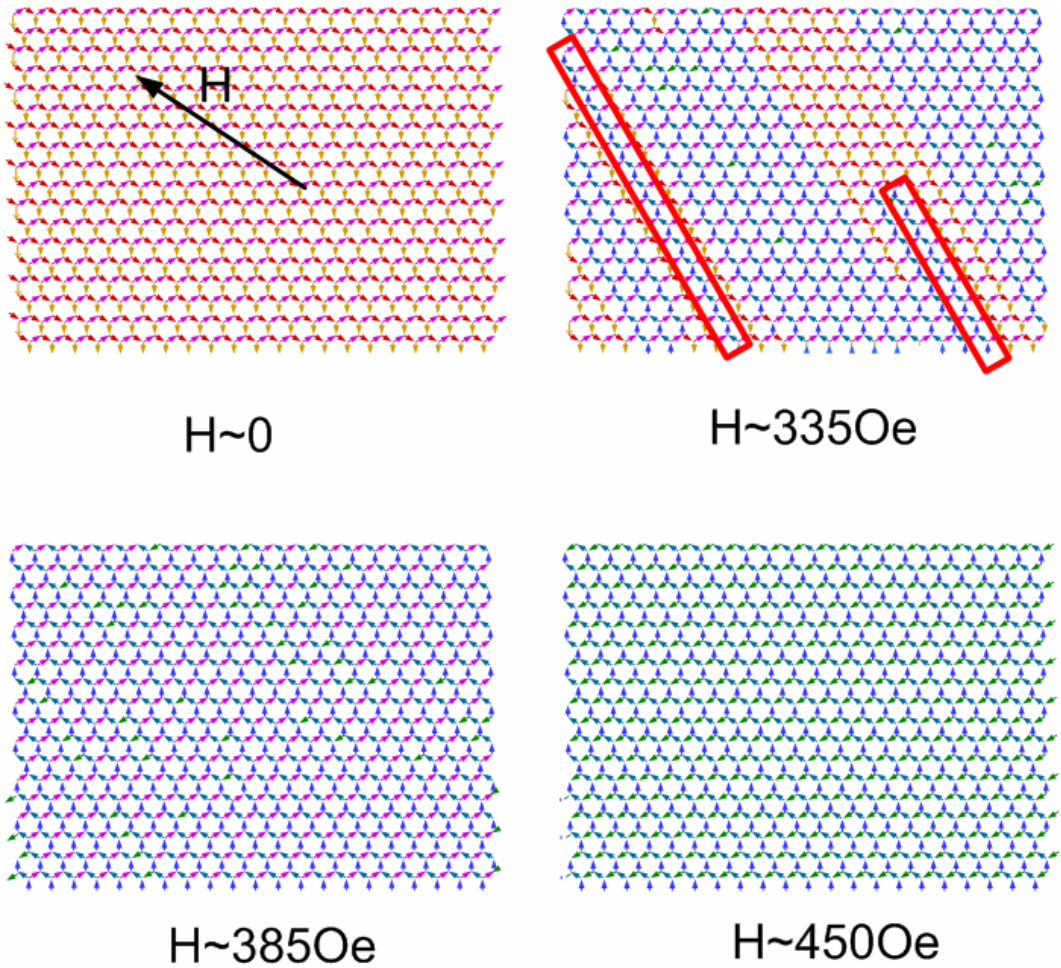


Figure 5.2 Magnetization process when field is along a spin and has 60° angle with the other two spin sub-lattice (Arrow). The sample was pre-magnetized in the opposite direction. Red color frames are examples of chain flipping.

Another point is that the magnetic field change is small from the start of magnetization switching to the finish, in other words the M-H curve has a very steep slope during the magnetization process. This avalanche-like reversal process has been confirmed by a numerical simulation using the magnetic charge model introduced in Chapter 5 [61].

5.2 distortion tuned frustration

In 3D spin ice materials, the stable spin configurations for each tetrahedron obey an ice rule, which states that two spins point outward and two spins inward on each tetrahedron. For each tetrahedron, there are six possible combinations of spins under the rule. The ground state is highly degenerate, and a static disordered state is formed at low temperature. These interesting phenomena originate in the high symmetry of the pyrochlore structure. So changing the structural symmetry could influence the frustration, because the interaction balance would be changed.

One approach to changing the structural symmetry is to apply a pressure. Mirebeau *et al.*[66, 67] studied the spin liquid $\text{Tb}_2\text{Ti}_2\text{O}_7$ by single crystal neutron scattering under high pressure up to 2.8GPa, together with a uniaxial stress, down to 0.1K. They found a long-range-ordered antiferromagnetic structure is induced by pressure. The Neel temperature and ordered magnetic moment can be tuned by the anisotropic pressure component. Mito[68] measured the magnetization curve of $\text{Dy}_2\text{Ti}_2\text{O}_7$ spin ice at $T=1.7\text{K}$ under uniaxial pressure along $\langle 111 \rangle$ direction up to 13.0 kBar. The measured enhancement of initial susceptibility when pressure is along $\langle 111 \rangle$ crystal orientation suggests a change of the degeneracy in the ground state.

It is also possible to introduce lattice and symmetric adjustment by doping. For example, Lau *et al.*[69] studied the zero-point entropy of Ho stuffed $\text{Ho}_{(2+x)}\text{Ti}_{(2-x)}\text{O}_7$ materials and found the zero point entropy per spin measured appears unchanged by excess spins, although doping certainly changes the lattice parameters and magnetic interaction. The problem here is that the geometrical effect can not be isolated from other factors.

Artificial spin ice is a new approach for the study of spin ice as individual spins can be directly observed. In the previous realization of a two dimensional kagome spin ice (see Fig 3.6), we demonstrated for the first time the rigid adherence to a local ice rule by directly counting the individual pseudo-spins (Fig 4.1). The resulting spin configurations show not only local ice rules and long-range disorder, but also correlations consistent with spin ice Monte Carlo calculations. Our study suggests that dipolar corrections are significant in this system, as in real spin ice (Table III). Artificial spin ice also allows us to intentionally change the symmetry of the pattern, and thus to study the symmetry breaking problem systematically.

Here we introduced a strain-like distortion to the kagome lattice. Strain can be classified into linear strain and shear strain in two dimensions.

$$\varepsilon_{ij} = \begin{bmatrix} \varepsilon_x & \gamma_{xy}/2 \\ \gamma_{xy}/2 & \varepsilon_y \end{bmatrix},$$

where $\varepsilon_x, \varepsilon_y$ are linear strain tensors and γ_{xy} is shear strain tensor. The experiment we did is to distort the lattice in one direction by various amounts while keeping the other direction unchanged, i.e. $\varepsilon_y = 0, \gamma_{xy} = 0$, while ε_x is a variable defined below. As shown in Fig 5.3, we define a parameter $s = b'/b$ to characterize the strain, where $\varepsilon_x = s - 1$. In our experiments, we vary s from 0.8-1.5.

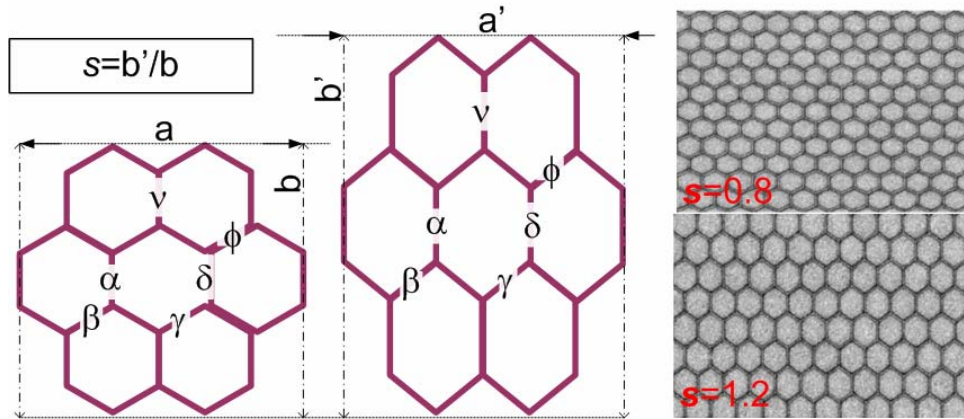


Figure 5.3 Sketch of the proposed kagome spin ice with strain-like distortion. The uniaxial ‘strain’ is defined $s = b'/b$, while $a' = a$. We varied s from 0.8 to 1.5 in the patterned samples and ‘strain’ $\varepsilon_x = s - 1$. The lattices pictured on the right have $s = 0.8$ and $s = 1.2$ respectively.

We first studied the vertex-type distribution change due to the lattice distortion. As shown in Fig 5.4, among the 6 types of vertices, the percentage of 90° vertices and -90° one increases as strain increases or when the lattices is stretched, and they become less as the lattice is compressed. The percentage of other types of vertices becomes less as s increases. We notice that ice rule is still valid as s changes in this range.

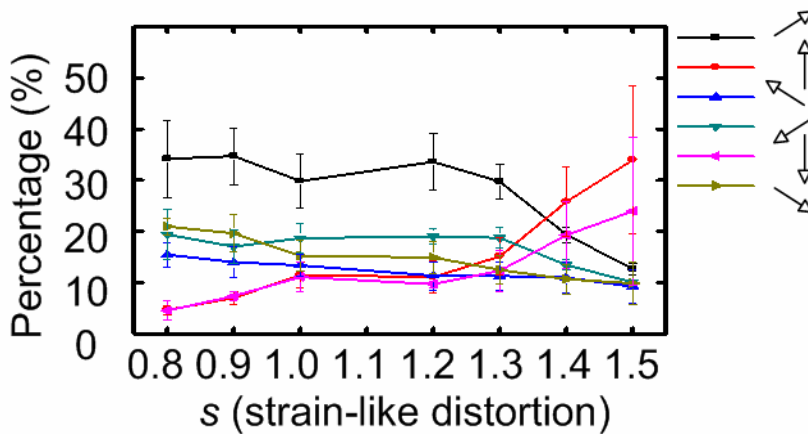


Figure 5.4 Vertex type distribution with lattice distortion. The ‘strain’ s is in vertical direction (90°). The numbers of vertices in the vertical direction (90° ones and -90° ones) follow s change.

The above preference of vertices configuration due to strain can be explained by the interaction imbalance due to symmetry breaking. Our OOMMF simulation suggests both exchange energy and dipolar energy changes with distortion. For example, when ‘strain’ value is larger than 1.0, the angles between neighboring spins along the 60° and -60° zigzag chains ($(180^\circ - \alpha/2)$ in Fig 5.5) become larger than 120° ; thus, a continuous magnetization along those chains cost less exchange energy, while a magnetization along the horizontal zigzag chain for angles less than 120° (α in Fig 5.5) cost more energy. The dipolar energy also plays as consistent a role as the exchange energy, as shown in Fig 5.6.

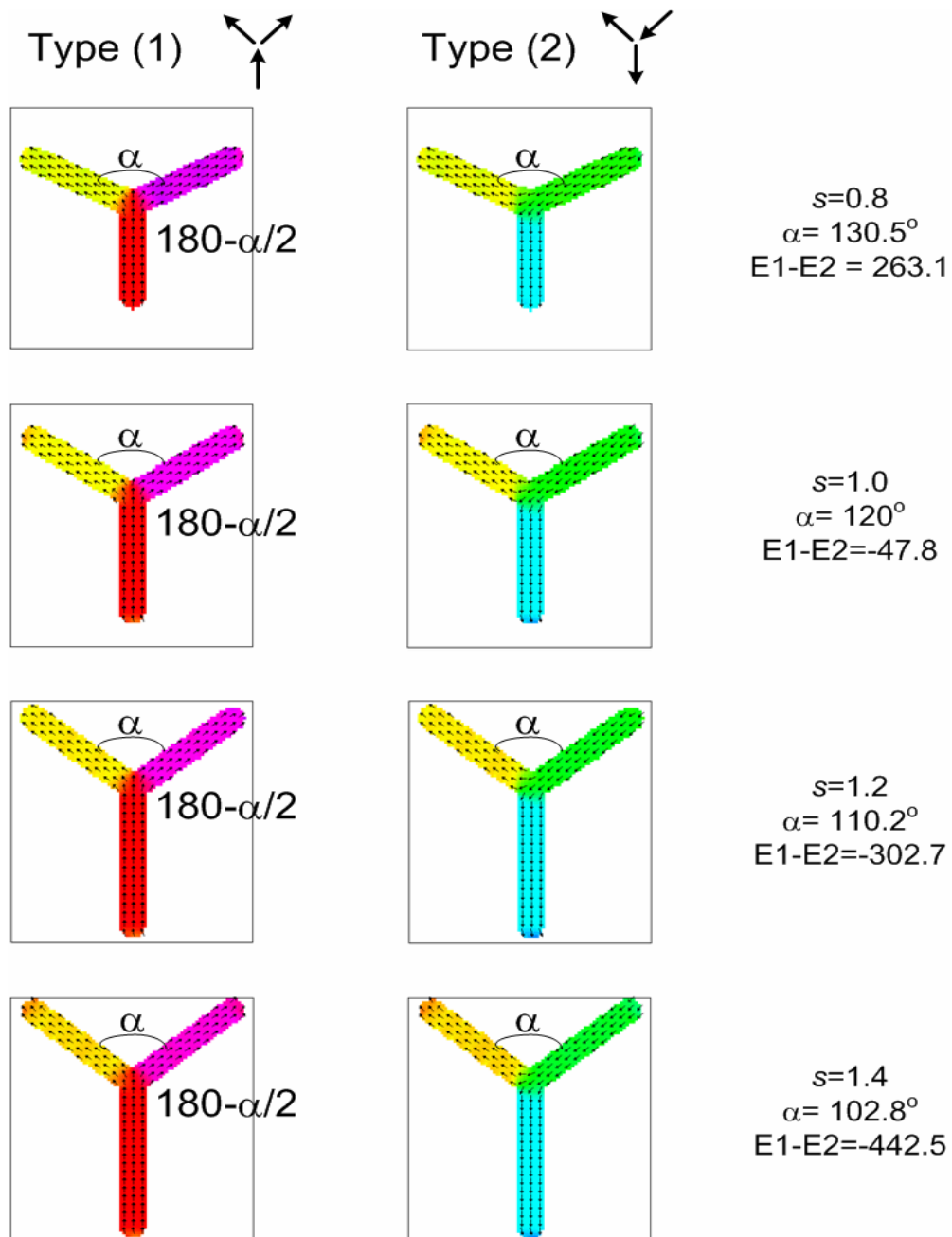


Figure 5.5 OOMMF simulation of a three-spin vertex with various distortions. The four images on the left (1) are configuration when overall magnetization is along the 'strain' (vertical),

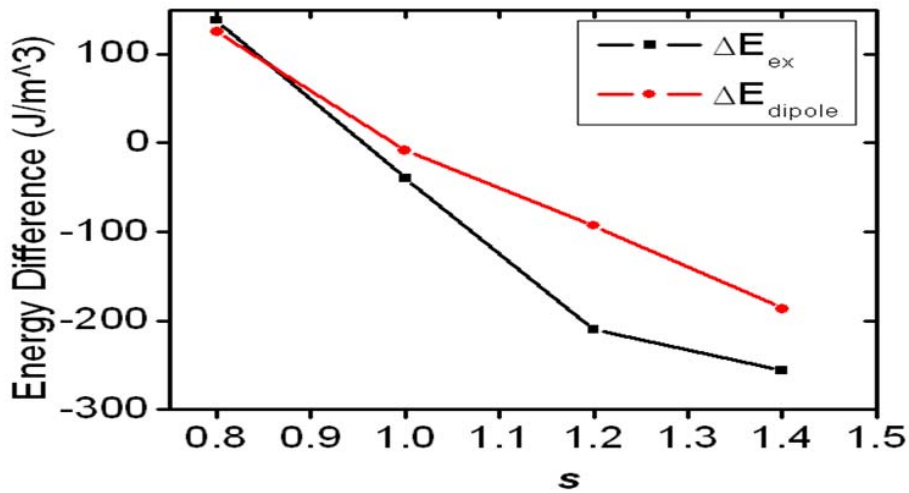


Figure 5.6 Energy change of triangular vertex with 'strain' distortion. $\Delta E = E(1) - E(2)$. When ΔE negative, magnetization configuration (1) in Fig 5.5 is favorable, and $90^\circ / -90^\circ$ vertices are preferred.

We also study the correlation change. Since the lattice is no longer symmetric with $s \neq 1$, we calculated the correlations from the data for spin elements in 3 directions separately (as defined in Fig 5.7), i.e. the vertical spins (red), the 150° spins (blue) and 30° (green) spins (although the latter two are not along 150° or 30° when $s \neq 1$).

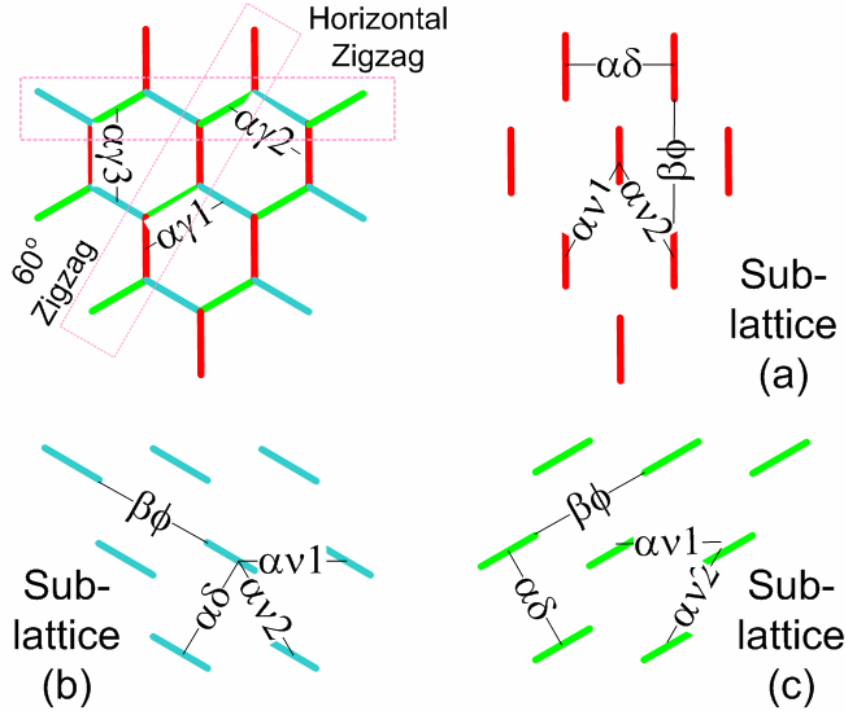


Figure 5.7 Correlation symbols definition for three sub-lattices.

As we have mentioned above, the magnetization favors the 60° and -60° zigzag chain as s increases. This trend is presented by the αv type correlations. αv_1 , αv_2 for the vertical (red) spins, as well as αv_2 for the 150° and 30° (blue and green) spin elements all increase with s . αv_1 for the 150° and 30° spin elements decreases with s , indicating the spins along the horizontal zigzag chain become less correlated as the lattice is stretched in the vertical direction.

$\alpha\delta$ and $\beta\phi$ for the vertical spin elements also increase with s . This can be explained by an increase in the dipolar energy. Since the lattice is stretched in the vertical direction, the spin elements in the vertical direction become longer compared with other two. $\alpha\delta$ and $\alpha\phi$ for the spins in 150° and 30° direction remain almost unchanged. The elements in these directions are also stretched in length; however,

they also become further spaced. Fig 5.8b also shows the $\alpha\gamma$ correlation change.

Here $\alpha\gamma_1$ and $\alpha\gamma_2$ indicates correlations between one vertical spin and one 150° and 30° spin, and $\alpha\gamma_3$ is between one 150° spin and a 30° spin. The trend is less obvious for $\alpha\gamma$ correlations, although $\alpha\gamma_3$ suggests more AFM type correlation because the angle between this spin pair become more parallel with more strain.

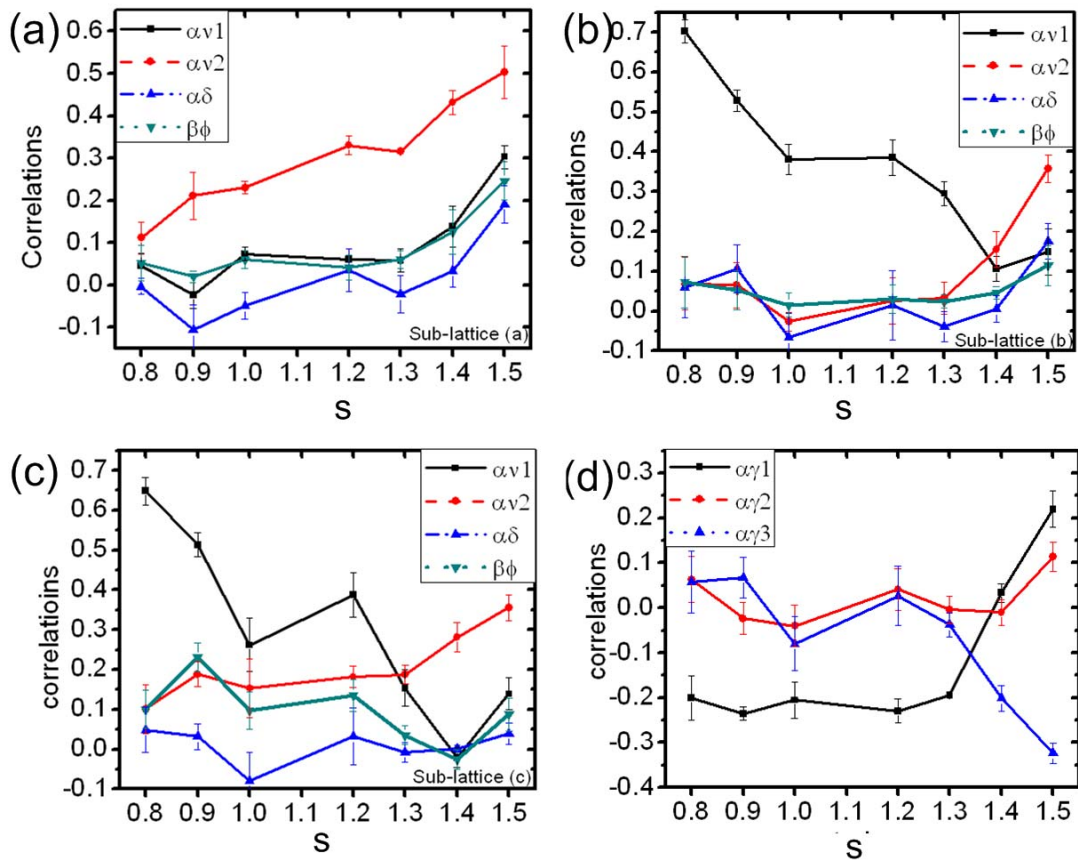


Figure 5.8 Correlations vs. strain-like distortion measurements. Refer to Fig 5.7 for the definition of Greek symbols. a) Correlations for vertical spins. b) $\alpha\gamma$ correlations. c) Correlations for the -150° spins. d) Correlations for the 150° spins.

5.3 lithography stigmatism and crystal anisotropy

Intentionally introduced artificial distortion certainly breaks symmetry of the local and global magnetization in kagome spin ice as we discussed above. However in the sample without distortion, symmetry breaking remains, revealed by the unequal distribution of the 6 vertex types (Fig 5.1). This symmetry breaking seems consistent from different demagnetization runs, indicating the demagnetization is not fully effective in this sample. For example, the 150° type vertices have a higher percentage relative to other vertex types in three runs. The symmetry breaking is thought to be due to either the lithography (lattice distortion or stigmatism during writing) or film deposition (crystal anisotropy). Although, it seems unlikely that lattice distortion alone can account for this. We can measure (by TEM) the unstrained lattice to have $<3\%$ inadvertent ‘strain’, but still 30% intentional ‘strain’ does not overcome the symmetry breaking. This suggests that either astigmatism or film structure play a primary role.

To investigate whether the demagnetization ineffectiveness (remnant magnetization) comes from crystal anisotropy or lithography stigmatism induced lattice defects (for example, inconsistency in the widths of spin elements), we made several patterns which are rotated at a certain angle compared to one another on the same substrate. By comparing the overall magnetization and vertex distribution before and after the demagnetization process, we can infer if lithography or deposition leads to the remnant magnetization. If the lithography-stigmatism-induced lattice defects are causing the remnant magnetization, the overall magnetization

should rotate with the lattice. On the other hand, if crystal anisotropy is the reason, the overall magnetization should remain on the same global direction on the substrate.

As shown in Fig 5.9, the remnant magnetization (indicated by the dashed line arrows) for the as-grown lattice seems not to rotate with the lattice, indicating the crystal anisotropy may play a role. For the demagnetized sample, the overall remnant magnetization seems to rotate with the lattice, indicating lithography-stigmatism-induced lattice defects may also play a role. However, the rotating angle of magnetic properties is not consistent with that of the artificial lattice and the magnitude of remnant magnetization varies, suggesting a more complex scenario than we describe above.

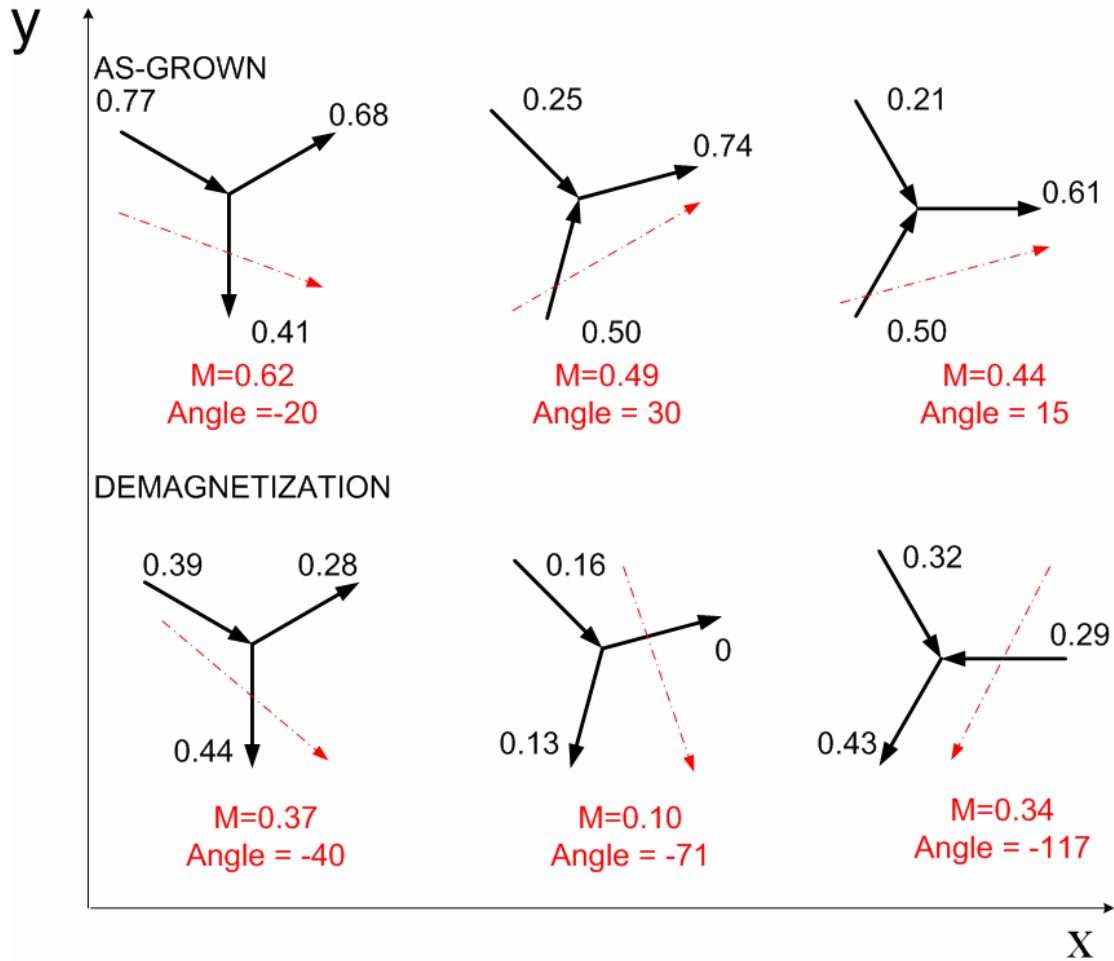


Figure 5.9 Remnant magnetization of kagome lattice before and after demagnetization. From left to right, 3 lattices are rotated 15° compared to each other. M is the magnitude of the remnant magnetization. And Angle is the direction of the remnant magnetization, also indicated by the dash line arrows. The values besides each spin in the figure denote the average magnetization for spins along that direction.

The demagnetization process makes the vertices' distribution more balanced if not fully consistent. However, the "majority vertices" remain majority, or only share majority/minority status with their anti-parallel vertices at $\Delta\theta=180^\circ$. For example, in Fig 5.10, the 150° vertices for pattern1 have the highest ratio as grown and remain the highest after demagnetization. While for pattern 3, -150° and -90° outstands others

for the as grown sample. After demagnetization, their opposite directions (30° and 90°) become more probable.

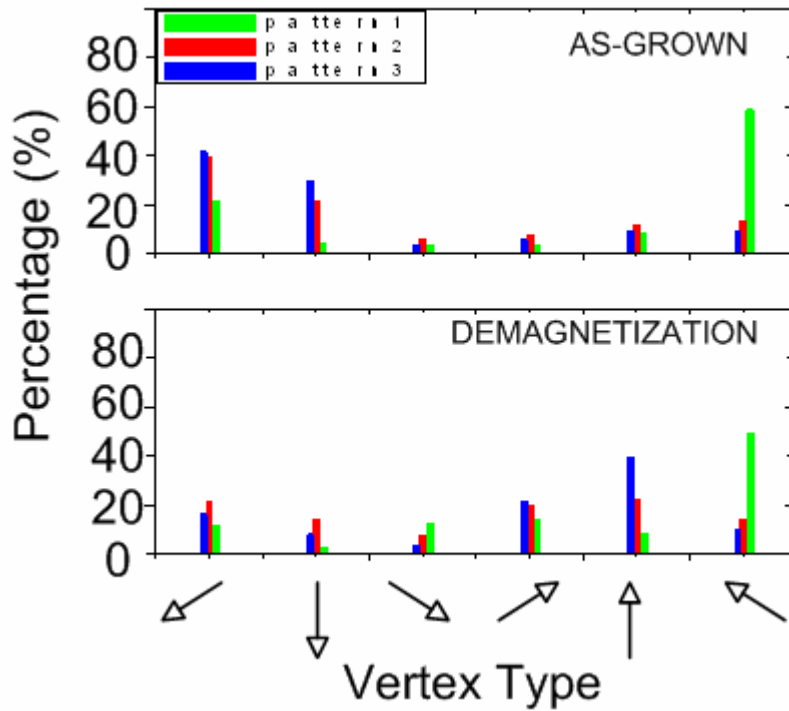


Figure 5.10 Vertex distribution before and after demagnetization. Upper panel: as-grown sample; Lower panel: demagnetized sample.

To investigate how the lithography stigmatism defects like width variation could effect the frustration in our system, we utilized a sample with isolated islands which happen to have obvious width variation (Fig 5.11).

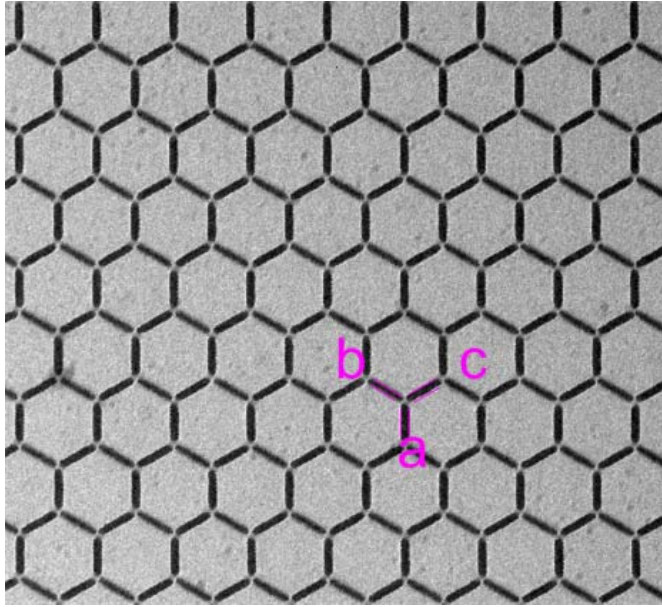


Figure 5.11 A kagome spin ice sample with various widths.

We measured the widths for 50 elements in each direction respectively, and found that the difference between three sub-lattices can not be ignored. Among them, sub-lattice **b** has the narrowest average width.

$$w_a = (1.00 \pm 0.03)w_0$$

$$w_b = (0.78 \pm 0.02)w_0, \text{ where } w_0 \text{ is the average widths for the vertical spin sub-}$$

$$w_c = (0.97 \pm 0.03)w_0$$

lattice (denoted as **a** in picture).

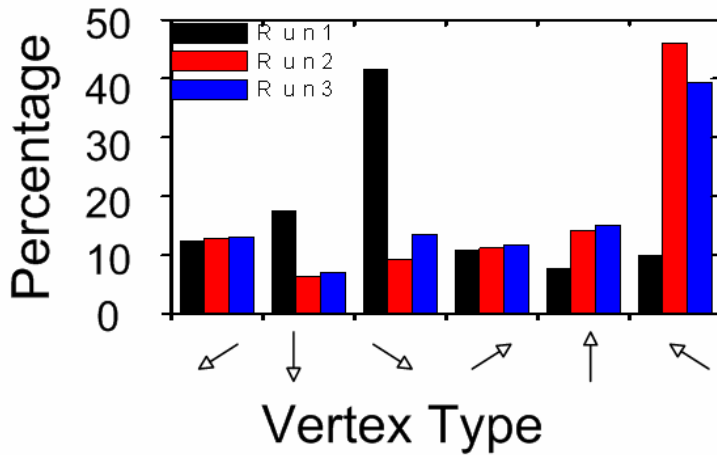


Figure 5.12 Vertex distribution after demagnetization for sample in Fig 5.10.

The demagnetized sample shows clear preference for the vertex aligned in **b** direction. This preference maybe explained by the shape anisotropy. Because narrower magnetic elements have larger shape anisotropy, the spins in them are more aligned along their length and more difficult to switch.

In summary, we systematically investigated the symmetry breaking in an artificial kagome spin ice. We found strain in the fabricated lattice could change the vertices' distribution and correlations. The lithography-induced defects associated with the lattice and crystal anisotropy during deposition may play a complex and combined role in determining the remnant magnetization and vertex distribution.

Chapter 6 Summary and future works

Geometrical frustration is known to significantly modify the properties of many materials (Chapter 2). Pyrochlore spin ice and hexagonal water ice are canonical systems[70, 71] that show the effects of frustration in both heat capacity[15, 17] and dynamical response [72, 73], and frustration also influences the mechanical response of water ice[74], with geologically significant implications. In both instances, microscopic ordering principles on the lattice lead to a macroscopic degeneracy of configurations. The degeneracy may be lifted by applying a magnetic field, as in the case of kagome plateau of pyrochlore spin ice (Chapter 3 and references in there). This degeneracy may also be modified or lifted by lattice imperfections, as in the case of KOH-doped water, where a first-order transition to an ordered ground state emerges [75]. Unfortunately, these effects are difficult to model or predict, because existing experimental techniques cannot directly observe the local ordering, near lattice defects or otherwise. To address this long outstanding problem, recent interest[30, 32, 76, 77] has focused on fabricating systems that allow the effects of frustration to be physically modeled and the resulting local configurations to be directly observed.

In this thesis, I present an artificial approach to kagome lattice. The kagome lattice is a two-dimensional structure composed of corner-sharing triangles and is an essential component of the pyrochlore spin ice structure (Chapter 3). By constructing magnetic nano-bar elements into the kagome lattice, the magnetic interactions between these elements mimic those between spins in a kagome spin ice. The realized artificial spin ice system rigorously obey the ice rule (2-in 1-out or 1-in 2-out

configuration at a vertex of three elements), thus providing a sought-after model system appropriate for further studies.

Chapter 4 investigates a ground state of the artificial kagome spin ice brought by demagnetization procedure. We observed short-range ordering and absence of long-range disorder, as well as the relative low remnant magnetization in the system, which are signatures of geometrically frustrated materials in their ground state. The rigid adherence to local ice rule further verifies the validity of this artificial approach and correlates our magnetic structure to real spin ice.

Furthermore, correlations in our artificial spin ice system suggest a strong role for dipolar effects, an essential component of spin ice models. Also the charge correlation (charge ordering coefficient) and Shannon entropy we calculated suggest that the degeneracy of our lattice is lifted from a completely disordered kagome spin ice system, and close to a “true” ground state that’s usually found as the kagome plateau in pyrochlore spin ice when applying a field in $\langle 111 \rangle$ direction.

The advantage of artificial spin ice is that we can probe the spins locally and have the flexibility to tune the system artificially. In Chapter 5, I discussed the magnetic field effects and strain effects, both investigated by directly looking at local spins.

When applying a magnetic field to the system, the spins change from disorder to order. Spin flipping in the magnetization reversal process prefers to propagate along zigzag chains. The chain flipping process may also happen in real spin ice, but that can not be probed directly. Artificial strain induces partial ordering and

symmetry breaking in the lattice, which mimics the pressure effects in real spin ice and spin liquid[66-68].

We also observed a symmetry breaking problem in the non-strained sample. The symmetry breaking is thought to be due to either the lithography (stigmatism during writing) or film deposition (crystal anisotropy). We noticed that the spins are not ordered even for the as grown sample. Although we have investigated this problem using a series of rotation patterns, further experiments need to be done.

One proposed future experiment is to put the substrate in an in-plane magnetic field during metal deposition. The field will induce spins to be ordered as-grown, inducing controlled crystal anisotropy. If crystal anisotropy is also the main reason for symmetry breaking after demagnetization, a more prominent remnant magnetization should be expected.

Another future work that worth doing is to further investigate the magnetic field induced spin flipping, especially apply a field to a demagnetized lattice. The demagnetized lattice renders us various local spin configurations. In magnetic charge model, those local spin configurations mean different charge contribution and different local magnetic force. Thus spin flipping at any local position may be different regarding the required external magnetic field. By mapping our observation to numerical calculation using magnetic charge concept, we may find an accurate model for the spin ice. Such models are currently under development by collaborator Oleg Tchernyshyov and Paula Mellado at Johns Hopkins University.

Results here demonstrate that the magnetic honeycomb structure is an ideal artificial spin ice system for studying the effects of frustration. Its simplicity and ease

of fabrication make it a robust platform for studying the influence of lattice imperfections in geometrically frustrated physical systems. Additionally, it achieves this without the need for mathematical approximations or lengthy computations[50] and without the trial-and-error typically associated with materials discovery. As demonstrated by the relatively good agreement between our correlations and the results of Monte Carlo simulations, the demagnetization process we employ might also serve in a more general sense as an efficient proxy for other computer models that search for optimal solutions in configuration space. With appropriate modifications, the artificial spin ice approach may well open the door to solving other optimization problems as well.

The artificial kagome lattice also has potential application in high density magnetic storage because the system can access a very wide range of nearly degenerate states. If information were encoded within a low energy configuration of the moments, the energetic driving force for local magnetization reversals could be suppressed by this near-degeneracy, even for highly dense arrays[30].

Appendix A: Lorentz TEM and Contrast Transfer Function

The Lorentz transmission electron microscope was first used to image domains by simply defocusing the objective lens [47, 48] (See Fig A.1). The observed contrast can be understood qualitatively in terms of the Lorentz force acting on the moving electrons as they travel through the magnetic foil.

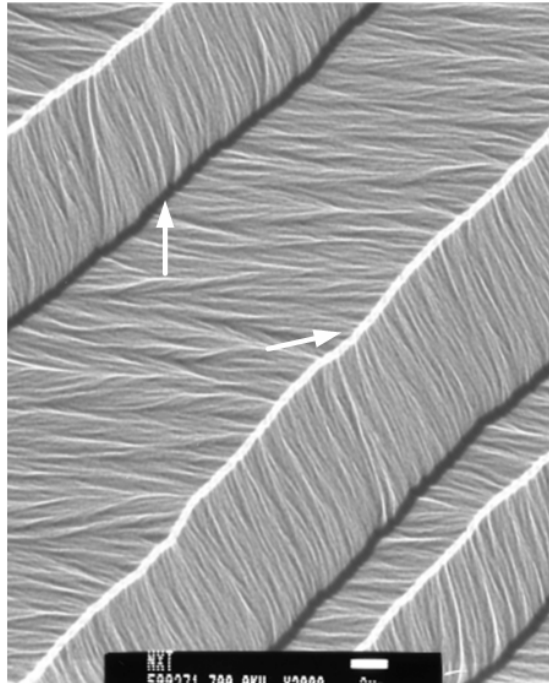


Figure A.1 Lorentz TEM image of a permalloy thin film shows domain structures. The arrows indicate two 180° domain walls which are shown as bright or dark edges.

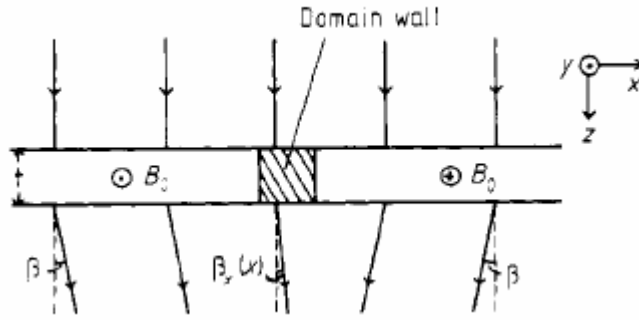


Figure A.2 The deflection of electrons on passing through a uniform ferromagnetic foil that contains one domain wall. Reproduced from [48].

Assuming the electrons are incident in the z direction onto a thin sample lying in x - y plane as shown in Fig A.2, and there are two domains in which the magnetizations are along $+y$ and $-y$ respectively, the electrons passing through the domains will be deflected in different direction. The magnitude of the Lorentz deflection angle β is given by

$$\beta = eB_0\lambda t / h ,$$

where e is the electronic charge, h is Planck's constant, λ is the electron wavelength, t is the sample thickness and B_0 is the magnetization.

If the component of magnetic induction perpendicular to the beam varies with location, we can define a local Lorentz deflection angle. For example, if the magnetization is a function of both x and z , the local deflection angle would be

$$\beta_y(x) = e\lambda / h \int_{-\infty}^{\infty} B_y(x, z) dz = e\lambda B_y(x)t / h ,$$

here $B_{y(x,z)}$ is the local value of the y component of the magnetic induction.

For accurate quantitative analysis of the Lorentz image, a more quantum mechanical description of the electron-specimen interaction is desirable. Such a description was provided by Aharonov and Bohm [78] who showed that the effect of

magnetic induction was to introduce a phase shift between two electron beams which originated from the same point and were subsequently rejoined after traveling different paths which enclosed magnetic flux N . The phase shift is given as

$$\varphi = 2\pi eN / h$$

So, the phase shift between any two points with x coordinates x_1 and x_2 (Fig A.3) is

$$\varphi(x) = 2\pi e t / h \int_{x_1}^{x_2} B_y(x) dx$$

From this point of view, Lorentz microscope can be seen as a branch of phase contrast electron microscopy.

The intensity contrast at the image plane can be obtained using the contrast transfer function. The electron wave emerging from the bottom surface of specimen can be written in the form of $f(x, y) \exp(2\pi i k_z z)$ where $f(x, y)$ is the specimen transmittance. For the magnetic foil talked above,

$$f(x, y) = \exp[i\varphi(x)]$$

The subsequent propagation of the electron wave to the image plane can be seen as a two-stage process. Entering the back focal plane of the objective lens, the electron disturbance $g(k_x, k_y)$ can be described by the Fourier transform of $f(x, y)$

$$g(k_x, k_y) = \iint f(x, y) \exp(-2\pi i(k_x x + k_y y)) dx dy, \text{ where } k_x, k_y \text{ are the spatial}$$

frequency.

Considering the finite size of electron lenses and aberrations, the wave is further modified, and on emerging from the back focal plane has the form

$$g(k_x, k_y) t(k_x, k_y), \text{ where}$$

$t(k_x, k_y) = A(k_x, k_y) \exp\{-2\pi i[C_s \lambda^3 (k_x^2 + k_y^2)/4] - [\Delta z \lambda (k_x^2 + k_y^2)/2]\}$, where C_s is the spherical aberration coefficient of the objective lens and Δz is the defocus. Finally the form of the electron disturbance in the image plane is a second Fourier transformation and the image intensity is

$$I(x', y') = \left| \iint g(k_x, k_y) t(k_x, k_y) \exp[-2\pi i(k_x x' + k_y y')] dk_x dk_y \right|^2$$

In defocus of Fresnel mode of Lorentz TEM, the magnetic contrast is generated by introducing a non-zero value of Δz . The contribution by the pupil function or spherical aberration are usually insignificant, so

$$t(k_x, k_y) \approx \exp[\pi i \Delta z \lambda (k_x^2 + k_y^2)]$$

Under these conditions, the integral above can be written in terms of a convolution between $\exp[i\phi(x)]$ and the Fourier transform of $t(kx, ky)$. Thus the intensity equation becomes

$$I(x', y') = \left| \exp[i\phi(x')] * \exp[\pi i (x'^2 + y'^2) / \lambda \Delta z] \right|^2, \text{ where } * \text{ means convolution}$$

integral. The below Fig 3.13 illustrates the contrast understood classically by the electron beam deflection.

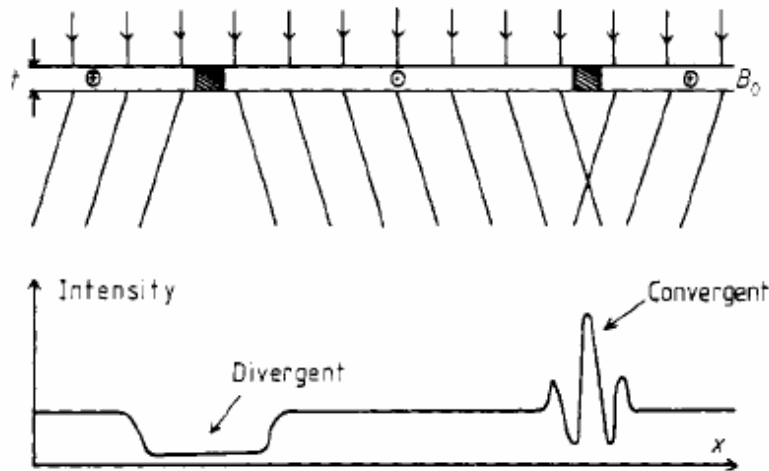


Figure A.3 Schematic representation of the intensity distribution in a fresnel image of a ferromagnetic foil containing two 180 domain walls. Reproduced from [48].

To simulate the contrast of single-domain needle-shaped elements, we use a standard contrast transfer function [49]. Fig A.4 shows that Lorentz contrast simulation of a magnetic bar elements has over-focus Lorentz contrast featuring a dark edge and a bright edge depending on the magnetization direction. The TEM images verified the simulation. Simply, this can be explained by deflection of the e-beam by Lorentz force when it passes through a magnetic element.

Using a right-hand rule, we can uniquely specify the magnetization direction for each element, as shown by the colored arrows. We verify the magnetic origin of the contrast both by through-focus imaging and by in-situ field reversal.

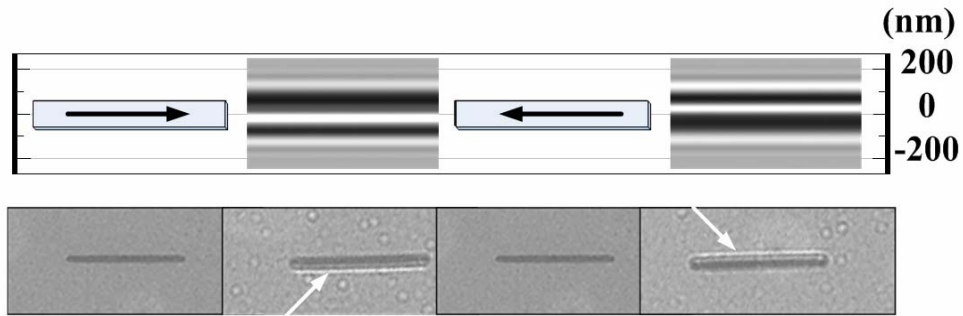


Figure A.4 Contrast transfer function simulation and Fresnel image of magnetic nano bar elements. Bright fringes running along the long edges of each element; from these the magnetization orientation can be deduced.

Matlab code of the contrast transfer function

```

profile = [zeros(200,512);ones(100,512)*1;zeros(212,512)];%profile of a magnetic bar element
e=1.602e-19;%electron charge, unit C
h=6.626e-34;% planck constant, unit J.s
mu=4e-7*pi; % permeability, unit Wb/m^2
Ms = 0.9 * (1/mu); %saturation magnetization of Py, 0.3 Tesla
z=22; %thickness of permalloy, unit nm
phaseM=(2*pi*e*z*1e-9/h).*Ms*mu.*cumsum(profile,1).*1e-9; %phase change due to magnetic

theta=0.006526;% interaction constant, for 300kV theta - 6.526 (mrad/V*nm), for 200kV,
theta=0.007288 eq2.35
Vc=-26; % mean inner potential of permalloy, [79]
phaseE=theta*Vc*z.*profile; % phase change due to electrostatic potential
phase1=phaseE+phaseM;
profile=[profile,fliplr(profile);flipud(profile),fliplr(flipud(profile))]; % symmetry construction for FFT
phase1=[phase1,fliplr(phase1);flipud(phase1),fliplr(flipud(phase1))];
g=fft2(exp(i.*phase1)); %reciprocal vector
qx=(1/1024).*ones(1024,1)*circshift([-512:511],[0,512]);
qy=qx';
Q = sqrt(qx.^2 + qy.^2);
lamda=2.24e-3;%wavelength, unit nm for 300kv
Cs=1e10; %Spherical aberration coefficient
theta_c=(0.01e-3);%beam divergence angle
df=1600000; %defocus value
chi=pi.*(df.*lamda.*(Q.^2)).%+0.5*Cs*lamda^3*Q.^4; %Equation 28.8 of [80]
t=exp(-(pi^2)*(theta_c^2).*((df.*Q).^2)); %envelope function, Equation 28.53 of [80]
intensity=(abs(iff22(g.*t.*exp(-i.*chi))))).^2;
figure(1); imagesc(intensity(1:512,1:512));

%%% end %%%

```

Appendix B: Lithography Procedure

The Bi-layer resist lithography procedure used in Chapter has been discussed by others [81]. To avoid redundancy, some materials appeared there are not included here. Only brief recipes and parameters I used for the resist spinning, deposition and lift off are given below.

The resist recipe utilizes both polymethyl methacrylate (PMMA) 950K and 495K from Microchem (www.microchem.com). This recipe was intended for metal liftoff and pattern has an undercut to aid in lift-off. The spin coater used is SCS G3-8.

1. Layer1 Spin 495K PMMA @6000rpm, 45 sec.
2. Bake on hotplate, 150°C, 8 minutes.
3. Layer 2 Spin 950K PMMA @6000rpm 45 sec.
4. Bake on hotplate, 150C, 8 minutes.
5. Spin aquaSAVE (a water-soluble conductive polymer from Mitsubishi, used to prevent charging and help focus) @ 6000rpm, 45 sec.

After e-beam lithography, the sample was developed to get rid of the exposed region of resist.

1. Put in water to wash off aquaSAVE for 2 min.
2. Put in MIBK (Put in methyl isobutyl ketone):IPA(isopropyl alcohol)=1:3 (volume) for 2 min
3. Put in IPA for 1-2 min and blow dry.

Following developing, a deposition step was performed in which a material was placed in the exposed and developed regions of the pattern. Here we deposited

$\text{Ni}_{0.8}\text{Fe}_{0.2}$ using an e-beam evaporator. The deposition rate is 1.0-2.0Å/s. After depositing Permalloy, a 5nm Aluminum protective layer was deposited.

The last step was lift-off in which the resist was removed along with the metal which lies on top of resist in the undeveloped regions. This was done by placing the substrate, resist and evaporated metal included, into a solvent which dissolves the resist.

- 1) Put in PRX-127 photoresist stripper (www.microchem.com) for 60min.
- 2) Spray rinse with PRX-127 using a wash bottle.
- 3) Spray rinse with IPA using a wash bottle, and then blow dry.

Before putting the sample into TEM for observation, another 5nm Aluminum anti-charging layer was usually deposited onto the sample using e-beam evaporator.

Appendix C: Multi-ferroic materials

C.1 Multiferroic and Magnetoelectric materials

Originally, multiferroics are used to describe single phase materials in which there are two or more the so-called ferroic properties: ferroelectricity, ferromagnetism and ferroelasticity[82]. Because there is more than one order parameter in one the system, they may interact with each other. The interaction between ferroelectricity and ferromagnetism in such materials is called Magneto-electric (ME) coupling. Magneto-electric effect in a single-phase crystal is traditionally described in Landau theory[83, 84]. Examples of single phase multiferroics include Cr_2O_3 [85], BiFeO_3 [86] and others[87, 88].

However, magneto-electric coupling may also arise indirectly through strain mediation in materials where the magnetic and electrical order parameters are in separate but intimately connected phases[89]. Each phase may be independently optimized for room temperature performance and the coupling limit is lifted. This type of magneto-electric coupling can be achieved in the form of composites[90], laminates [91, 92]or epitaxial multilayers[93].

In our experiment, we used $\text{BaTiO}_3\text{-CoFe}_2\text{O}_4$ (BTO-CFO) thin film nano-composite material prepared by pulsed-laser deposition on MgO substrates[3]. It has a nominal thickness of 180nm. X-ray diffraction and TEM experiments show that the BTO and CFO were separated into two phases in the thin film by self-assembly (Fig C.1). The two phases have a pillar-in-matrix geometry, in which the CFO pillars occupy about 35% in volume and have diameters of 20-30 nm, and their distribution

and size are roughly uniform. Both BTO and CFO phases have their [100] lattice direction perpendicular to the thin film plane [3].

Polarization-electric field hysteresis loop measurement and magnetization measurement show that the film has ferroelectric and magnetic ordering simultaneously. More interestingly, the magnetization versus temperature curve measured at $H \sim 100$ Oe, shows a distinct drop in magnetization at the ferroelectric Curie temperature, thus indicating a coupling effect between the ferroelectric and magnetic subsystem. For a more detailed description of the BTO-CFO sample, please refer to Multiferroic BaTiO₃-CoFe₂O₄ Nanostructures paper of Zheng *et al.* [3].

In this nano-pillar-in-matrix kind of multiphase materials, the properties strongly depend on the pillar size and composition, as well as the uniformity. A localized dielectric measurement is a convenient and effective method to check the quality of the film and to find the nanostructure/composition dependence of the electrical properties. In this chapter, I introduce localized dielectric measurements of BTO-CFO using a microwave microscope[94]. The measurement of relative dielectric constant has a good sensitivity (about ± 4 in the range of 200~1000) and high spatial resolution ($\sim 1\mu\text{m}$).

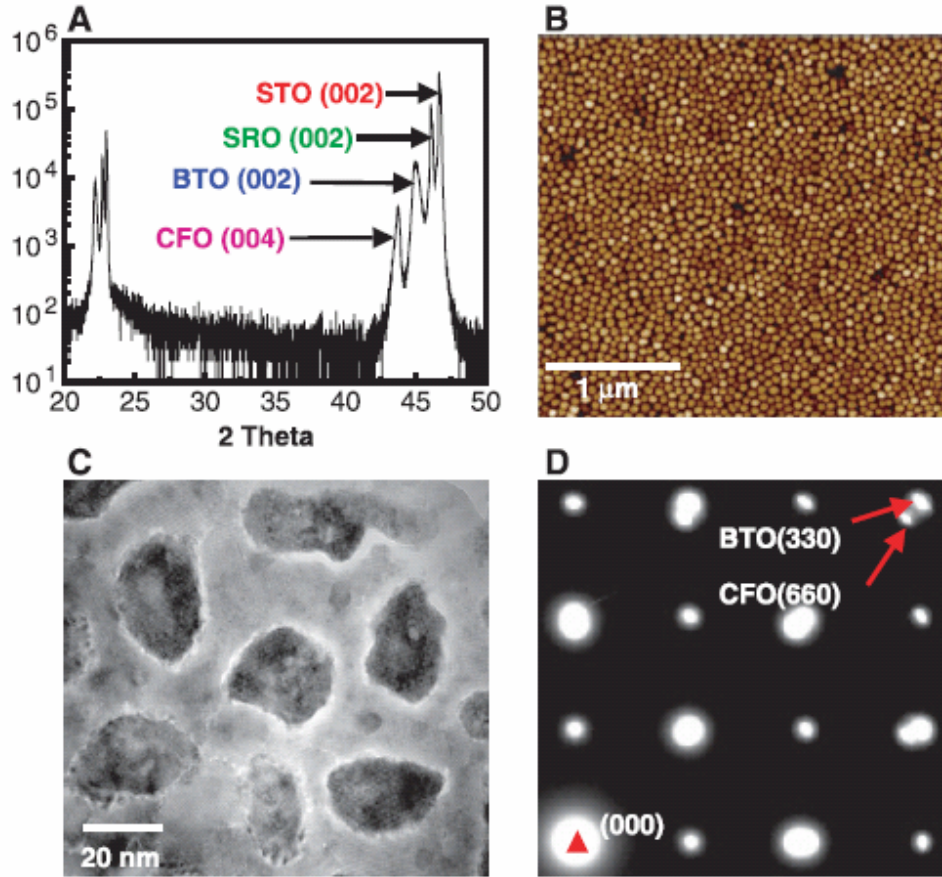


Figure C.1 The BTO-CFO thin film nano-composite structure characterization. (A) X-ray ($\theta-2\theta$) scan showing only the (00l) type peaks, corresponding to CoFe_2O_4 , BaTiO_3 , SrRuO_3 , and the SrTiO_3 substrate. (B) AFM topography image of the film showing a quasi-hexagonal arrangement of the CoFe_2O_4 nanopillars. (C) TEM planar view image showing the CoFe_2O_4 nanostructures in the BaTiO_3 matrix. (D) Electron diffraction pattern of (C), illustrating the in-plane heteroepitaxy between CoFe_2O_4 and BaTiO_3 . Reproduced from [3].

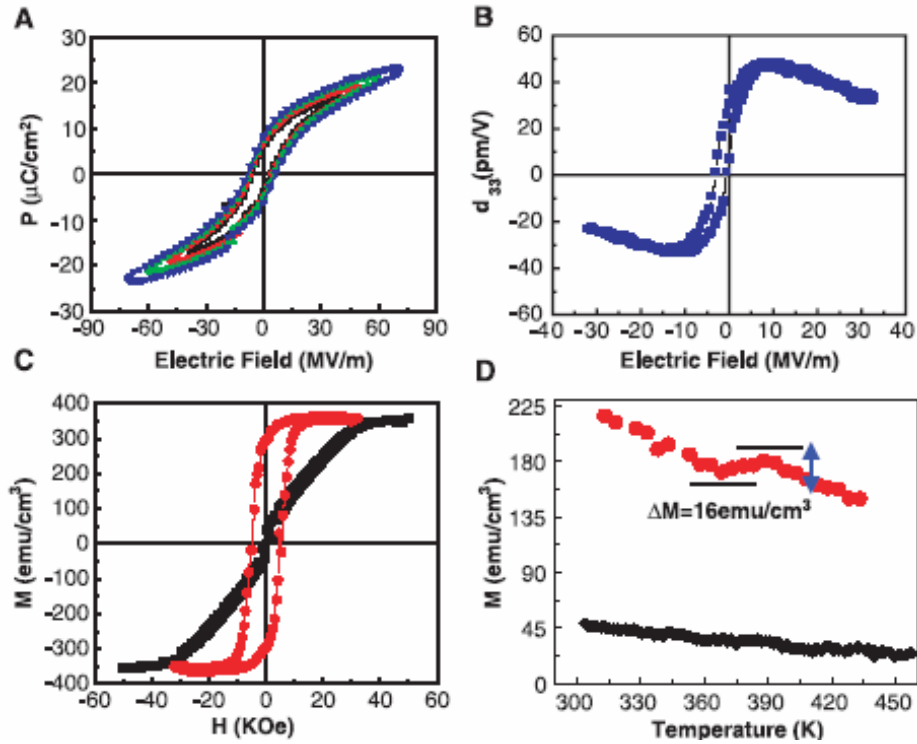


Figure C.2 The BTO-CFO thin film nano-composite magnetic and electric properties. (A) Polarization–electric field hysteresis loop showing that the film is ferroelectric with a saturation polarization $P_s \sim 23 \mu\text{C}/\text{cm}^2$. (B) Small-signal piezoelectric d_{33} hysteresis loop for a 50- μm -diameter capacitor. (C) Out-of-plane (red) and in-plane (black) magnetic hysteresis loops depicting the large uniaxial anisotropy. (D) Magnetization versus temperature curve measured at $H = 100 \text{ Oe}$, which shows a distinct drop in magnetization at the ferroelectric Curie temperature for the vertically self-assembled nanostructure (red curve); the multilayered nanostructure (black curve) shows negligible change in magnetization[3].

C.2 Microwave microscope

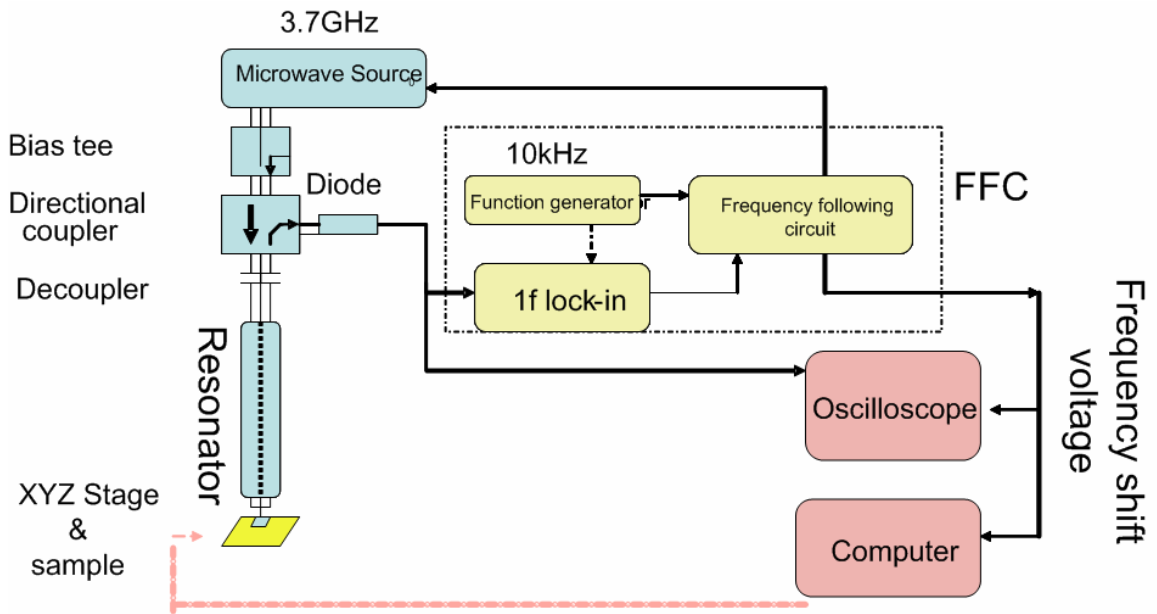


Figure C.3 Schematic illustration of a microwave microscope.

A scanning microwave microscope consists of an open-ended coaxial probe with a sharp, protruding center conductor [95]. The sample under the tip perturbs the resonator and causes a frequency shift. The frequency shift from the unperturbed condition (with a known sample as reference) to the perturbed condition (with the unknown sample to be measured) is related to the permittivity of the sample. Using perturbation theory [96], we calculated the frequency shift of the microscope as a function of the fields in the sample near the probe tip[97],

$$\frac{\Delta f}{f} \approx \frac{\epsilon_0}{4W} \int_{V_s} (\epsilon_{r2} - \epsilon_{r1}) \vec{E}_1 \cdot \vec{E}_2 dV ,$$

where ϵ_{r2} and ϵ_{r1} are the relative permittivity of the two samples. E_1 and E_2 are the calculated electric fields inside the two samples, W is the energy stored in the resonator, and the integral is over the volume V_s of the sample.

The dielectric constant vs. frequency shift curve for bulk and thin film samples are illustrated in Fig C.4. The shape of curve is determined by the probe geometry. For a defined geometry, we use Maxwell 2D software [98] to calculate the static electric field and stored energy in the sample. It is established that the static fields are a good approximation to the near-field structure of the tip. Combined with the equation above, the frequency shift vs. permittivity curve is calculated. The probe geometry is simplified to be an ellipsoid of revolution in contact with the sample (Fig C.5c). To find the probe geometry of the tip used in our experiment, i.e. the correct a , b , and c parameters, calibration points were measured with several known bulk samples. Fig C.4a shows a calculated curve of frequency shift vs. permittivity that fits our calibration points well when we choose $a=50\mu\text{m}$, $b=22\mu\text{m}$ and $c=2.6\mu\text{m}$. The geometry parameters are confirmed by SEM observation of the tip[99]. We can see that larger dielectric permittivity causes a more negative frequency shift of the microscope.

Fig C.4b simulates the thin film situation with the probe geometry determined by the bulk dielectric calibration step. In this simulation, we assume the substrate is MgO and the thin film thickness is 180nm, which is consistent with the samples used in this experiment. We assumed the sample has a disk shape with a diameter of $5000\mu\text{m}$ and a substrate thickness of $500\mu\text{m}$. In Fig C.4b we define the bare MgO substrate as the unperturbed condition, the frequency shift relative to MgO is

recorded to get the dielectric permittivity for the thin film samples to be measured.

The simulation curve is close to a straight line in the range from $\epsilon_r=100$ to $\epsilon_r=1100$ ($\epsilon_r \approx -15.425 - 2.336 \Delta f (kHz)$), so we can use the linear fit to estimate the dielectric constant of the thin films.

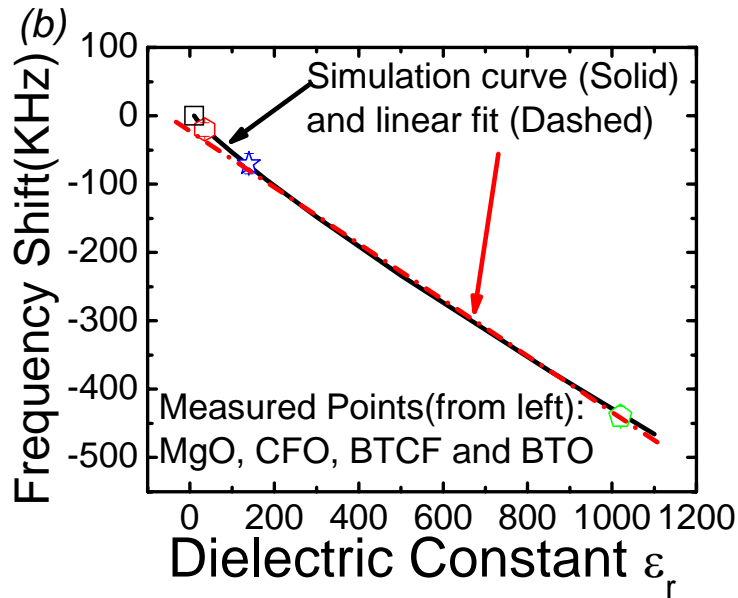
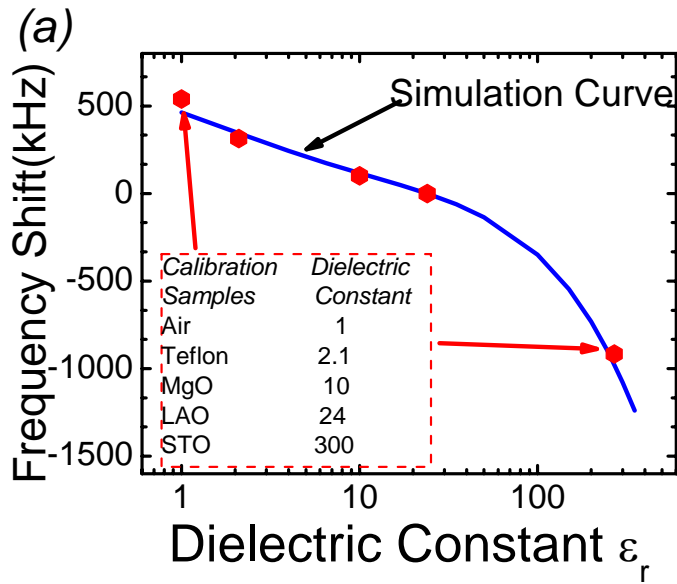


Figure C.4 Characterization curves of microwave microscope for dielectric measurements. (a) Data and simulation curve of frequency shift vs. permittivity for bulk samples (we use a bulk LAO substrate as the reference and all frequency shifts are given relative to it). The plot is in a linear-log scale to show the diversity of dielectric reference points. The relationship is non-linear for relative dielectric constant values below 50, but approximately linear above 50; (b) data and simulation for thin films. We assume MgO as the substrate and a film thickness of 180 nm. All frequency shifts are given relative to MgO. Note that this plot is in a linear scale.

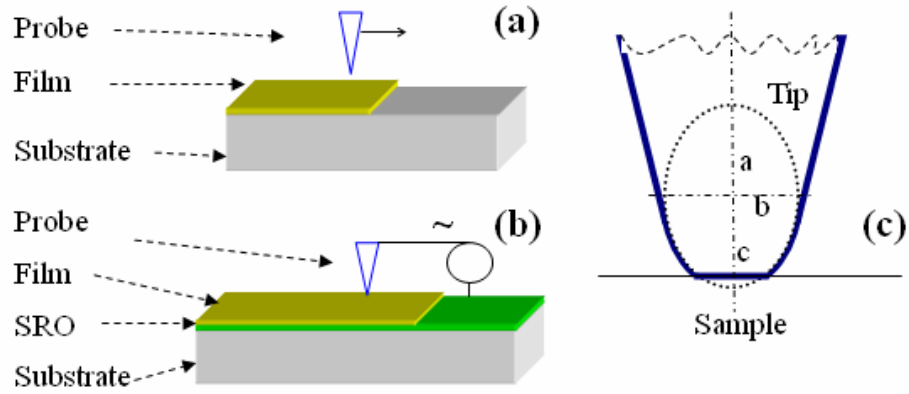


Figure C.5 Illustration of thin film sample and the microwave probe. (a) Sample schematic for dielectric measurements (BTO-CFO on MgO substrate with partly exposed MgO). (b) Sample schematic for non-linear dielectric measurements (BTO-CFO thin film on MgO substrate with a SRO counter-electrode layer). A dc and low frequency (Hz~kHz) ac voltage can be applied across the dielectric film between the tip and the counter-electrode. (c) Simplified geometry of the probe tip modeled as an ellipsoid of revolution in contact with the sample.

C.3 Dielectric properties of BTO-CFO thin film

Imaging Resolution

We scanned the microwave microscope tip across the lithographically-defined sharp edge between the BTO-CFO thin film and MgO bare substrate (Fig C.5a) and recorded the frequency shift. We use this design rather than measuring two separate samples because it can reduce the systematic error and noise in the dielectric constant determination, especially for the temperature dependence measurements presented below. There is a sharp change in frequency shift upon crossing the edge from MgO to BTO-CFO or BTO thin film (Fig C.6). The negative frequency change from MgO to BTO-CFO or BTO film indicates BTO-CFO and BTO have higher permittivity than MgO (for MgO, $\epsilon_r \sim 10$). We can convert the frequency shift values to relative permittivity values of $\epsilon_r = 140 \pm 6$ and 1020 ± 20 for BTO-CFO and BTO

respectively (at room temperature and 3.8 GHz). Assuming that the patterned edge and dielectric properties have a sharp change at the edge, from the scan with 0.1 μm step size (inset of Fig C.5b), we can also see the microwave microscope has a quantitative resolution[100] for dielectric constant of about 5 μm .

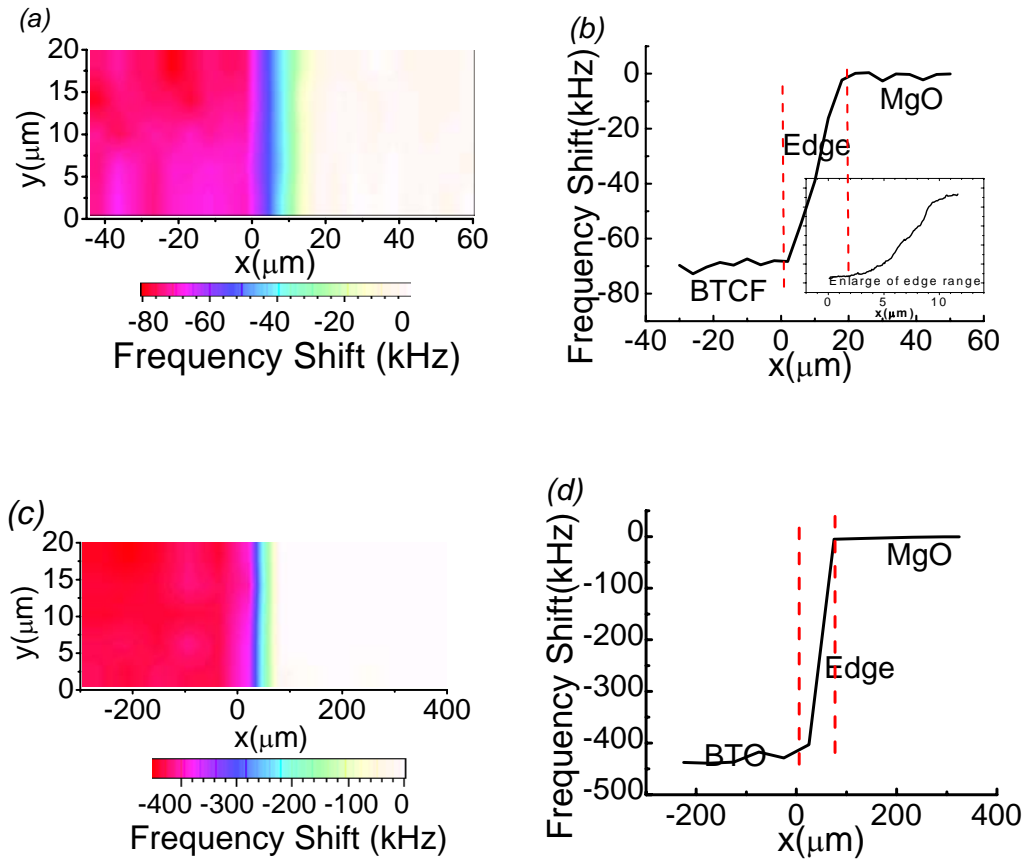


Figure C.6 Dielectric scanning and resolution characterization. (a), (c) Frequency shift scanning images at 3.8 GHz and room temperature crossing the BTO-CFO/MgO edge and BTO/MgO edge respectively, (b) (d) Single line scans from (a) and (c), inset of (b) is a scan across the BTO-CFO/MgO edge with 0.1 μm step size.

Dielectric Imaging

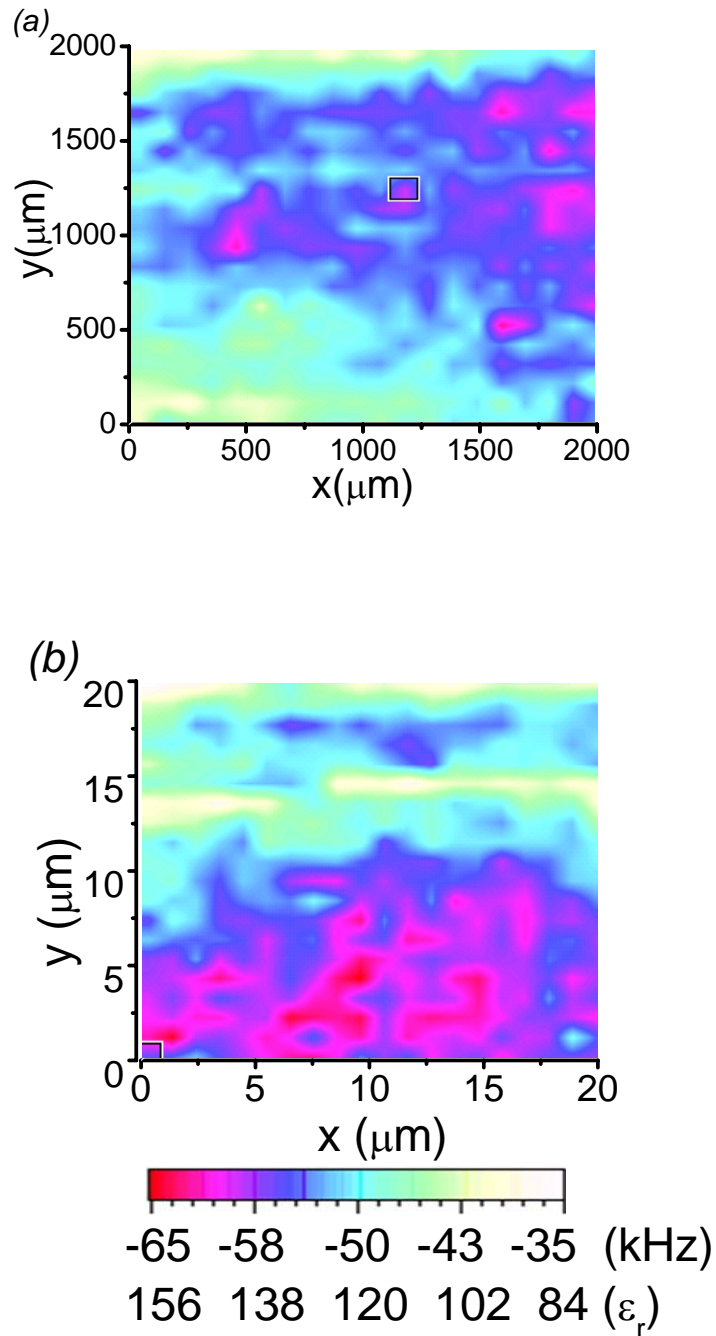


Figure C.7 Dielectric image of BTO-CFO thin film. (a) Linear dielectric constant image of BTO-CFO thin film, 2000 μm x 2000 μm scanning area with 5 μm step size, and (b) 20 μm x 20 μm area scanning image with 0.5 μm step size, both taken at 3.8 GHz and room temperature. Scale bar shows measured frequency shift and relative dielectric permittivity values.

A two-dimensional scanning image (Fig C.7a) shows that the BTO-CFO has a fairly uniform dielectric property with $\epsilon_r = 140 \pm 6.4$ averaged over a 2mm x 2mm area. The dielectric properties of this kind of nano-composite mainly depend on composition [101]. From Transmission Electron Microscope (TEM) and Atomic Force Microscope (AFM) measurement of this sample[3], it has roughly uniform composition in the plane of the film. That may explain the small range of dielectric constant variation observed. Fig C.7b shows a finer scanning image of the most inhomogeneous part of the film with 0.5 μm step size. The dielectric constant is $\epsilon_r = 136 \pm 8.2$ over this area. There is still contrast in the dielectric image on this short length scale, indicating a “qualitative” spatial resolution on the μm scale[100]. However, the resolution for quantitative imaging is larger and is typically governed by the tip geometry and the field confinement volume in the sample.

With this localized dielectric measurement technique, we also have the possibility of measuring the magneto-electric effect locally. Because applying a magnetic field would induce a magnetostriction of the CFO phase, this strain is transferred to BTO, which is equivalent to the stress effect on BTO. Our microscope has a sensitivity of 2 kHz in frequency shift, which corresponds to $\Delta\epsilon_r \sim 4$ in the 200-1000 relative dielectric constant range. Based on piezoelectric and magnetostriction coefficients ($e_{33} = 18.6\text{C} / \text{m}^2, q_{33} = 699.7\text{N} / \text{Am}$)[90], we estimate that a magnetic field of 3000 Oe is needed to get a measurable dielectric change in the BTO-CFO film.

C.4 Magneto-electro coupling imaging

The ME effect has been demonstrated through several different phenomena such as polarization change or dielectric change due to magnetic field, magnetization abnormalities at the Curie temperature, and polarization abnormalities at the magnetic transition temperature [102-105].

Some direct quantitative measurement methods of the ME effect have also been developed. For bulk samples, the ME effect can usually be measured directly by detecting the induced voltage in the sample with a lock-in amplifier when applying a magnetic field. In this case, a large dc magnetic field and a small quasi-static ac modulation magnetic field is applied to get the ME coefficient at different dc magnetic field values[106]. Since the ME effect is mediated by a mechanical interaction, the ME coefficient can also be greatly enhanced when choosing the modulation frequency near a mechanical resonance frequency of the sample [107]. A giant ME coefficient measured in bulk samples is reported as high as 8700mV/cm.Oe[108].

However, thin film geometry is not currently attractive for applications of the above measurement, because the ME voltage on the sample is usually small. Moreover, we would like to know how the ME effect depends on the local composition and nanostructure of the sample. In this section we present a proposal for ME measurement using a scanning near-field microwave microscope combined with lock-in techniques.

The experiment uses a microwave microscope shown in Fig C.8 which was originally used to measure the linear and nonlinear dielectric properties of thin films [95].

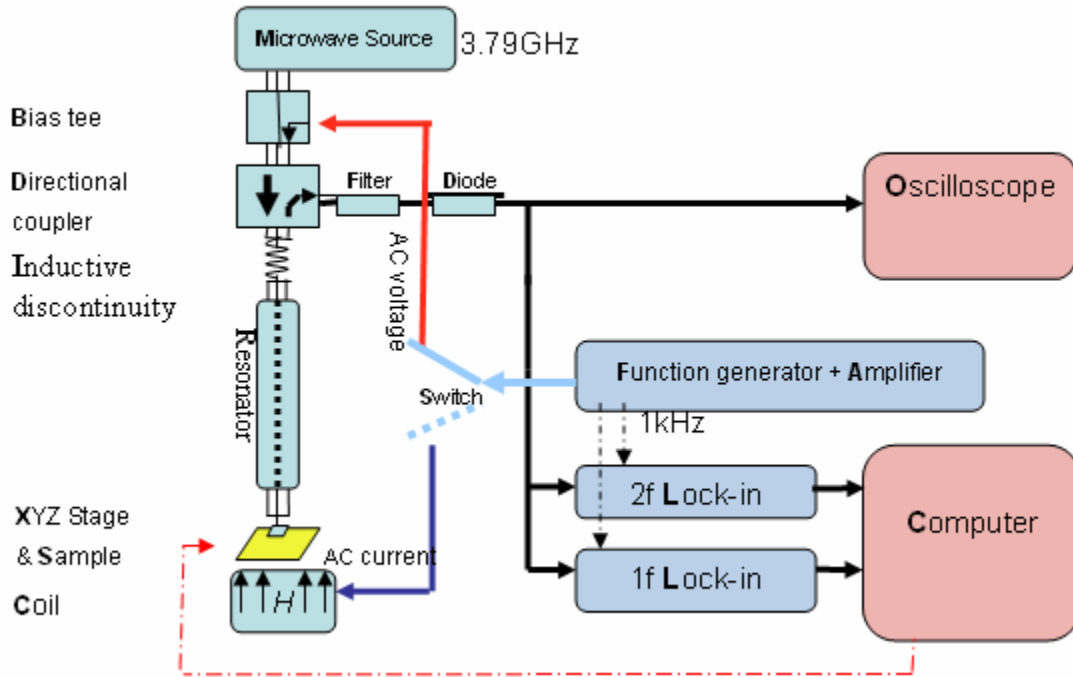


Figure C.8 Schematic diagram of Microwave Microscope for ME measurement. AC electric field or magnetic field was applied to the sample respectively. The reflected diode voltage was measured through a lock-in amplifier referenced to the modulation signal.

In our experiment, the microwave source frequency is adjusted to get the largest 2f lock-in signal, in our case about 3.79 GHz (Fig C.8). At this fixed frequency, an ac bias voltage or an ac magnetic field is applied to the sample. The ac bias voltage is applied through a bias tee and appears between the tip and the SRO counter-electrode. The ac magnetic field is applied by a cylindrical coil 7 cm tall and 5 cm in diameter, centered on the sample and the microscope tip. The applied field will change the local dielectric response of the sample through the ME effect. This will show up as a change in the reflection coefficient of the microscope. The

reflected signal from the microscope is measured as a function of the oscillating electric or magnetic field applied to the sample.

Low frequency electric field simulation with ac bias voltage in the thin film

In our experiment, the microscope tip is touching the thin film sample. The situation when a bias voltage applied is simulated in Fig C.9. In this simulation, we assume that the thin film material is uniform with a relative dielectric constant of 260. The dielectric constants of BTCF and BTO were measured on separate films grown directly on MgO with no counterelectrode, as described by [97]. (From other experiments at 3.8 GHz we find that BTO has a dielectric of 800, while CFO has a dielectric constant of ~ 35 .) The electric field in the sample is mainly in the vertical direction. The electric field is about $1.7 \times 10^4 \sim 3 \times 10^4$ V/cm per volt bias voltage.

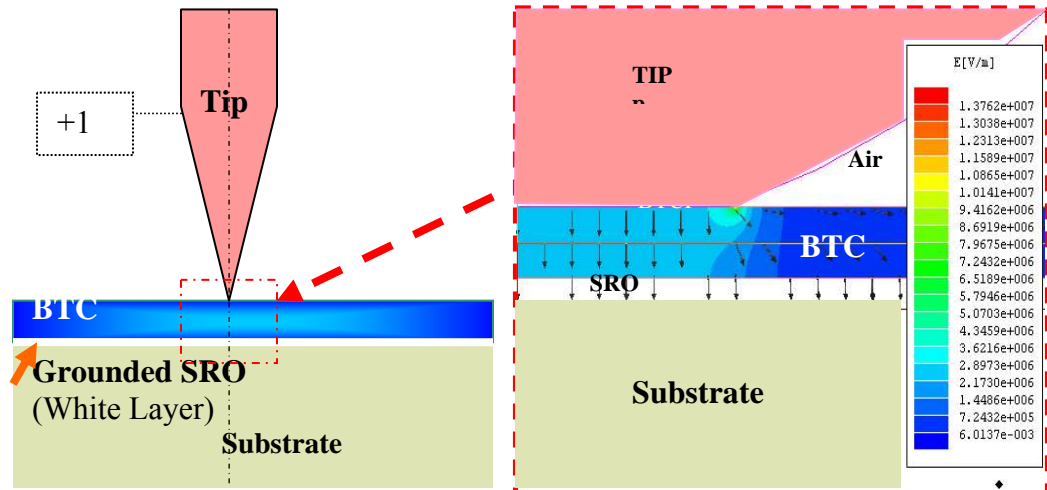


Figure C.9 Illustration of microscope tip, sample geometry (left) and electric field with a bias voltage (right). Vertical direction electric field was generated in the thin film beneath the tip area.

BTCF geometry and electric field due to ME effect when applying ac magnetic field

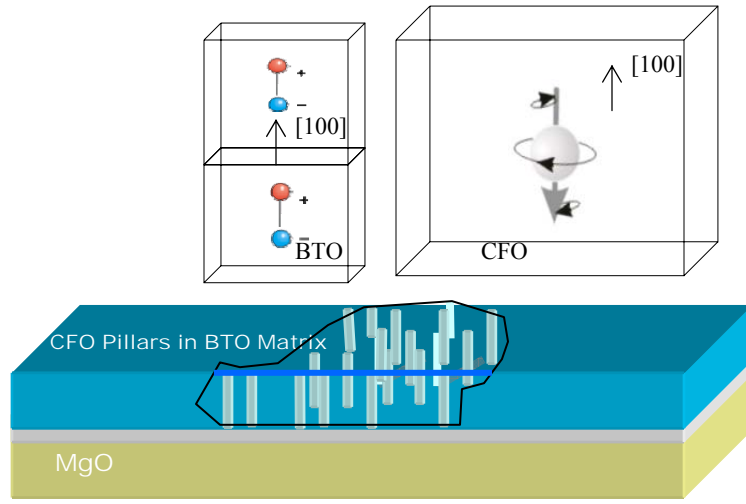


Figure C.10 Illustration of Thin film sample morphology (bottom) and BTO/CFO lattice (top). The CFO pillars are embedded in the BTO matrix. Both phases have their [100] direction perpendicular to the film plane.

In our sample, the CFO phase has a [100] direction which is perpendicular to the film plane. When an ac magnetic field is applied, this direction gains the largest magnetostriction. This magnetostriction is transferred to the BTO phase via mechanical interaction. Also the BTO [100] direction is parallel to that of CFO, hence we expect that an electric field in the vertical direction is produced via the piezoelectric effect, which is called the ME electric field.

A reasonable assumption is that the ME electric field produced by the magnetic field is equivalent to the electric field created by the bias voltage in terms of their direction and effects on the sample.

Diode Voltage Change with Electric Field

In theory, both the dielectric constant change $\Delta\varepsilon$ and the quality factor change ΔQ can change the diode voltage. They correspond to the shift and curvature change of the diode voltage versus frequency curve. Our experiments show that the curvature change ΔQ when changing the DC bias voltage on a BTO thin film sample can be ignored. Thus it is reasonable to assume that the diode voltage change comes from the dielectric constant change under electric field $\Delta\varepsilon$.

When applying a low frequency modulation electric field $E_{p3} = E_p \cos(\omega_p t)$, the dielectric constant becomes,

$$\begin{aligned}\varepsilon_{33} &\rightarrow \varepsilon_{33} + \Delta\varepsilon(E_{p3}) = \varepsilon_{33} + \varepsilon_{333}E_{p3} + \frac{1}{2}\varepsilon_{3333}E_{p3}^2 + \dots \\ &= (\varepsilon_{33} + \frac{1}{4}\varepsilon_{3333}E_p^2) + \varepsilon_{333}E_p \cos \omega_p t + \frac{1}{4}\varepsilon_{3333}E_p^2 \cos 2\omega_p t + \dots\end{aligned}$$

according to [109] and [97].

So, the differential change in the dielectric constant of the material $\Delta\varepsilon(E_{p3})$ will be

$$\Delta\varepsilon = \frac{1}{4}\varepsilon_{3333}E_p^2 + \varepsilon_{333}E_p \cos \omega_p t + \frac{1}{4}\varepsilon_{3333}E_p^2 \cos 2\omega_p t + \dots \quad (1)$$

The change in diode voltage due to a change in dielectric response of the sample is calculated according to a transmission line model of the microscope [97],

$$dV_{diode} = \eta(1-\eta)V_s^+ \frac{(A^2-1)Z_0}{[(Z_{dec} + AZ_0)Z_x + ARZ_0 + Z_0^2]^2} dZ_x \quad (2)$$

Where,

V_s^+ is the amplitude of the wave traveling into the microscope.

$Z_0 = 50\Omega$ is the characteristic impedance of the coaxial cable

Z_{dec} is the impedance of the inductive impedance discontinuity (decoupler)

Z_x is the impedance of the sample.

$\eta \cong 10^{\zeta/20}$ the coupling voltage fraction in the directional coupler

$$A = \frac{e^{rL} + e^{-rL}}{e^{rL} - e^{-rL}},$$

$$r = \alpha + i\beta,$$

L is length of the transmission line.

α is the attenuation constant in nepers/m

$\beta = \frac{\omega\sqrt{\epsilon}}{c}$ is the propagation constant of the transmission line resonator.

We can simplify equation (2) to $dV_{diode} = \left(\frac{1}{BZ_x + C}\right)^2 dZ_x$ (3)

with appropriate definitions of B and C. The sample impedance can be taken to be,

$$Z_x = \frac{1}{i\omega C_x} + Z' = \frac{1}{i\omega\epsilon \times \pi r_0^2 / h} + Z'$$

Where we take a simple model of the probe-sample capacitance C_x in which r_0 is the effective radius of the contact area between tip and sample, and h is thickness of thin film.

$$\begin{aligned} V_{diode} &= \left(\frac{1}{BZ_x + C}\right)^2 \times (\omega\epsilon\pi r_0^2 / h)^{-2} \times d\epsilon \\ \text{Thus,} \quad &= C' \left(\frac{1}{4} \epsilon_{3333} E_p^2 + \epsilon_{333} E_p \cos \omega_p t + \frac{1}{4} \epsilon_{3333} E_p^2 \cos 2\omega_p t \right) \end{aligned} \quad (4)$$

Where C' is constant determined by the geometry of the tip, the microscope and the diode sensor.

Our experiment uses a lock-in amplifier to extract the diode voltage signal. From Eq. (4) we see that when setting the reference signal of the lock-in amplifier at frequency ω_p , the output signal corresponds to the third-order dielectric and is linearly proportional to the applied electric field. When setting the reference signal of the lock-in at the doubled frequency $2\omega_p$, the output corresponds to the forth-order dielectric constant and is proportional to the square of the applied electric field[109]. These two signals both can be used in our experiment to determine the electric field induced by the magnetic field. However we found that the term corresponding to the

fourth order dielectric is more easily measured. In other words, when applying an ac modulation electric field or magnetic field to the sample, a reflection signal with double of modulation frequency can be seen. This is illustrated by the near-symmetric dielectric vs. bias voltage curve measured on a BTO sample, shown in Fig C.11.

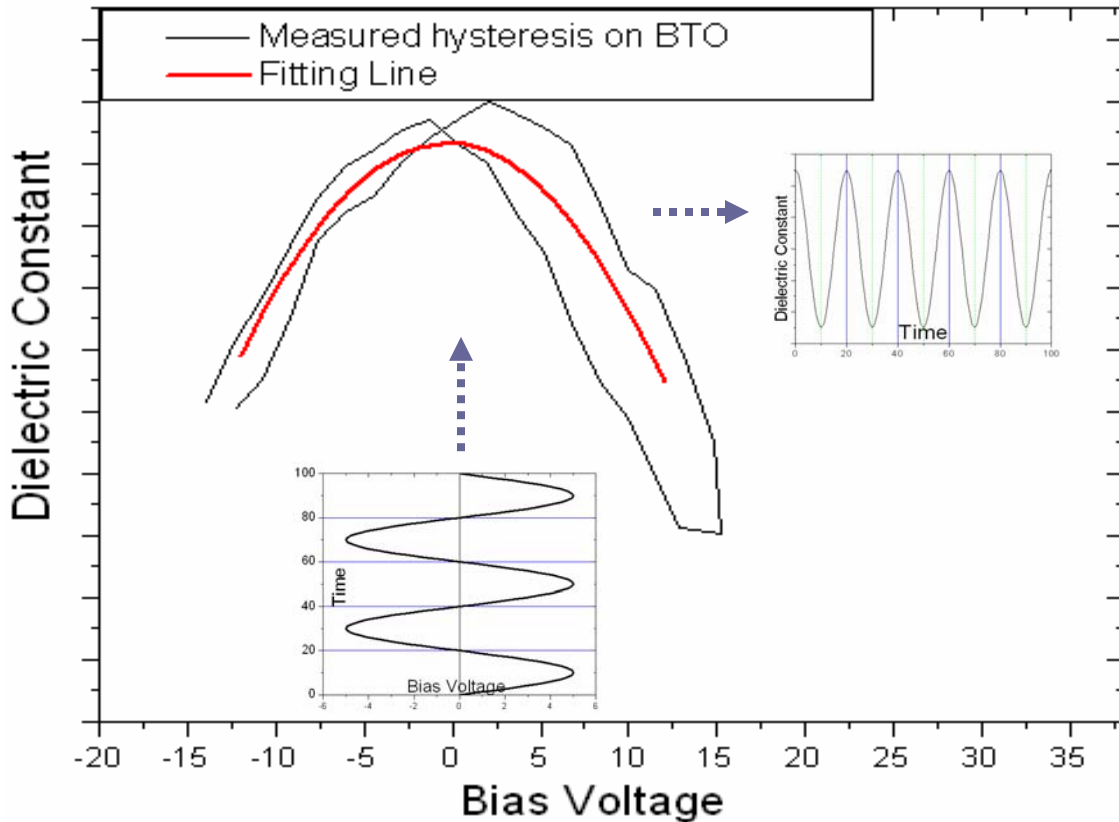


Figure C.11 Illustration of the dielectric constant change with ac electric field and the generation of 2f signal for a BTO/SRO thin film. There is a non-linear dielectric change in ferroelectric materials with an electric field. Bottom inset shows the applied AC electric field. Upper-right inset shows the dielectric change at double the frequency of the ac electric field.

Convert the data to ME coefficient

With the above assumption that the electric field produced by the magnetic field is equivalent to that produced by bias voltage in terms of their effect on the sample (both change the dielectric constant of the sample and influence the diode

voltage), we can convert the data to get an estimate of the ME coefficient as follows.

We essentially compare two different ways to change ϵ_{3333} . The ME coefficient is proportional to the ratio of the 2f lock-in voltages induced by the modulated magnetic and electric fields;

$$V_{2f}(H_p) = C \times \epsilon_{3333} E_p^2 = C \times \epsilon_{3333} \times \left(\frac{\partial E_p}{\partial H_p} \right)^2 \times H_p^2$$

$$= C \times \epsilon_{3333} \times \alpha_{ME}^2 \times H_p^2,$$

$$V_{2f}(V_b) = C \times \epsilon_{3333} E_p^2 = C \times \epsilon_{3333} \times \left(\frac{\partial E_p}{\partial V_b} \right)^2 \times V_b^2,$$

$$\text{Therefore } \alpha_{ME} = \left(\frac{V_{2f}(H_p)/H_p^2}{V_{2f}(V_b)/V_b^2} \right)^{1/2} \times \frac{\partial E_p}{\partial V_b} \quad (5)$$

Using data V_{2f}/H_p^2 and V_{2f}/V_b^2 for BTCF we have measured, and the simulation of the modulated electric field in the sample (Fig C.9), the result is $\alpha_{ME} = 204 \text{ V/cm.Oe}$, 191 V/cm.Oe and 133 V/cm.Oe for 3 different positions on the sample respectively.

Issues in the experiment

The advantage for the proposed magneto-electric measurement is that we can localize it to the μm scale. This provides the capability to investigate the relation between magneto-electric properties and local composition or nano-structure.

However, when applying an ac electric bias voltage, only the BTO piezoelectric phase underneath the tip area is subject to produce a strain response (electrostriction), while the CFO phase (no-electrostriction area) and other area away from the tip (lower-electric-field area) remain unchanged. So the BTO's response to

electric field is constrained and results in a smaller dielectric change compared to pure BTO under similar conditions (considering 65% BTO and 35% Air, since the dielectric constant of CFO is small and changes little with electric field).

Another challenge for this experiment is to make samples sufficiently insulating to prevent leakage currents contributing to the measured signal—a widespread problem undermining the measurement of ferroelectric polarization loops, as described in ref [110].

In summary, we measured the dielectric properties of BTO-CFO nanocomposites. The dielectric properties of BTO-CFO are similar to those of BTO. The measurement has a quantitative spatial resolution of approximately 5 μm . The possibility of localized magneto-electric measurement with this technique is also discussed.

Bibliography

- [1] W. Eerenstein, N. D. Mathur, and J. F. Scott, Multiferroic and magnetoelectric materials, *Nature* **442**, 759 (2006).
- [2] V. E. Wood, and A. E. Austin, Possible applications for magnetoelectric materials, *Int. J. Magn.* **5**, 303 (1974).
- [3] H. Zheng, J. Wang, S. E. Lofland, Z. Ma, L. Mohaddes-Ardabili, T. Zhao, L. Salamanca-Riba, S. R. Shinde, S. B. Ogale, F. Bai, D. Viehland, Y. Jia, D. G. Schlom, M. Wuttig, A. Roytburd, and R. Ramesh, Multiferroic BaTiO₃-CoFe₂O₄ Nanostructures, *Science* **303**, 661 (2004).
- [4] G. Toulouse, Theory of Frustration Effect In Spin-glasses .1., *Commun. Phys.* **2**, 115 (1977).
- [5] R. Moessner, Magnets with strong geometric frustration, *Can. J. Phys.* **79**, 1283 (2001).
- [6] P. G. Wolynes, and W. A. Eaton, The physics of protein folding, *Phys. World* **12**, 39 (1999).
- [7] S. T. Bramwell, and M. J. P. Gingras, Spin Ice State in Frustrated Magnetic Pyrochlore Materials, *Science* **294**, 1495 (2001).
- [8] A. P. Ramirez, in *Handbook of magnetic materials*, edited by K. J. H. Buschow (Elsevier Science, Amsterdam, 2001).
- [9] P. G. Debenedetti, and F. H. Stillinger, Supercooled liquids and the glass transition, *Nature* **410**, 259 (2001).
- [10] K. Binder, and A. P. Young, Spin glasses: Experimental facts, theoretical concepts, and open questions, *Rev. Mod. Phys.* **58**, 801 (1986).
- [11] J. A. Mydosh, *Spin Glasses: An Experimental Introduction* (Taylor & Francis, London, 1993).
- [12] A. S. Wills, R. Ballou, and C. Lacroix, Model of Localized Highly Frustrated Ferromagnetism: The kagome Spin Ice, *Phys. Rev. B* **66**, 144407 (2002).
- [13] T. Yoshioka, A. Koga, and N. Kawakami, Frustrated Ising Model on the Garnet Lattice, *Journal of Physical Society of Japan* **73**, 1805 (2004).
- [14] W. F. Giauque, and M. F. Ashley, Molecular Rotation in Ice at 10°K. Free Energy of Formation and Entropy of Water, *Phys. Rev.* **43**, 81 (1933).
- [15] W. F. Giauque, and J. W. Stout, The Entropy of Water and the Third Law of Thermodynamics. The Heat Capacity of Ice from 15 to 273°K., *J. Am. Chem. Soc.* **58**, 1144 (1936).
- [16] L. Pauling, The Structure and Entropy of Ice and of Other Crystals with Some Randomness of Atomic Arrangement, *J. Am. Chem. Soc.* **57**, 2680 (1935).
- [17] A. P. Ramirez, A. Hayashi, R. J. Cava, R. Siddharthan, and B. S. Shastry, Zero-point Entropy in 'Spin Ice', *Nature* **399**, 333 (1999).
- [18] E. O. Wollan, W. L. Davidson, and C. G. Shull, Neutron Diffraction Study of the Structure of Ice, *Phys. Rev.* **75**, 1348 (1949).
- [19] M. J. Harris, S. T. Bramwell, D. F. McMorrow, T. Zeiske, and K. W. Godfrey, Geometrical Frustration in the Ferromagnetic Pyrochlore Ho₂Ti₂O₇, *Phys. Rev. Lett.* **79**, 2554 (1997).

- [20] S. T. Bramwell, Condensed-matter Physics: Great Moments in Disorder, *Nature* **439**, 273 (2006).
- [21] M. J. Harris, S. T. Bramwell, P. C. W. Holdsworth, and J. D. M. Champion, Liquid-Gas Critical Behavior in a Frustrated Pyrochlore Ferromagnet, *Phys. Rev. Lett.* **81**, 4496 (1998).
- [22] R. Siddharthan, B. S. Shastry, A. P. Ramirez, A. Hayashi, R. J. Cava, and S. Rosenkranz, Ising Pyrochlore Magnets: Low-Temperature Properties, "Ice Rules," and Beyond, *Phys. Rev. Lett.* **83**, 1854 (1999).
- [23] S. T. Bramwell, M. J. Harris, B. C. den Hertog, M. J. P. Gingras, J. S. Gardner, D. F. McMorrow, A. R. Wildes, A. L. Cornelius, J. D. M. Champion, R. G. Melko, and T. Fennell, Spin Correlations in $\text{Ho}_2\text{Ti}_2\text{O}_7$: A Dipolar Spin Ice System, *Phys. Rev. Lett.* **87**, 047205 (2001).
- [24] M. Harris, Condensed-matter physics: Taking the frustration out of ice, *Nature* **399**, 311 (1999).
- [25] R. A. Shelby, D. R. Smith, and S. Schultz, Experimental Verification of a Negative Index of Refraction, *Science* **292**, 77 (2001).
- [26] M. C. K. Wiltshire, OPTICAL MATERIALS: Bending Light the Wrong Way, *Science* **292**, 60 (2001).
- [27] A.-P. Hynninen, J. H. J. Thijssen, E. C. M. Vermolen, M. Dijkstra, and A. van Blaaderen, Self-assembly route for photonic crystals with a bandgap in the visible region, *Nat. Mater.* **6**, 202 (2007).
- [28] D. J. Norris, Photonic Crystals: A view of the future, *Nat Mater* **6**, 177 (2007).
- [29] U. Welp, V. K. Vlasko-Vlasov, G. W. Crabtree, T. Carol, V. Metlushko, and B. Ilic, Magnetic domain formation in perforated permalloy films, *Appl. Phys. Lett.* **79**, 1315 (2001).
- [30] R. F. Wang, C. Nisoli, R. S. Freitas, J. Li, W. McConville, B. J. Cooley, M. S. Lund, N. Samarth, C. Leighton, V. H. Crespi, and P. Schiffer, Artificial 'Spin Ice' in a Geometrically Frustrated Lattice of Nanoscale Ferromagnetic Islands, *Nature* **439**, 303 (2006).
- [31] E. H. Lieb, and F. Y. Wu, edited by C. Domb, and M. S. Green (Academic, London, 1972).
- [32] G. Moller, and R. Moessner, Artificial Square Ice and Related Dipolar Nanoarrays, *Phys. Rev. Lett.* **96**, 237202 (2006).
- [33] In a square lattice with isolated islands, type I vertices in Wang et al paper are preferred. While in a connected square lattice, our experiments shows the preferred state would be ferromagnetic, i.e. type II vertices in Wang et al paper are preferred.
- [34] M. Tanaka, E. Saitoh, H. Miyajima, T. Yamaoka, and Y. Iye, Magnetic Interactions in a Ferromagnetic Honeycomb Nanoscale Network, *Phys. Rev. B* **73**, 052411 (2006).
- [35] Direct observation of the ice rule in an artificial kagome spin ice
- [36] K. Matsuhira, Z. Hiroi, T. Tayama, S. Takagi, and S. Sakakibara, A New Macroscopically Degenerate Ground State in the Spin Ice Compound $\text{Dy}_2\text{Ti}_2\text{O}_7$ under a Magnetic Field, *J. Phys. : Condensed Matter* **14** (2002).
- [37] T. Fennell, S. T. Bramwell, D. F. McMorrow, P. Manuel, and A. R. Wildes, Pinch points and Kasteleyn transitions in kagome ice, *Nat Phys* **3**, 566 (2007).

- [38] R. Higashinaka, H. Fukazawa, and Y. Maeno, Anisotropic release of the residual zero-point entropy in the spin ice compound $\text{Dy}_2\text{Ti}_2\text{O}_7$: Kagome ice behavior, *Phys. Rev. B* **68**, 014415 (2003).
- [39] R. Moessner, and S. L. Sondhi, Theory of the [111] magnetization plateau in spin ice, *Phys. Rev. B* **68**, 064411 (2003).
- [40] The low energy vertex degeneracy for square-ice is $6/16=0.375$, whereas for kagome ice it is $6/8=0.75$.
- [41] M.J. Donahue, and D.G. Porter, OOMMF User's Guide v1.0, NIST, Gaithersburg, MD.
- [42] Specifically, a 3-in or 3-out configuration prefers a vortex structure at the vertex, and the total energy is about 1.73 times larger than a ice-rule configurations (2-in-1-out or 1-in-2-out), where the magnetization changes gradually at the vertex forming Neel walls.
- [43] G.R. Brewer and, and J. P. Ballantyne, *electron-beam technology in microelectronic fabrication* (Academic Press, New York, 1980), p. xi.
- [44] K. Suzuki, S. Matsui, and Y. Ochiai, *Sub-half-micron lithography for ULSIs* (Cambridge University Press, Cambridge, 2000), p. xvii.
- [45] J. M. Shaw, M. Hatzakis, J. Paraszczak, J. Liutkus, E. Babich, *Organosilicon Polymers for Lithographic Applications*, *Polym. Eng. Sci.* **23**, 1054 (1983).
- [46] Membrane window thickness of 100 nm Si_3N_4 with surrounding silicon support of 200 μm . Total dimensions diagonally of sample is 3.0 mm.
- [47] H. W. Fuller, and M. E. Hale, Determination of Magnetization Distribution in Thin Films Using Electron Microscopy, *J. Appl. Phys.* **31**, 238 (1960).
- [48] J. N. Chapman, Investigation of Magnetic Domain Structures in Thin Foils by Electron Microscopy, *J. Phys. D: Appl. Phys.* **17**, 623 (1984).
- [49] D. B. Williams, and C. B. Carter, *Transmission Electron Microscopy* (Springer, New York, 1996), pp. 457.
- [50] G. Zaránd, F. Pázmándi, K. F. Pál, and G. T. Zimányi, Using Hysteresis for Optimization, *Phys. Rev. Lett.* **89**, 150201 (2002).
- [51] B. Goncalves, and S. Boettcher, Hysteretic optimization for spin glasses, *Journal of statistical mechanics: theory and experiment* **1**, P01003 (2008).
- [52] A. Imre, G. Csaba, G. H. Bernstein, W. Porod, and V. Metlushko, Investigation of shape-dependent switching of coupled nanomagnets, *Superlattices and Microstructures* **34**, 513 (2003).
- [53] A possible cause of this asymmetric distribution might be the astigmatism in the electron-beam lithography, which results in about 3.3% width difference between the lines of the three sub-lattices of spins.
- [54] Y. Tabata, H. Kadowaki, K. Matsuhira, Z. Hiroi, N. Aso, E. Ressouche, and B. Fk, Kagome Ice State in the Dipolar Spin Ice $\text{Dy}_2\text{Ti}_2\text{O}_7$, *Phys. Rev. Lett.* **97**, 257205 (2006).
- [55] R. G. Melko, B. C. den Hertog, and M. J. P. Gingras, Long-Range Order at Low Temperatures in Dipolar Spin Ice, *Phys. Rev. Lett.* **87**, 067203 (2001).
- [56] R. G. Melko, and M. J. P. Gingras, Monte Carlo Studies of the Dipolar Spin Ice Model, *J. Phys.: Condens. Matter* **16** (2004).

- [57] Z. Hiroi, K. Matsuhira, S. Takagi, T. Tayama, and T. Sakakibara, Specific heat of kagome ice in the pyrochlore oxide $\text{Dy}_2\text{Ti}_2\text{O}_7$, *Journal of Physical Society of Japan* **72**, 411 (2003).
- [58] M. Udagawa, M. Ogata, and Z. Hiroi, Exact result of ground-state entropy for ising pyrochlore magnets under a magnetic field along [111] axis, *Journal of Physical Society of Japan* **71**, 2365 (2002).
- [59] K. Kano, and S. Naya, Antiferromagnetism: the kagome ising net, *Progress of theoretical physics* **10** (1953).
- [60] C. Castelnovo, R. Moessner, and S. L. Sondhi, Magnetic monopoles in spin ice, *Nature* **451**, 42 (2008).
- [61] P. Mellado, O. Tchernyshyov, Y. Qi, T. Brintlinger, and J. Cumings, in APS March Meeting New Orleans, 2008).
- [62] L. Pauling, *The nature of the chemical bond* (Cornell University Press, Cornell, 1960).
- [63] C. E. Shannon, A Mathematical Theory of Communication, *Bell System Technical Journal* **27**, 379 (1948).
- [64] E. T. Jaynes, Information Theory and Statistical Mechanics, *Phys. Rev.* **106**, 620 (1957).
- [65] R. N. Mantegna, S. V. Buldyrev, A. L. Goldberger, S. Havlin, C. K. Peng, M. Simons, and H. E. Stanley, Linguistic Features of Noncoding DNA Sequences, *Phys. Rev. Lett.* **73**, 3169 (1994).
- [66] I. Mirebeau, I. N. Goncharenko, P. Cadavez-Peres, S. T. Bramwell, M. J. P. Gingras, and J. S. Gardner, Pressure-induced crystallization of a spin liquid, *Nature* **420**, 54 (2002).
- [67] I. Mirebeau, I. N. Goncharenko, G. Dhalenne, and A. Revcolevschi, Pressure and Field Induced Magnetic Order in the Spin Liquid $\text{Tb}_2\text{Ti}_2\text{O}_7$ as Studied by Single Crystal Neutron Diffraction, *Phys. Rev. Lett.* **93**, 187204 (2004).
- [68] M. Mito, S. Kuwabara, K. Matsuhira, H. Deguchi, S. Takagi, and Z. Hiroi, Uniaxial pressure effects on spin-ice compound $\text{Dy}_2\text{Ti}_2\text{O}_7$, *J. Magnetism and Magnetic Materials* **310**, e432 (2007).
- [69] G. C. Lau, R. S. Freitas, B. G. Ueland, B. D. Muegge, E. L. Duncan, P. Schiffer, and R. J. Cava, Zero-point entropy in stuffed spin-ice, *Nat. Phys.* **2**, 249 (2006).
- [70] S. T. Bramwell, M. J. P. Gingras, P. C. Holdsworth, *Frustrated Spin Systems* (World Scientific, London, 2004), p. 367.
- [71] V. F. Petrenko, and R. W. Whitworth, *Physics of Ice* (Oxford University Press, Oxford, 1999), p. 384.
- [72] K. Matsuhira, Y. Hinatsu, K. Tenya, and T. Sakakibara, Low temperature magnetic properties of frustrated pyrochlore ferromagnets $\text{Ho}_2\text{Sn}_2\text{O}_7$ and $\text{Ho}_2\text{Ti}_2\text{O}_7$, *J. Phys.: Condensed Matter* **12**, L649 (2000).
- [73] S. Kawada, Dielectric Anisotropy in Ice Ih, *J Phys Soc Jpn* **44**, 1881 (1978).
- [74] J. W. Glen, Effect of Hydrogen Disorder on Dislocation Movement and Plastic Deformation of Ice, *Phys Kondens Mater* **7**, 43 (1968).
- [75] Y. Tajima, T. Matsuo, and H. Suga, Phase-Transition in Koh-Doped Hexagonal Ice, *Nature* **299**, 810 (1982).
- [76] A. Libál, C. Reichhardt, and C. J. O. Reichhardt, Realizing colloidal artificial ice on arrays of optical traps, *Phys. Rev. Lett.* **97**, 228302 (2006).

- [77] C. Nisoli, R. Wang, J. Li, W. F. McConville, P. E. Lammert, P. Schiffer, and V. H. Crespi, Ground State Lost but Degeneracy Found: The Effective Thermodynamics of Artificial Spin Ice, *Phys. Rev. Lett.* **98**, 217203 (2007).
- [78] Y. Aharonov, and D. Bohm, Significance of Electromagnetic Potentials in the Quantum Theory, *Phys. Rev.* **115**, 485 (1959).
- [79] Quantitative study of magnetic field distribution by electron holography and micromagnetic simulations
- [80] D. B. Williams, and C. B. Carter, *Transmission Electron Microscopy* (Springer Science, New York, 1996), p. 460.
- [81] T. Brintlinger, Carbon Nanotube Device: Growth, Imaging, and Electronic Properties, (Ph.D dissertation, University of Maryland, College Park, 2005), p. 98.
- [82] H. Schmid, Multi-ferroic magnetoelectrics, *Ferroelectrics* **162**, 665 (1994).
- [83] H. Schmid, Introduction to the proceedings of the 2nd international conference on magnetoelectric interaction phenomena in crystals, *Ferroelectrics* **161**, 1 (1994).
- [84] J. P. Rivera, definition, units, measurements, tensor forms of the linear magnetoelectric effect and on a new dynamic method applied to Cr-Cl boracite, *Ferroelectrics* **161**, 165 (1994).
- [85] I. E. Dzyaloshinskii, Magneto-electrical effects in antiferromagnets, *Sov. Phys. JETP* **10**, 628 (1959).
- [86] M. Bichurin, Short introduction to the proceedings of the 3rd international conference on magnetoelectric interaction phenomena in crystals, *Ferroelectrics* **204**, XVII (1997).
- [87] G. A. Smolenskii, and I. E. Chupis, Ferroelectromagnets, *Sov. Phys. USPEKHI* **25**, 475 (1982).
- [88] B. I. Al'shin, and D. N. Astrov, Magnetoelectric effect in Titanium Oxide Ti_2O_3 , *Soviet Physics JETP* **17**, 809 (1963).
- [89] A. M. J. G. Van Run, Terrell, D.R. and Scholing, An in situ Grown Eutectic Magnetoelectric Composite Material: Part 2. Physical Properties, *J. Mater. Sci.* **9**, 1710 (1974).
- [90] C.-W. Nan, Magnetoelectric effect in composites of piezoelectric and piezomagnetic phases, *Phys. Rev. B* **50**, 6082 (1994).
- [91] C. Ning, N. Ce-Wen, Z. Junyi, and L. Yuanhua, Large high-frequency magnetoelectric response in laminated composites of piezoelectric ceramics, rare-earth iron alloys and polymer, *Appl. Phys. Lett.* **84**, 3516 (2004).
- [92] G. Srinivasan, E. T. Rasmussen, B. J. Levin, and R. Hayes, Magnetoelectric effects in bilayers and multilayers of magnetostrictive and piezoelectric perovskite oxides, *Physical Review B* **65**, 134402 (2002).
- [93] M. K. Lee, T. K. Nath, C. B. Eom, M. C. Smoak, and F. Tsui, Strain modification of epitaxial perovskite oxide thin films using structural transitions of ferroelectric $BaTiO_3$ substrate, *Appl. Phys. Lett.* **77**, 3547 (2000).
- [94] Yi Qi, S. Anlage, H. Zheng, R. Ramesh, Local dielectric measurements of $BaTiO_3$ - $CoFe_2O_4$ nanocomposites through microwave microscopy *J. Mat. Res.* **22**, 1193 (2007).
- [95] D. E. Steinhauer, C. P. Vlahacos, F. C. Wellstood, M. A. Steven, C. Canedy, R. Ramesh, A. Stanishevsky, and J. Melngailis, Imaging of microwave permittivity,

- tunability, and damage recovery in (Ba, Sr)TiO₃ thin films, *Appl. Phys. Lett.* **75**, 3180 (1999).
- [96] H. M. Altshuler, *Handbook of Microwave Measurements II* (Polytechnic Inst. Of Brooklyn, Brooklyn, NY 1962).
- [97] Quantitative imaging of sheet resistance, permittivity, and ferroelectric critical phenomena with a near-field scanning microwave microscope
- [98] Ansoft Maxwell 2D: Electromagnetic Field Simulation for High-Performance Electromechanical Design
- [99] A. Imtiaz, M. Pollak, S. M. Anlage, J. D. Barry, and J. Melngailis, Near-field microwave microscopy on nanometer length scales, *Appl. Phys. Lett.* **97**, 044302 (2005).
- [100] S. M. Anlage, V. V. Talanov, and A. R. Schwartz, in *Principles of Near-Field Microwave Microscopy*, edited by S. Kalinin and A. Gruverman (Springer, New York, 2006), p. 207.
- [101] K. S. Chang, M. A. Aronova, C. L. Lin, M. Murakami, M. H. Yu, J. Hattrick-Simpers, O. O. Famodu, S. Y. Lee, R. Ramesh, M. Wuttig, I. Takeuchi, C. Gao, and L. A. Bendersky, Exploration of artificial multiferroic thin-film heterostructures using composition spreads, *Appl. Phys. Lett.* **84**, 3091 (2004).
- [102] Y. F. Popov, Features of the magnetoelectric properties of BiFeO₃ in high magnetic fields, *J. Low-Temp. Phys.* **27**, 478 (2001).
- [103] T. Kimura, S. Kawamoto, I. Yamada, M. Azuma, M. Takano, and Y. Tokura, Magnetocapacitance effect in multiferroic BiMnO₃, *Phys. Rev. B* **67**, 180401 (2003).
- [104] E. Ascher, H. Rieder, H. Schmid, and H. Stossel, Some Properties of Ferromagnetoelectric Nickel-Iodine Boracite, Ni₃B₇O₁₃I, *J. Appl. Phys.* **37**, 1404 (1966).
- [105] N. Hur, S. Park, P. A. Sharma, J. S. Ahn, S. Guha, and S. W. Cheong, Electric polarization reversal and memory in a multiferroic material induced by magnetic fields, *Nature* **429**, 392 (2004).
- [106] J. Wang, J. B. Neaton, H. Zheng, V. Nagarajan, S. B. Ogale, B. Liu, D. Viehland, V. Vaithyanathan, D. G. Schlom, U. V. Waghmare, N. A. Spaldin, K. M. Rabe, M. Wuttig, and R. Ramesh, Epitaxial BiFeO₃ Multiferroic Thin Film Heterostructures, *Science* **299**, 1719 (2003).
- [107] S. Dong, J. Cheng, J. F. Li, and D. Viehland, Enhanced magnetoelectric effects in laminate composites of Terfenol-D/Pb(Zr,Ti)O₃ under resonant drive, *Appl. Phys. Lett.* **83**, 4812 (2003).
- [108] J. G. Wan, J. M. Liu, H. L. W. Chand, C. L. Choy, G. H. Wang, and C. W. Nan, Giant magnetoelectric effect of a hybrid of magnetostrictive and piezoelectric composites, *J. Appl. Phys.* **93**, 9916 (2003).
- [109] A. K. Yasuo Cho, and Takahiro Saeki, Scanning nonlinear dielectric microscope, *Rev. Sci. Instrum.* **67**, 2297 (1996).
- [110] M. E. Lines, and A. M. Glass, *Principles and Applications of Ferroelectrics and Related Materials* (Clarendon Press, Oxford, 1977).